Lehigh University
Lehigh Preserve

Theses and Dissertations

2015

Hydrogen centers and the conductivity of In2O3 single crystals studied by FTIR spectroscopy

Weikai Yin
Lehigh University

Follow this and additional works at: http://preserve.lehigh.edu/etd

Part of the Physics Commons

Recommended Citation
Yin, Weikai, "Hydrogen centers and the conductivity of In2O3 single crystals studied by FTIR spectroscopy" (2015). *Theses and Dissertations*. 2896.
http://preserve.lehigh.edu/etd/2896

This Dissertation is brought to you for free and open access by Lehigh Preserve. It has been accepted for inclusion in Theses and Dissertations by an authorized administrator of Lehigh Preserve. For more information, please contact preserve@lehigh.edu.

Hydrogen centers and the conductivity of In_2O_3 single crystals studied by FTIR Spectroscopy

by

Weikai Yin

A Dissertation

Presented to the Graduate and Research Committee

of Lehigh University

in Candidacy for the Degree of

Doctor of Philosophy

in

Physics

Lehigh University

August 2015

© Copyright by Weikai Yin 2015

All Rights Reserved

Certificate of Approval

Approved and recommended for acceptance as a dissertation in partial fulfillment of the requirements for the degree of Doctor of Philosophy.

Weikai Yin

"Hydrogen centers and the conductivity of In_2O_3 single crystals studied by FTIR Spectroscopy"

____
Defense Date

____
Michael Stavola
Dissertation Director

____
Approved Date

____
Beall Fowler
Committee Member

____
Ivan Biaggio
Committee Member

____
Jerome Licini
Committee Member

____
Richard Vinci
Outsider Member

Acknowledgement

Reviewing my five year difficult and meaningful journey towards my Ph.D., many people have helped me in my study, research and life, which motivated me and promoted my accomplishment of my Ph.D.. First and foremost, I would like to express my special appreciation and thanks to my advisor, Professor Michael Stavola, for his encouragement, patience and guidance during these past five years. He has been a tremendous advisor for me not only with his insightful thought, and abundant knowledge, but also his enthusiasm and motivation. His life is just full of positive attitude, which makes my tough lab experience enjoyable and well-organized. His advice on both research and future career have been invaluable. I would also like to thank Professor Beall Fowler for his contribution to theoretical calculations in my Ph.D. work. His logical way of thinking and explanation was impressive when the theoretical physics that explained my research was challenging. I will be thankful to Professor Ivan Biaggio for his contribution to the simulation of diffusion in my research with his brilliance. I am also very grateful to my Ph.D. committee members, Professor Richard Vinci and Professor Jerome Licini for providing me advice on improving my research and ways of expressing.

I will be forever thankful to all my lab mates for helping me and making Professor Stavola's lab so enjoyable. Especially Philip Weiser, who is enthusiastic, motivated and well-organized, was always willing to share ideas and cooperate in our research,

which will surely make me miss him after I graduate. I would also thank to Ying Qin, Figen Bekisli, Haoxiang Zhang and Kirby Smithe for your support in any task. I also give my appreciation to John Gregoris for his assistance in the workshop and Lois Groff and Pamela Gescek for their help in the office. Furthermore, I would like to thank the entire faculty and my fellow classmates for their help in courses, research and life.

I would like to express my special thanks to my parents. Words cannot express my gratitude for their love, understanding, support and all of the sacrifices that they have made to my Ph.D. work and entire life.

Finally, I express my endless thanks to my girlfriend, Yangyang Xiao, who not only encouraged me, supported me, gave me unconditional love but also were strict with me. The life with her has made me always feel "unsatisfied" and motivated after new accomplishments. Thanks for her love and always letting me know "I deserve to be better", which has encouraged me work harder and fight for my dream.

Table of Contents

Title Page....i

Copyright....ii

Certificate of Approval....iii

Acknowledgement....iv

Table of Contents....vi

List of Figures....ix

List of Tables....xvi

Abstract....1

Chapter 1: Transparent Conducting Oxides....3

1.1: Introduction to Transparent Conducting Oxides....3

1.2: Crystal Structures of Transparent Conducting Oxides....6

1.3: H as a source of conductivity in oxides....10

1.3.1: Hydrogen in ZnO....10

1.3.2: Hydrogen in In_2O_3....15

References....21

Chapter 2: Experimental Methods....24

2.1: Local Vibrational Modes (LVMs)....24

2.2: infrared absorption and free carrier absorption....28

2.3: Experimental Techniques....32

2.3.1: Fourier-transform infrared spectroscopy (FTIR)....32

2.3.2: Instrumentation....37

2.3.3: Other Techniques - Raman spectroscopy & Hall effect............43

2.4: Diffusion..47

2.4.1: Indiffusion experiments..48

2.4.2: Outdiffusion experiments..49

References...52

Chapter 3: Hydrogen centers and the conductivity of In_2O_3 single crystals.......53

3.1: Introduction..53

3.2: Experimental Procedures...54

3.3: Experimental Results..55

3.3.1: Free-carrier absorption and O-H vibrational lines......................56

3.3.2: Annealing and thinning experiments...59

3.3.3: Calibration of IR lines..67

3.3.4: Hydrogen diffusion in In_2O_3 crystals..69

3.3.5: H_O shallow donors?..76

3.3.6: Other IR absorption lines..77

3.3.7: In_2O_3 phonons..80

3.3.8: Other shallow donors and deep compensating centers............83

3.4: Defect Modeling...85

3.5: Conclusions..90

References..92

Chapter 4: Conclusion..95

APPENDIX I..97

APPENDIX II..99

APPENDIX III...101

Vita...103

List of Figures

1.1: In_2O_3 as-grown crystals appear to be yellowish. They have high transmission in the visible region of the spectrum and high electrical conductivity................................4

1.2: ITO coated glass has a low absorption (high transmission) in the visible region. An absorption spectrum for ITO coated glass (Red) and absorption spectrum of uncoated glass (black)..5

1.3: ZnO crystal showing high light transmission [1.9]...5

1.4: Rutile crystal structure of SnO_2. Each Sn atom (grey) is surrounded by six oxygen neighbors. Each oxygen atom (red) is surrounded by three coplanar Sn atoms..........7

1.5: Zinc Oxide crystal structures. (a) hexagonal wurtzite; (b) cubic zincblende [1.19]..8

1.6: In_2O_3 Bixbyite crystal structure with 80 atoms in a conventional cell. In atom (grey); O atom (red) [1.23]...9

1.7: Local structures of In atoms (In1 and In2) surrounded by six O atoms. All O sites are equivalent and are surrounded by four In atoms. (a) The 8b In site (In1). (b) The 24d In site (In2). (c) The O site [1.22]...10

1.8: ZnO wurtzite structure and the sites on which interstitial hydrogen can be incorporated. BC indicates a bond-center site, and AB indicates an antibonding site [1.24]...11

1.9: Formation energies of interstitial hydrogen in ZnO, as a function of Fermi level, obtained from DFT-LDA calculations. The zero of Fermi energy is chosen at the top of the valence band. The theoretical (E_g^{th} = 1.91 eV, dotted line) and experimental (E_g^{exp}

= 3.4 eV) band gaps are indicated. The energies for H^0 and H^- are shown in dashed lines to indicate they are underestimated in the LDA calculations [1.24]....................12

1.10: Coupling between the H 1s orbital and the Zn 4s 'dangling bonds' (Zn dbs) to form the hydrogen multicenter bond in ZnO [1.27]..13

1.11: Formation energies as a function of the Fermi-level position for hydrogen in the multicenter bond configuration H_O, interstitial hydrogen H_i and the oxygen vacancy V_O in ZnO (a) and MgO (b) [1.27]...14

1.12: The possible sites for interstitial H in the In_2O_3 crystal structure. Red: bond center sites; green: anion anti-bonding sites [1.22]..15

1.13: Relaxed geometry of H defects in In_2O_3. (a) H_i^+ at AB_{O1} site; (b) H_i^- at the 16c site; (c) H at oxygen vacancy (H_O^+) [1.22]..16

1.14: The formation energies of hydrogen defects and oxygen vacancies in In_2O_3 as a function of Fermi energy [1.22]...17

1.15: Amplitude of the paramagnetic fraction Mu^0 and diamagnetic fraction Mu^+ of muonium in In_2O_3 as a function of temperature. The fits to an ionization model give an activation energy of 47$\pm$6 meV [1.28]...17

1.16: Interstitial hydrogen donors and their complexes with various cation vacancies in In_2O_3. (a) H_i^+, (b) $(V_{In}\text{-}H)^{-2}$ on the 24d site, and (c) $(V_{In}\text{-}H)^{-2}$ on the 8d site [1.16]..20

1.17: Predicted formation energies for vacancies and their complexes with hydrogen in In_2O_3, shown in the limit of (a) O-rich and (b) In-rich conditions [1.16]....................20

2.1: Density of vibrational states for undoped and ^{12}C-doped GaP (M_1=70, M_2=31) by

numerical calculation in a linear-chain model. A local vibrational mode due to ^{12}C appears at ω=510 cm^{-1} [2.1]..25

2.2: The harmonic-oscillator (dashed line) and Morse (solid line) potential energy functions for HCl...27

2.3: The harmonic-oscillator (dashed line) and Morse (solid line) potential energy functions. Energy levels of hydrogen and deuterium are indicated by horizontal lines [2.1]..27

2.4: The absorption cross section as a function of frequency ω and damping factor γ. γ is approximately the FWHM of the absorption peak [2.1].......................................29

2.5: A hydrogen doped ZnO crystal sample was annealed in flowing N_2 at elevated temperature from 50°C to 700°C. (a) the absorption coefficient at around 2000 cm^{-1} to 3000 cm^{-1}; (b) free carrier concentration as a function of annealing temperature [2.9]..31

2.6: Schematic diagram of a FTIR spectrometer...32

2.7: Interferograms and their corresponding Fourier transformed spectra for (a) a single frequency, (b) two close frequencies, (c) broad continuous frequencies. Especially at the zero optical path difference (ZPD) position in the interferogram (c), a large signal is observed because all wavelengths contribute constructively...............34

2.8: A hydrogen doped In_2O_3 sample; (a) interferogram, (b) sample raw spectrum, (c) reference spectrum, (d) absorbance spectrum..37

2.9: The optical configuration of Bomem DA 3.16 spectrometer................................38

2.10: Illustration of Oxford CF1204 cryostat...42

2.11: Configuration of a Raman system..43

2.12: Transitions for Rayleigh (elastic) and Raman (inelastic) scattering..................44

2.13: Schematic diagram of Raman shift (Stokes scattering). A Raman shift gives the local vibrational mode frequency..45

2.14: Hall Effect measurement geometry..46

3.1: A selection of IR absorption spectra (T = 4.2 K, resolution = 1 cm^{-1}) for an In_2O_3 sample that initially had been hydrogenated by an anneal (30 min) in an H_2 ambient at 500°C. The sample was then annealed sequentially in flowing He at the temperatures shown in °C. (a) The absorption due to free carriers. (b) The IR absorption lines in the O-H stretching region. These spectra were baseline corrected to remove the contribution from free carriers..56

3.2: IR absorption spectra (4.2 K, resolution = 1 cm^{-1}) for In_2O_3 samples containing D and H. Spectra were baseline corrected to remove the contribution from free carriers. The sample for the upper spectrum in (a) had been deuterated by annealing in a D_2 ambient (60 min) at 500°C. It was then annealed in flowing He at 550°C to increase its transparency and to produce the O-D lines that are shown. The sample for the upper spectrum in (b) had been hydrogenated by annealing (30 min) in an H_2 ambient at 500°C and subsequently annealed (30 min) at 550°C. [The lower spectrum in (a) shows the D-stretching region for a hydrogenated sample and the lower spectrum in (b) shows the H-stretching region for a deuterated sample.]....................................57

3.3: A selection of IR absorption spectra (T = 77 K, resolution = 1 cm^{-1}) for an In_2O_3 sample that initially had been annealed (60 min) in flowing He at 850°C to remove any

hydrogen that might have been present and was that subsequently deuterated by an anneal (30 min) in an D_2 ambient at 500°C. The sample was then annealed sequentially in a flowing He ambient at the temperatures shown in °C. (a) The absorption due to free carriers. (Free carrier absorption spectra measured following anneals from 50 to 250°C are indistinguishable from the results shown for the D-treated sample and also following the anneal at 200°C.) (b) The IR absorption lines in the O-D stretching region. These spectra were baseline corrected to remove the contribution from free carriers..60

3.4: A selection of IR absorption spectra (T = 77 K, resolution = 1 cm^{-1}) for a hydrogenated In_2O_3 sample that was annealed sequentially in flowing N_2 at 400°C for different accumulated times. (a) The absorption due to free carriers. (b) The IR absorption lines in the O-H stretching region..61

3.5: The decay of free carrier absorption and the peak height of the interstitial O-H line at 3306 cm^{-1} for isothermal anneal experiments (400°C) plotted on a Log10 scale. (a) best fit to free carrier absorption; (b) best fit to the peak height of the interstitial O-H line at 3306 cm^{-1}. Both datasets were fit by Excel Solver and then plotted by OriginLab..62

3.6: Best fit to both the free carrier absorption (a) and the peak height of the interstitial O-H line at 3306 cm^{-1} (b) for isothermal annealing experiments (400°C). The same decay rates (0.89 h^{-1} and 0.026 h^{-1}) are used for both datasets.................................63

3.7: Best fit to data for the free carrier absorption (a) and the peak height of the interstitial O-H line at 3306 cm^{-1} (b) for isothermal annealing experiments (400°C). Fits

made with the same decay rates (-0.89 h^{-1} and -0.026 h^{-1}) are shown on a linear scale..64

3.8: A selection of IR absorption spectra (T = 77 K, resolution = 1 cm^{-1}) for an In_2O_3 sample that initially had been annealed (30 min) in flowing He at 1000°C to remove any hydrogen that might have been present and was subsequently hydrogenated by an anneal (30 min) in an H_2 ambient at 450°C. The sample was then sequentially thinned by lapping and polishing the front and back surfaces. The thickness removed following each thinning step (both sides) is shown in mm. (a) shows free-carrier absorption spectra for the H-treated sample and for the sample following thinning. (b) shows baseline-corrected IR spectra of the O-H absorption lines.............................65

3.9: Strength of free-carrier absorption and O-H vibrational absorption for the In_2O_3 sample whose IR data are shown in Fig. 3.8 as a function of thickness removed from the sample. The left scale (filled circles) shows the difference in the free-carrier absorption at 2500 and 4000 cm^{-1} for each thickness removed. The right scale (open circles) shows the integrated absorbance for the 3306 cm^{-1} O-H stretching line assigned to the interstitial H^+ shallow donor for each thickness removed..................66

3.10: The hydrogen defect concentration for an In_2O_3 sample (annealed in H_2 at 450°C for 1 hour) as a function of diffusion depth (layer thickness removed from one side). The experimental data were fit with a complementary error function................72

3.11: The out-diffusion coefficient D determined by integrating the numerical solution to generate the time dependence of hydrogen (normalized) and free carrier out-diffusion. The O-H (blue) and free carrier (black) out-diffusion experimental data

points were fit by Mathematica simulation curves (green and red) separately. A representative error bar is shown in the O-H experimental data that is due to uncertainty in the choice of baseline in the spectra. The orange curve is the best numerical integration fit to both two experimental datasets......................................76

3.12: IR absorption spectrum (T = 4.2 K, resolution = 1 cm^{-1}) for an In_2O_3 sample deuterated by an anneal (60 min) in a D_2 ambient at 500°C......................................78

3.13: IR absorption spectra in the O-D stretching region for four deuterated In_2O_3 samples, which then have been annealed in flowing N_2 to partially recover IR transparency. The O-D lines at 2469 (the shoulder) and 2521 cm^{-1} were introduced together into sample spectra..79

3.14: A strong IR absorption line at 1890 cm^{-1} (a) existed in an as-grown In_2O_3 sample but disappeared after a sample had been deliberately hydrogenated or deuterated. This line emerged again as the sample turned more transparent upon annealing (b)..81

3.15: Raman spectra of an as-grown In_2O_3 sample. (a) shows the fundamental region. (b) and (c) show spectra for the overtone regions. Line frequencies and suggested assignments are presented in Table 3.3...81

3.16: IR spectra of colored as-grown samples (gray and green samples). The gray sample was 0.825 mm thick and the green sample 1.160 mm thick. Samples were annealed at the temperature shown. (a) free carrier absorbance of gray and green In_2O_3 samples. (b) IR absorption lines in the O-H stretching region for the grey sample. (c) IR absorption lines in the O-H stretching region for the green sample...................84

3.17: Defect models. (a) The lowest energy antibonding configuration (AB_{01}) for H_i^+. (b) Metastable H_i^+ antibonding configurations (AB_{02} to AB_{04}). Defect labeling follows Ref. 12. (c) Lowest energy configuration for $[V_{In}(24d)\text{-}H]^{2-}$. Larger (blue) atoms represent O, smaller (black) atoms represent In, and the smallest (red) atom is H. This was constructed by MOLDRAW (P. Ugliengo, Torino 2006, available at http://www.moldraw.unito.it) and POV-Ray (http://povray.org)....................................86

List of Tables

3.1: Vibrational frequencies of O-H (O-D) modes seen for hydrogenated (deuterated) In_2O_3 single crystals. A possible shoulder giving rise to the asymmetry of the 3306 cm^{-1} line is unresolved....58

3.2: The intensities of O-D lines at 2464, 2469 (the shoulder) and 2521 cm^{-1} for four different deuterated In_2O_3 samples. The intensities of the 2521 cm^{-1} and 2469 cm^{-1} D lines are approximately equal....80

3.3: Frequencies of lattice vibrational lines seen with Raman measurements. Assignments of combination modes are suggested....82

3.4: Calculated vibrational frequencies and formation energies relative to the most stable configurations for H centers in In_2O_3. Defect labeling follows that of Refs. 12 and 27. Frequencies for H_i and V_{In}-H centers include the effect of anharmonicity. The results shown for H_O and D_O are harmonic frequencies....88

Abstract

The role played by hydrogen impurities in the conductivity of indium oxide (In_2O_3) has been controversial. Some studies, based on the effect of oxygen partial pressure in growth or annealing environments, argue that oxygen vacancies are the cause of the conductivity of In_2O_3. However, there is a growing body of theoretical and experimental work which suggests that hydrogen centers can be important shallow donors in In_2O_3. Muon-spin-resonance experiments indicate that implanted muons, whose properties mimic those of hydrogen, form shallow donors in In_2O_3. In_2O_3 thin films containing hydrogen show n-type conductivity with high mobility, and theory states that interstitial hydrogen (H_i^+) and hydrogen trapped at an oxygen vacancy (H_O^+) are shallow donors that can give rise to n-type conductivity or compensate acceptors in In_2O_3.

We have performed a series of IR absorption experiments and complementary theory to determine the properties of OH and OD centers in In_2O_3 single crystals. Annealing In_2O_3 samples in H_2 or D_2 at temperatures near 450°C produces an n-type layer ≈ 0.06 mm thick with an n-type doping of 1.6×10^{19} cm^{-3}. The resulting free-carrier absorption is correlated with an OH center with a vibrational frequency of 3306 cm^{-1} that we associate with interstitial H^+, which is thermally stable around 600°C. Additional O-H (O-D) vibrational lines are assigned to metastable configurations of the interstitial H^+ (D^+) center and complexes of H (D) with In

vacancies. Unlike other oxides studied recently where H trapped at an oxygen vacancy is the dominant shallow donor (ZnO and SnO_2, for example), interstitial H^+ is found to be the dominant H-related shallow donor in In_2O_3. In addition, the diffusion of hydrogen defects has been studied by thinning experiments and isothermal anneals.

Chapter 1:

Transparent Conducting Oxides

1.1: Introduction to Transparent Conducting Oxides

Transparent conducting oxides (TCOs) have unusual but highly useful properties, combining transparency in the visible region of the spectrum with high electrical conductivity. Glass fibers have high transmission of light but are electrical insulators, while silicon and compound semiconductors are electrical conductors but with dopant dependence. Transparent conducting oxides form a highly flexible intermediate class of materials with both these characteristics. They are usually prepared with thin film technologies and are used in opto-electrical devices such as solar cells, displays, opto-electrical interfaces, and transparent circuits [1.1]. Typically, these applications use electrode materials that have greater than 80% transmittance of incident light as well as conductivities higher than 10^3 S/cm for efficient carrier transport. TCOs for use as thin-film electrodes in solar cells should have a minimum carrier concentration on the order of 10^{20} cm^{-3} for low resistivity and a band-gap energy above approximately 3.0 eV to avoid absorption of light over most of the solar spectrum [1.2].

Indium tin oxide (ITO, 90% In_2O_3, 10% SnO_2 by weight) is the most widely used transparent conducting oxide because of its electrical conductivity (10^3 S/cm) and optical transparency (85%-90%). It is transparent and colorless in thin film form while yellowish to grey in bulk. Figure 1.1 shows In_2O_3 crystals, which appear to be yellowish. ITO is often used to make transparent conductive coatings for displays

such as flat panel displays and plasma displays. The absorption spectrum of ITO coated glass is similar to that of regular glass (Fig. 1.2). One common application involves ITO films deposited on aircraft windshields that are used for defrosting [1.3]. Heat is generated by applying voltage across the film. ITO thin films can be deposited with ion assisted plasma evaporation [1.4], electron beam evaporation [1.5-1.7], direct current (DC), pulsed DC (PDC) or thermal evaporation [1.8].

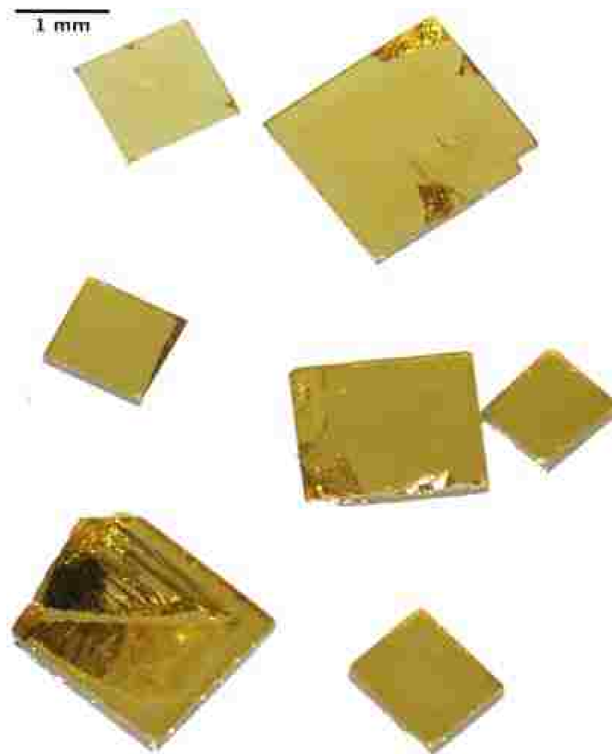

FIG. 1.1. In_2O_3 as-grown crystals appear to be yellowish. They have high transmission in the visible region of the spectrum and high electrical conductivity.

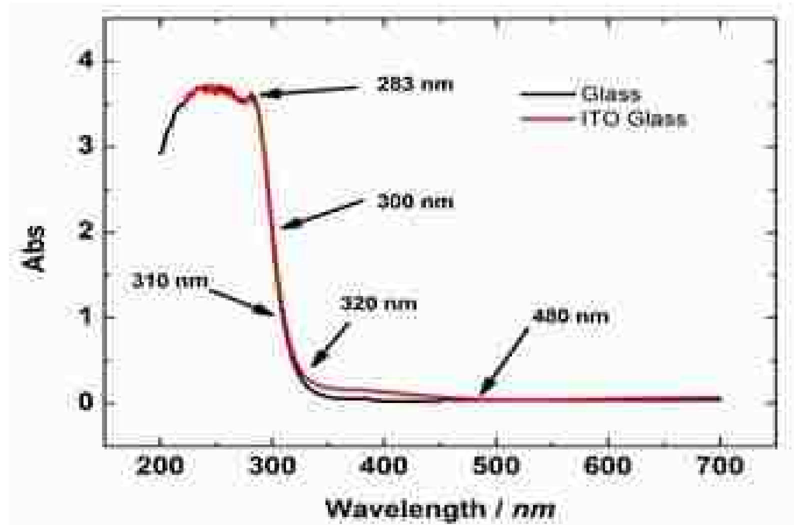

FIG. 1.2. ITO coated glass has a low absorption (high transmission) in the visible region. An absorption spectrum for ITO coated glass (Red) and absorption spectrum of uncoated glass (black).

FIG. 1.3. ZnO crystal showing high light transmission [1.9].

ZnO is another popular TCO in industry (Fig. 1.3) [1.9]. ITO is the most popular TCO in the current market because it is superior to ZnO in terms of transmittance and conductivity. However, since ITO is priced several times higher than ZnO, ZnO is a lower cost alternative to ITO in applications such as display technology and solar cells. Between 50% and 60% of ZnO is also used in the rubber industry [1.10]. The ceramic industry also consumes a significant amount of ZnO in ceramic glazes and frit compositions.

SnO_2 is another typical example of a TCO. Similar to ZnO, SnO_2 is a lower cost substitute to ITO with comparable performance in transparency and conductivity after proper treatments. SnO_2 has long been used as a glass coating and an opacifier or white colorant in ceramic glazes [1.11]. SnO_2 wires are also commonly used as the detecting element in carbon monoxide detectors [1.12]. The unique properties of transparent conducting oxides will lead to their wider use in the optoelectronics and energy industries.

1.2: Crystal Structures of Transparent Conducting Oxides

To investigate the properties and applications of TCOs, their crystal structures must be known. Various types of crystal structures result in different metal oxides properties and host-impurity bonds.

SnO_2 has the rutile crystal structure with a direct band gap of 3.6 eV. The unit cell of SnO_2 is shown in Fig. 1.4. Each Sn atom is surrounded by six oxygen neighbors, which form a distorted octahedron. Each oxygen atom is surrounded by three coplanar Sn atoms to form an almost equilateral triangle.

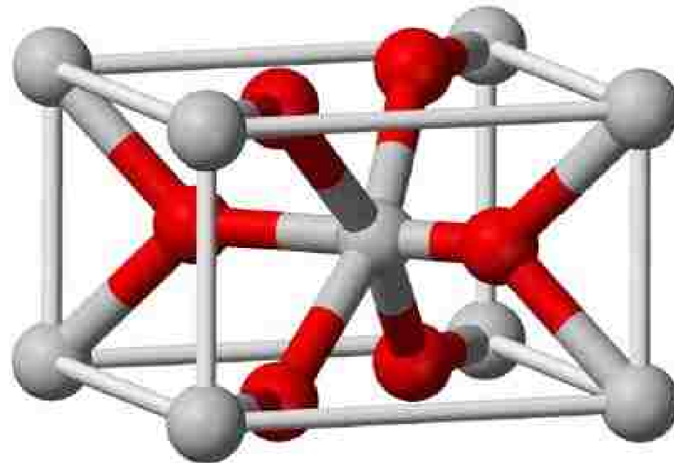

FIG. 1.4. Rutile crystal structure of SnO_2. Each Sn atom (grey) is surrounded by six oxygen neighbors. Each oxygen atom (red) is surrounded by three coplanar Sn atoms.

The conventional wisdom has been that the conductivity of TCOs is due to oxygen vacancies or cation interstitials [1.13-1.15]. As with other TCOs, the assumption that native defects are responsible for the n-type conductivity of SnO_2 has been challenged recently [1.16][1.17]. For example, Interstitial hydrogen (H_i) and hydrogen at an oxygen vacancy (H_O) have been predicted to be shallow donors in SnO_2. Interstitial hydrogen is not thermally stable in SnO_2 near room temperature, while H_O is a more thermally stable defect than H_i and decays upon annealing near

500^oC [1.18].

Titanium dioxide (TiO_2) also has the rutile crystal structure and an indirect band gap of 3.0 eV. TiO_2 is being investigated for photo-catalytic applications. H in TiO_2, unlike in ZnO or SnO_2, gives rise to electrons that are self trapped as small polarons.

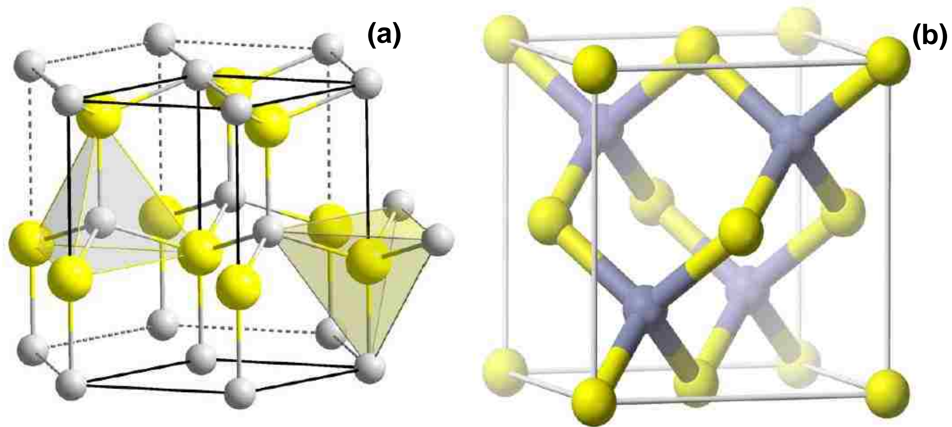

FIG. 1.5. Zinc Oxide crystal structures. (a) hexagonal wurtzite; (b) cubic zincblende [1.19].

ZnO has two possible crystal lattice structures, hexagonal wurtzite and cubic zincblende (Fig. 1.5) [1.19]. The wurtzite structure is most stable at ambient conditions. The zincblende form can be stabilized by growing ZnO on substrates with cubic lattice structure. In the wurtzite structure, each Zn atom is bonded to four oxygen atoms and each oxygen atom is bonded to four Zn atoms. ZnO has a band gap of 3.4 eV at room temperature. Historically, it was reported that as-grown ZnO is n-type because of native defects. However, recent experiments and theory have shown that oxygen vacancies are deep donors and H impurities are the most likely

cause of n-type conductivity in ZnO [1.17]. These new results for H confirm results in the old literature for ZnO that were mostly forgotten [1.20]. Interstitial H has been observed by IR spectroscopy, while H at an oxygen vacancy has been seen by photo-thermal ionization spectroscopy [1.21].

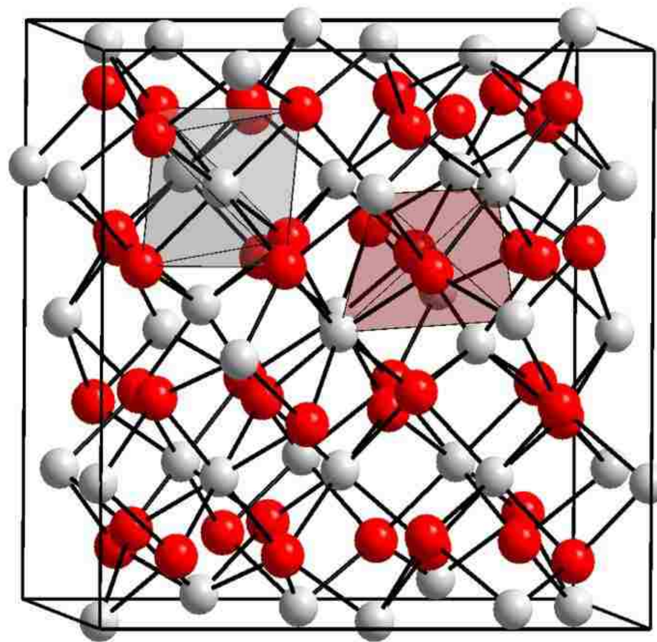

FIG. 1.6. In_2O_3 Bixbyite crystal structure with 80 atoms in a conventional cell. In atom (grey); O atom (red) [1.23].

In_2O_3 has a complicated cubic crystal structure called bixbyite with 80 atoms in a conventional cell [1.22]. The crystal structure is shown in Fig. 1.6 [1.23]. There are two inequivalent In sites, each of which is surrounded by six O atoms. A quarter of the In atoms occupy the 8b positions (In1) while the remaining three quarters occupy the 24d positions (In2) in Wyckoff notation [1.22]. Fig. 1.7 shows the calculated local

structures of O atoms (red) and the In1 and In2 atoms (grey). All O sites are equivalent and are surrounded by four In atoms. The local structure of an In1 atom is quite symmetrical, in which all six In-O bonds are equivalent with a bond distance of 0.2% smaller than the average value of all In-O bonds. The In2 local structure is less symmetrical and the six In-O bonds can be divided into three groups of two equivalent In-O bonds [1.22].

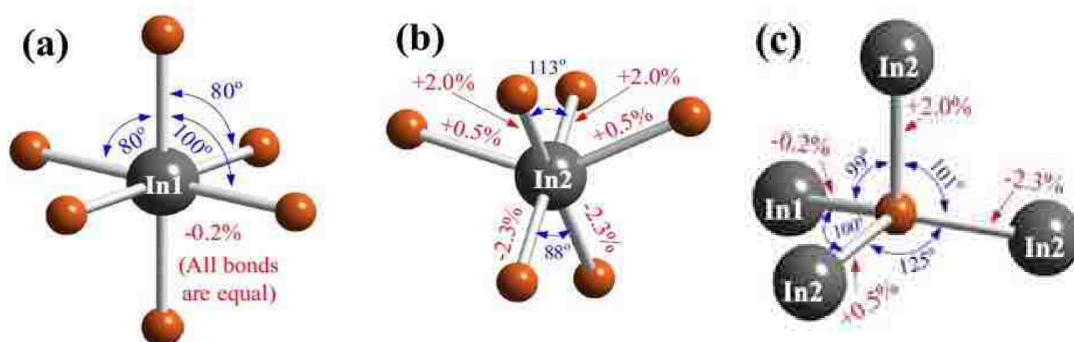

FIG. 1.7. Local structures of In atoms (In1 and In2) surrounded by six O atoms. All O sites are equivalent and are surrounded by four In atoms. (a) The 8b In site (In1). (b) The 24d In site (In2). (c) The O site [1.22].

1.3: H as a source of conductivity in oxides

1.3.1: Hydrogen in ZnO

The high electrical conductivity of TCOs has been attributed to native defects such as oxygen vacancies and cation interstitials based on early experimental work [1.13][1.15]. However, recent calculations and experiments have shown that native defects are not the major sources of n-type conductivity. It has been confirmed that

the hydrogen impurity increases the conductivity of TCOs and also gives rise to several hydrogen-containing centers. Hydrogen acts as a shallow donor and contributes to the n-type conductivity of TCOs [1.18].

Zinc oxide is a wide-band-gap semiconductor that exhibits n-type conductivity with many technological applications. It provides a good example of an oxide that can be doped n-type with hydrogen. A first-principles investigation, based on density functional theory, predicted that hydrogen behaves as a shallow donor and acts as a source of conductivity [1.24]. Fig. 1.8 shows the sites on which interstitial hydrogen can be incorporated in the ZnO wurtzite structure.

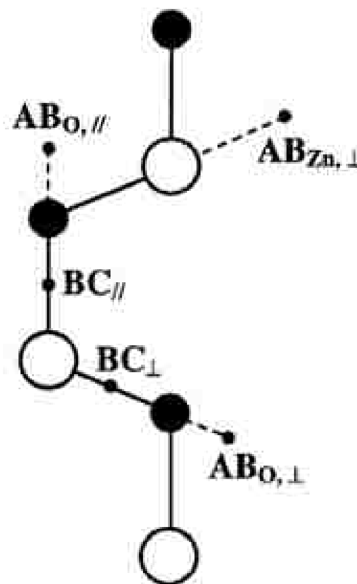

FIG. 1.8. ZnO wurtzite structure and the sites on which interstitial hydrogen can be incorporated. BC indicates a bond-center site, and AB indicates an antibonding site [1.24].

The DFT calculations predicted that for all charge states, the $BC_{\parallel}$ configuration (bond centered in a bond that is parallel to the c axis) is most stable with minimum formation energy [1.25]. This theoretical result also agrees with an experimental study of ZnO by infrared absorption spectroscopy [1.26]. The corresponding formation energies of all charge states are shown in Fig. 1.9 [1.24]. After correction of the calculated band gap, H^+ is the lowest-energy state throughout the experimental band gap. The formation energy of H^+ is low enough to give rise to a high concentration of hydrogen in n-type ZnO. Thus, in ZnO, H^+ is the stable charge state for all Fermi-level positions, which acts as a shallow donor.

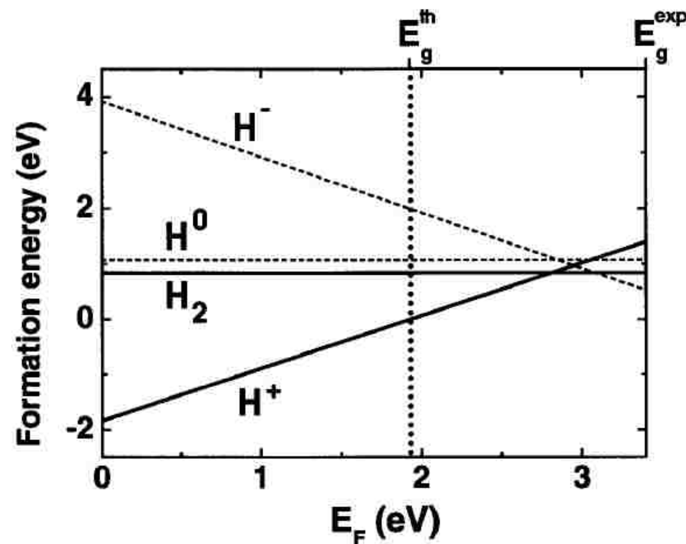

FIG. 1.9. Formation energies of interstitial hydrogen in ZnO, as a function of Fermi level, obtained from DFT-LDA calculations. The zero of Fermi energy is chosen at the top of the valence band. The theoretical (E_g^{th} = 1.91 eV, dotted line) and experimental (E_g^{exp} = 3.4 eV) band gaps are indicated. The energies for H^0 and H^- are shown in dashed lines to indicate they are underestimated in the LDA calculations [1.24].

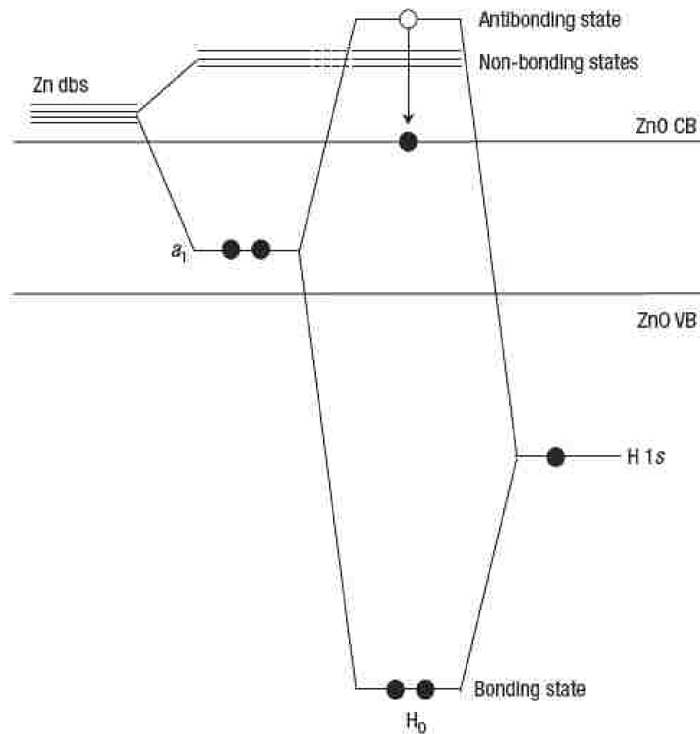

FIG. 1.10. Coupling between the H 1s orbital and the Zn 4s 'dangling bonds' (Zn dbs) to form the hydrogen multicenter bond in ZnO [1.27].

Recent research has provided evidence that hydrogen as a substitutional impurity (H_O) in ZnO, that is, as H trapped at an oxygen vacancy, also contributes to its conductivity [1.27]. Oxygen vacancies are low-energy defects and may form in large concentrations in ZnO, which are neutral and electrically inactive. Hydrogen on a substitutional oxygen site forms multicenter chemical bonds with all of its metal-atom nearest-neighbors (Fig. 1.10) [1.27]. In wurtzite structure ZnO, the removal of an oxygen atom from the lattice breaks four bonds. The H 1s orbital combines with the a_1 state and results in a fully symmetric bonding state in the valence band (VB), and an antibonding state in the conduction band (CB). The

electron that would occupy this antibonding state is then transferred to the conduction-band minimum, making the substitutional hydrogen H_O a shallow donor.

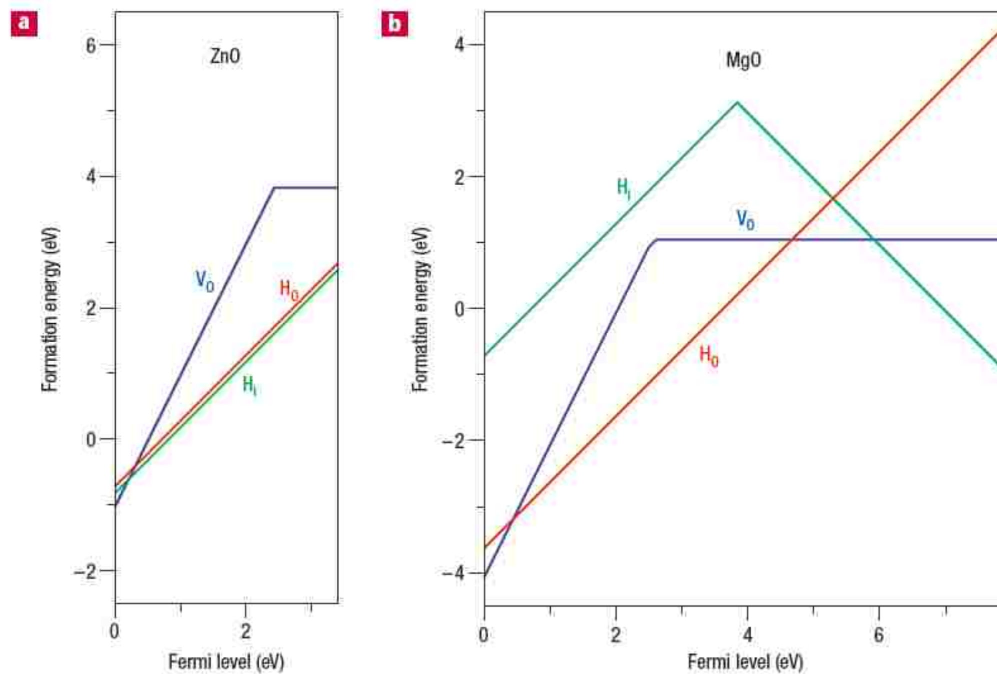

FIG. 1.11. Formation energies as a function of the Fermi-level position for hydrogen in the multicenter bond configuration H_O, interstitial hydrogen H_i and the oxygen vacancy V_O in ZnO (a) and MgO (b) [1.27].

Similarly, Fig. 1.11 shows the formation energy of H_O, based on DFT calculations, and indicates that substitutional hydrogen is most stable in ZnO and MgO [1.27]. H_O acts as a shallow donor in ZnO and only the +1 charge state is stable over the entire bandgap (Fig. 11a). In ZnO, interstitial hydrogen has a low formation energy resulting in a high concentration, which also gives rise to a shallow-donor level. However, H_i has a low diffusion barrier and is unstable at high temperatures, favoring H_O as the

dominant source in annealed samples. The oxygen vacancy is a deep donor. In MgO, the formation energy of H_O is lower than H_i (Fig. 11b), so H_O is expected to be the predominant form of hydrogen.

1.3.2: Hydrogen in In_2O_3

In In_2O_3, interstitial H (H_i) has positive, neutral and negative charge states. Similar to ZnO, H_i^+ exhibits local minima at the bond center (BC) and anion antibonding (AB_O) sites. In In_2O_3, there are four inequivalent BC and four inequivalent AB_O sites (Fig. 1.12) [1.22]. H_i^+ is found to not be stable at the BC sites. Calculated formation energies of all the H_i^+ configurations showed that $E_f(AB_{O1})$ = -2.09 eV has the lowest energy and makes AB_{O1} site the preferred site [1.22].

FIG. 1.12. The possible sites for interstitial H in the In_2O_3 crystal structure. Red: bond center sites; green: anion anti-bonding sites [1.22].

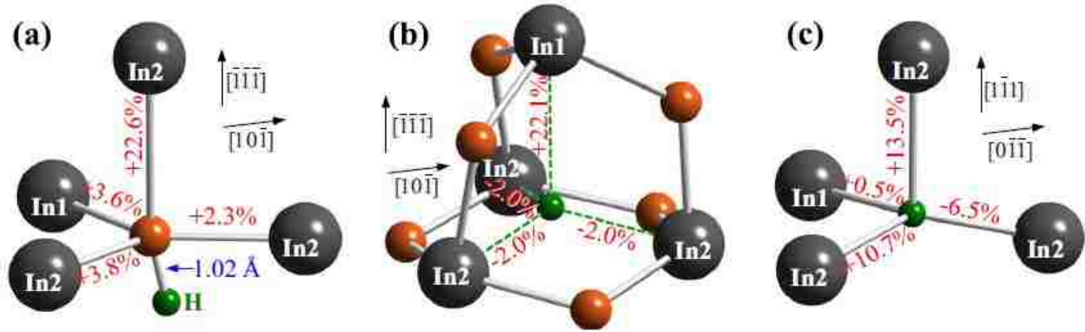

FIG. 1.13. Relaxed geometry of H defects in In_2O_3. (a) H_i^+ at AB_{O1} site; (b) H_i^- at the 16c site; (c) H at oxygen vacancy (H_O^+) [1.22].

The relaxed geometry of H_i^+ at the AB_{O1} site is shown in Fig. 1.13 (a). In the negative charge state, H_i prefers interstitial sites closer to the cations, referred to as 8a and 16c in Wyckoff notation. The formation energy of the 16c site H_i^- is lower by 0.9 eV than at the 8a site and the relaxed geometry of the 16c site H_i^- is shown in Fig. 1.13 (b). Fig. 1.14 shows the calculated formation energies of hydrogen defects as a function of Fermi energy, which predicts H_i^+ has the lowest formation energy. In addition to H_i^+, the formation energy of H_O^+ is higher than H_i^+, which suggests that H_i^+ will be the preferred configuration.

Recent research indicates that muonium forms a shallow-donor state in In_2O_3, and by analogy, so would hydrogen [1.28]. Fig. 1.15 shows the amplitude of the paramagnetic fraction and diamagnetic fraction of muonium in In_2O_3 as a function of temperature.

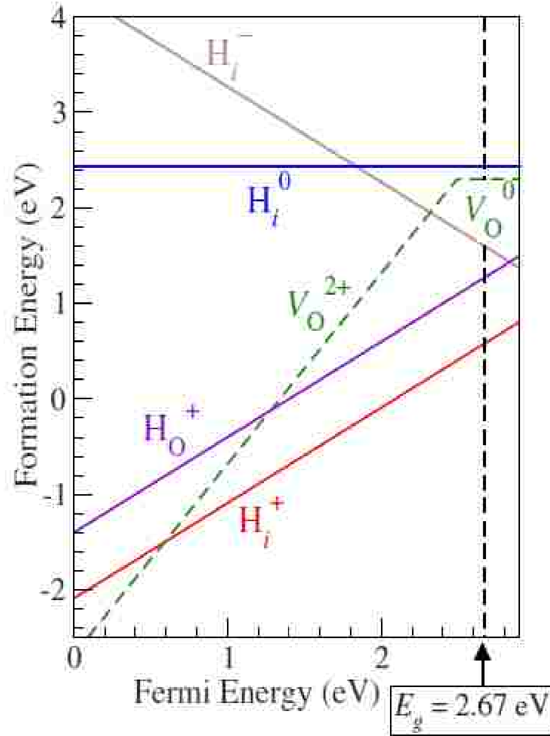

FIG. 1.14. The formation energies of hydrogen defects and oxygen vacancies in In_2O_3 as a function of Fermi energy [1.22].

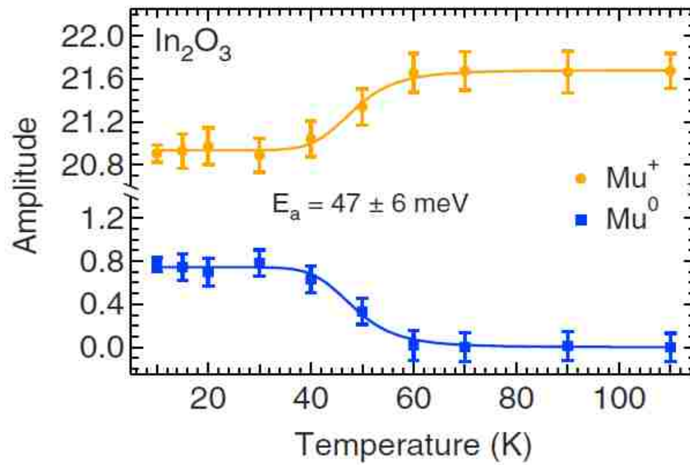

FIG. 1.15. Amplitude of the paramagnetic fraction Mu^0 and diamagnetic fraction Mu^+ of muonium in In_2O_3 as a function of temperature. The fits to an ionization model give an activation energy of 47 ± 6 meV [1.28].

All quantities derived are within a factor of two of values estimated from a simple hydrogenic model. By analogy, these results suggest that hydrogen will form a shallow-donor state which significantly contributes to the conductivity of In_2O_3.

Furthermore, H-doped In_2O_3 thin films have been deposited and high mobility and high near IR transparency have been achieved [1.29]. The deposition involved a sputtering process performed at room temperature and with a post-annealing treatment at 200°C. The H composition could be controlled by varying the water vapor pressure during the deposition. H-doped thin films showed large mobility, as high as 98-130 $cm^2/(V\text{-}s)$, and carrier concentration of $1.4\text{-}1.8\times10^{20}$ cm^{-3}. In addition, high transparency in the near IR was realized. Therefore, it was proposed that H-doped In_2O_3 has the potential to improve optoelectronic devices such as thin-film solar cells and photodetectors.

Studies of cation vacancies and their complexes with hydrogen impurities in In_2O_3 by first-principles calculations have also suggested a low formation energy for cation vacancies and their complexes with hydrogen [1.16]. Fig. 1.16 shows interstitial hydrogen donors and their complexes with various cation vacancies in In_2O_3. IR spectroscopy has indicated that cation vacancies strongly interact with H in TCOs resulting in complexes that are stable up to temperatures over 700°C [1.30]. Formation energies for vacancies and their complexes with hydrogen in In_2O_3 are shown in Fig. 1.17 [1.16]. It was realized that the isolated hydrogen interstitial acts as

a shallow donor with a low formation energy, which allows H_i^+ to be present with high concentration and mobility. While cation vacancies have high formation energies, their complexes with hydrogen were predicted to be much more favorable with lower formation energy. Thus, the vacancy–hydrogen complexes have low enough formation energies to potentially be incorporated during growth in a hydrogen-containing environment.

Oxygen vacancies traditionally have been suggested to be the cause of conductivity of In_2O_3 in some studies [1.31-1.33]. However, a growing body of theoretical and experimental work listed in this chapter finds that hydrogen centers, which have been ignored for decades, can be important shallow donors in TCOs like In_2O_3. Since the role played by hydrogen impurities in conductivity of In_2O_3 has been controversial, infrared (IR) spectroscopy, Hall effect measurements, and theory are used to investigate the microscopic properties of hydrogen centers in In_2O_3 single crystals and their relationship to conductivity in our research.

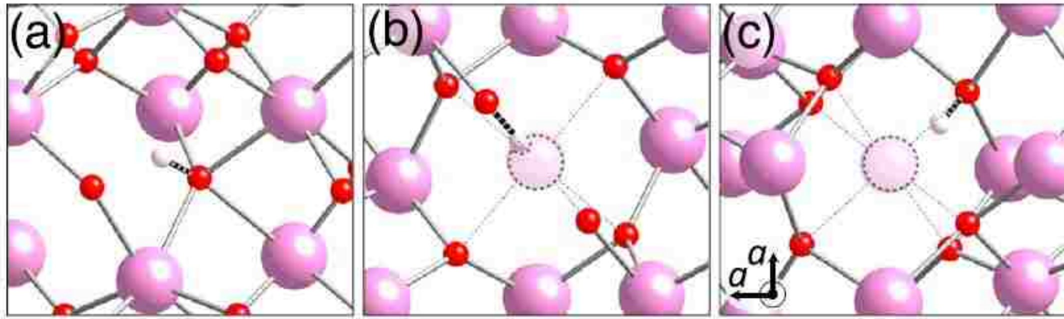

FIG. 1.16. Interstitial hydrogen donors and their complexes with various cation vacancies in In_2O_3. (a) H_i^+, (b) $(V_{In}\text{-}H)^{-2}$ on the 24d site, and (c) $(V_{In}\text{-}H)^{-2}$ on the 8d site [1.16].

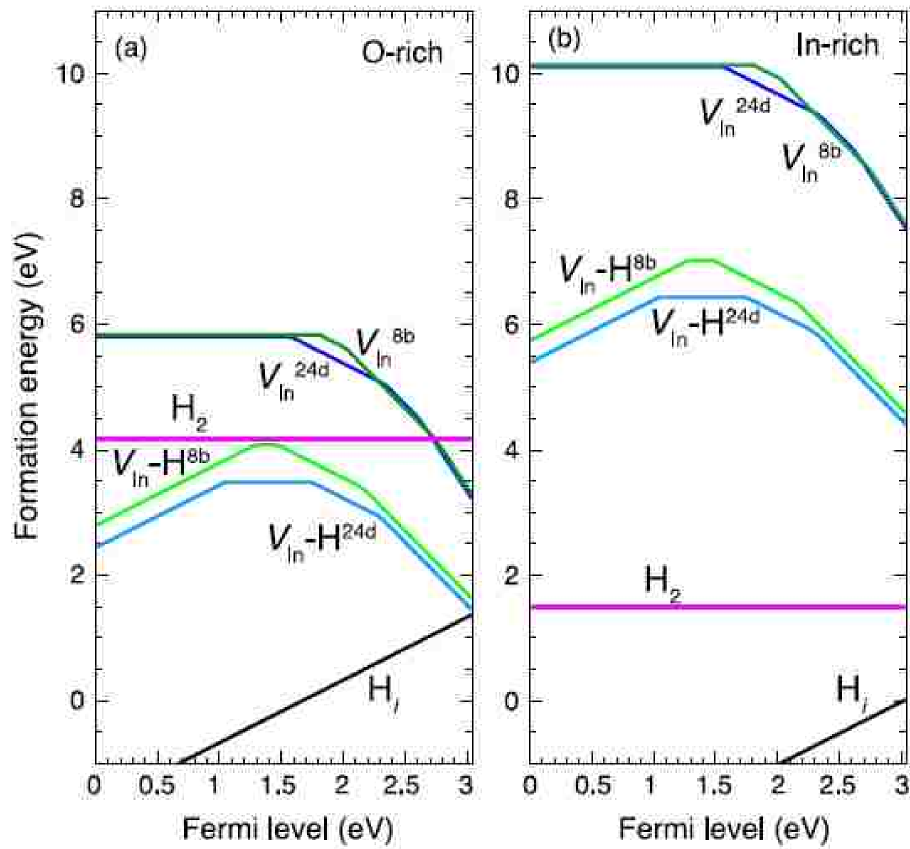

FIG. 1.17. Predicted formation energies for vacancies and their complexes with hydrogen in In_2O_3, shown in the limit of (a) O-rich and (b) In-rich conditions [1.16].

References

1.1. A. Stadler, Materials **5**, 661–683 (2012).

1.2. Minami, Tadatsugu, Semicond. Sci. Technol. **20** (4), S35 (2005).

1.3. M. A. McMaster, (Libby-Owens-Ford) (filed Oct. 5, 1942) U.S. Patent 2,429,420, issued 21 October 1947, (see other McMaster US and British patents too).

1.4. S. Laux, N. Kaiser, A. Zöller, R. Götzelmann, H. Lauth, Thin Solid Films **335**, 1–5 (1998).

1.5. D.C. Paine, T. Whitson, D. Janiac, R. Beresford, C.O. Yang, B. Lewis, J. Appl. Phys. **85**, 8445–8450 (1999).

1.6. C.H. Chen, S.J. Chang, Y.K. Su, G.C. Chi, J.Y. Chi, C.A. Chang, J.K. Sheu, J.F. Chen, IEEE Photonics Technol. Lett. **13**, 848–850 (2001).

1.7. J.K. Sheu, Y.K. Su, G.C. Chi, M.J. Jou, C.M. Chang, Appl. Phys. Lett. **72**, 3317–3319 (1998).

1.8. R.H. Horng, D.S. Wuu, Y.C. Lien, Appl. Phys. Lett. **79** (2925), 1–3 (2001).

1.9. K. Maeda, M. Sato, I. Niikura, Semicond. Sci. Technol. **20** (4), S49-S54 (2005)

1.10. A. Moezzi, A.M. McDonagh, M.B. Cortie, Chemical Engineering Journal 185–186, 1–22 (2012).

1.11. *The Glazer's Book – 2nd edition,* A.B.Searle (The Technical Press Limited, London, 1935).

1.12. *Sensors Nanoscience Biomedical Engineering and Instruments,* edited by R.C Dorf (CRC Press Taylor and Francis, FL, 2006).

1.13. *Semiconducting Transparent Thin Films,* H.L. Hartnagel, A.L. Dawar, A.K. Jain,

C. Jagadish (Institute of Physics, London, 1995).

1.14. *Transparent Electronics: From Synthesis to Applications,* edited by A. Facchetti and T. Marks (Wiley, New York, 2010).

1.15. C. Kilic and A. Zunger, Phys. Rev. Lett. **88**, 095501 (2002).

1.16. J.B. Varley, H. Peelaers, J. Phys. Condens. Matter **23**, 334212 (2011).

1.17. P.D.C. King, and T.D. Veal, J. Phys. Condens. Matter **23**, 334214 (2011).

1.18. F. Bekisli, M. Stavola, W. B. Fowler, L. Boatner, E. Spahr, and G. Lupke, Phys. Rev. B **84**, 035213 (2011).

1.19. *Metal Oxides: Chemistry & Applications,* edited by J.L.G. Fierro (Taylor & Francis Group, FL, 2006).

1.20. *Solid State Physics,* edited by F. Seitz and D. Turnbull (Academic Press, New York and London, 1959).

1.21. S.G. Koch, E.V. Lavrov, and J. Weber, Phys. Rev. Lett. **108**, 165501 (2012).

1.22. S. Limpijumnong, P. Reunchan, A. Janotti, and C.G. Van de Walle, Phys. Rev. B **80**, 193202 (2009).

1.23. M. Marezio, Acta Cryst. **20** (6), 723-728 (1966).

1.24. C.G. Van de Walle, Phys. Rev. Lett. **85** (5), 1012 (2000).

1.25. M.G. Wardle, J.P. Goss, Phys. Rev. Lett. **96**, 205504 (2006).

1.26. E.V. Lavrov, J. Weber, Phys. Rev. B **66**, 165205 (2002).

1.27. A. Janotti, C.G. Van de Walle, Nature Materials **6**, 44 (2007).

1.28. P.D.C. King, R.L. Lichti, Y.G. Celebi, Phys. Rev. B **80**, 081201 (2009).

1.29. T. Koida, H. Fujiwara, M. Kondo, Japanese Journal of Applied Physics **46** (28),

L685–L687 (2007).

1.30. W.M. Hlaing Oo, S. Tabatabaei, M.D. McCluskey, Phys. Rev. B **82**, 193201 (2010).

1.31. S. Lee and D.C. Paine, Appl. Phys. Lett. **102**, 052101 (2013).

1.32. J.H.W. De Wit, J. Sol. State Chem. **13**, 192 (1975).

1.33. J.H.W. De Wit, G. Van Unen, and M. Lahey, J. Phys. Chem. Solids **38**, 819 (1977).

Chapter 2: Experimental Methods

2.1: Local Vibrational Modes (LVMs)

With the increasing demand of semiconductors in industry, it is important to attain controlled doping of semiconductors along with tunable conductivity. In addition to altering the electronic properties and even transparency of semiconductors, impurities also affect the vibrational modes. Atoms in a crystalline solid collectively oscillate about their equilibrium positions, resulting in phonon vibrational modes. Introducing an impurity into a crystal breaks the translational symmetry and new vibrational modes may appear. Local vibrational modes are the characteristic vibrational modes of the atoms in a defect, which can be localized in real space and frequency space. If a defect replaces a heavier host atom, its vibrational frequency is likely to be higher than the upper-most phonon frequency. For example, hydrogen defects have vibrational frequencies 5-10 times the maximum phonon frequency, giving rise to sharp peaks in infrared-absorption and Raman-scattering spectra [2.1].

In the following, key results for local vibrational modes are summarized, following the recent review written by McClusky [2.1]. Considering a monatomic linear chain as a model, the local vibrational frequency can be written as,

$$\omega^2 = \omega_{\max}^2 \frac{M^2}{2Mm - m^2} \tag{2.1}$$

where $\omega_{max}=(4k/M)^{1/2}$ is the maximum frequency of the unperturbed linear chain, M is the lattice mass and m is the defect mass. Therefore, if $m<M$, there exists a LVM frequency above the highest phonon frequency.

In a compound semiconductor, numerical calculations in matrix form determine the eigenvalues ω and eigenvectors u_n (the displacement of the nth atom from its equilibrium position). The phonon density of states can then be plotted in a diagram as a function of eigenvalue ω. Figure 2.1 shows the density of vibrational states for undoped and ^{12}C-doped GaP (M_{Ga}=70, M_P=31, and with the carbon atom replacing phosphorus) by numerical calculation in the linear-chain model [2.1].

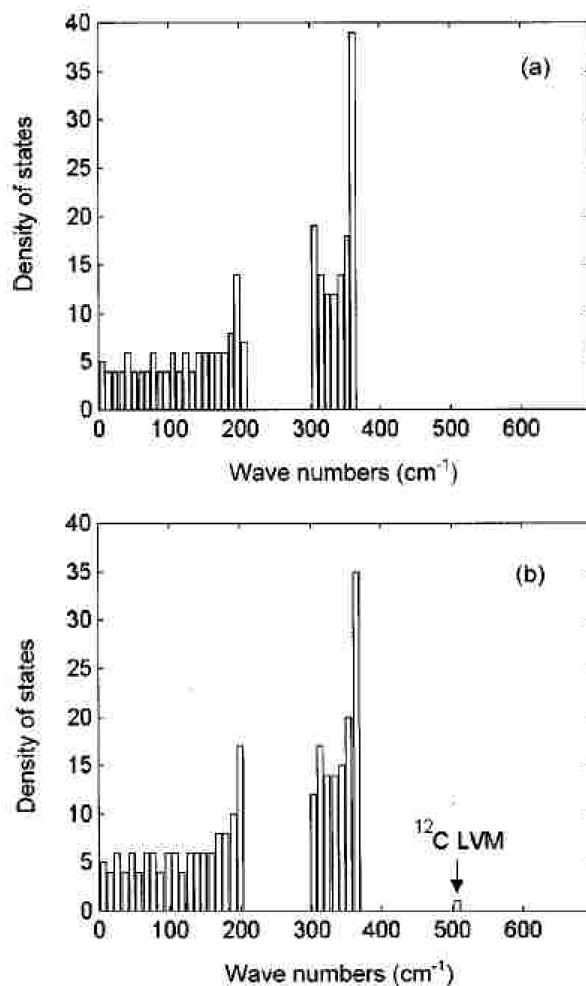

FIG. 2.1. Density of vibrational states for undoped and ^{12}C-doped GaP (M_1=70, M_2=31) by numerical calculation in a linear-chain model. A local vibrational mode due to ^{12}C appears at ω=510 cm^{-1} [2.1].

The diatomic molecule is also an effective empirical model that describes the frequencies and isotope shifts of LVMs [2.2][2.3]. An impurity atom with mass m is attached to a host atom with mass M. To account for the other host atoms, M is multiplied by an empirical constant x [2.2]. Therefore, the vibrational frequency of this diatomic molecule is,

$$\omega = \sqrt{k(1/xM + 1/m)} = \sqrt{k/\mu} \tag{2.2}$$

where μ is the reduced mass. Figure 2.2 shows the harmonic-oscillator and Morse potential energy functions for HCl, showing that the potential for a diatomic molecule is nearly harmonic at small amplitude.

If the defect atom is replaced with an isotope of itself, it will have a different mass, resulting in a different vibrational frequency ω (Fig. 2.3) [2.1]. For example, when hydrogen (m=1 amu) is replaced by deuterium (m=2 amu), the isotopic frequency ratio is given by

$$r = \omega_H / \omega_D = \sqrt{2\frac{xM+1}{xM+2}} \tag{2.3}$$

where ω_H and ω_D are the hydrogen and deuterium frequencies. Therefore, r is slightly less than, but close to, $\sqrt{2}$, which agrees with experimental results.

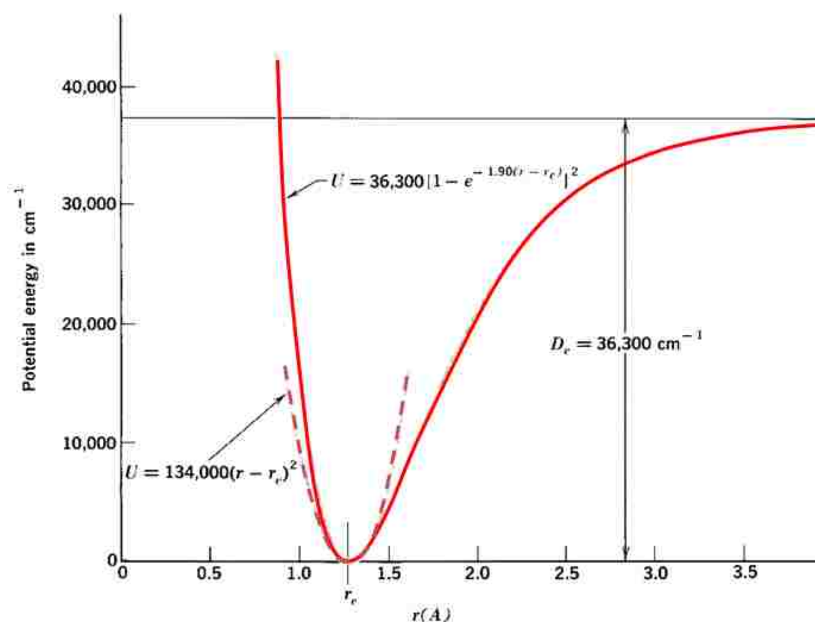

FIG. 2.2. The harmonic-oscillator (dashed line) and Morse (solid line) potential energy functions for HCl.

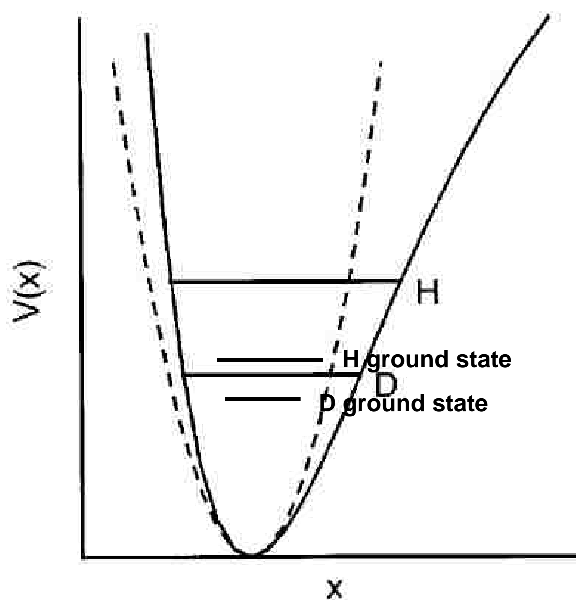

FIG. 2.3. The harmonic-oscillator (dashed line) and Morse (solid line) potential energy functions. Energy levels of hydrogen and deuterium are indicated by horizontal lines [2.1].

2.2: infrared absorption and free carrier absorption

One of the important experimental techniques for probing the defect vibrational frequencies is IR absorption spectroscopy. The defect atom absorbs a photon, which excites a vibrational mode and gives rise to a peak in the IR absorption spectrum.

This technique can be explained by an oscillating dipole model (two masses M and m, electric charge ±q), in which two masses are attached to each other by a spring with a spring constant k. Then the equation of motion is

$$\ddot{x} + \gamma \dot{x} + \omega_0^2 x = qE(t) / \mu \tag{2.4}$$

where γ is a damping constant, $\omega_0 = \sqrt{k/\mu}$ is the natural angular velocity, μ=1/(1/M +1/m) is the reduced mass and E(t) is the electric field. The solution of this differential equation gives the absorption cross section,

$$\sigma = \frac{\langle P \rangle}{ncE_0^2 / 8\pi} = \frac{4\pi q^2 \omega^2 \gamma}{n\mu c} \frac{1}{\left(\omega_0^2 - \omega^2\right)^2 + \gamma^2 \omega^2} \tag{2.5}$$

where σ is the absorption cross section, <P> is the time-averaged power dissipation, and n is the index of refraction. The peak in an IR spectrum appears at frequency $\omega = \omega_0$ and shows the maximum amplitude. Equation (2.5) indicates that σ is also related to the damping factor γ. σ as a function of ω and γ is shown in Fig. 2.4 [2.1].

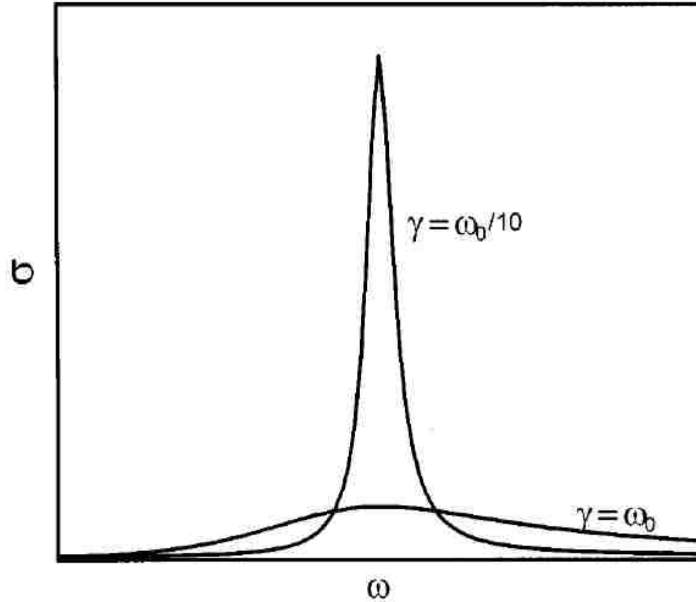

FIG. 2.4. The absorption cross section as a function of frequency ω and damping factor γ. γ is approximately the FWHM of the absorption peak [2.1].

The integrated absorption coefficient A_I is defined as

$$A_I = \int_0^\infty \alpha(\omega)d\omega = N\int_0^\infty \sigma(\omega)d\omega \tag{2.6}$$

where N is the defect concentration and α=σN is the absorption coefficient in units cm^{-1}. Combining Equations (2.5) and (2.6), yields,

$$A_I = N\frac{\pi q^2}{n\mu c^2} \tag{2.7}$$

Equation (2.7) shows the relationship between the integrated absorption coefficient and defect concentration, which will be utilized in Chapter 3.

Free carriers are electrons or holes that are free to move within the conduction or valence band. Free carrier absorption occurs when an electron (or hole) in the

semiconductor conduction (or valence) band absorbs a photon, making a transition to a higher energy state within the same band and is proportional to the carrier concentration [2.4]. Therefore, free carrier absorption is stronger in semiconductors with high free carrier concentrations (heavily doped semiconductors).

Free carrier absorption was thought to have a negative impact on the performance of devices such as silicon solar cells [2.5], thermophotovoltaic cells [2.6], and infrared photodetectors [2.7]. However, free carrier absorption is a strong function of the free carrier concentration and wavelength, which provides a means to characterize electron-hole plasmas and doped semiconductors. Free carrier absorption is important for our work because (1) doped semiconducting oxides with high free carrier concentration give rise to absorption in the IR frequency range, (2) the IR free carrier absorption can be correlated with the defects that introduce conductivity.

The classical theory of free carrier absorption is derived from Drude's model for the harmonic oscillation of unbound electrons in a fixed array of scattering nuclei [2.8]. The theory finds the free carrier absorption coefficient to be

$$\alpha_{FC} = \frac{Ne^2}{m^* \varepsilon_0 n c \tau} \frac{1}{\omega^2} \tag{2.8}$$

where N is the concentration of free carriers, e is the fundamental charge, m^* is the conductivity effective mass of the free carrier, ε_0 is the vacuum permittivity, n is the index of refraction, c is the speed of light, and τ is the mean time between collisions of

the oscillating particles and the nuclei. Equation (2.8) shows that the free carrier absorption coefficient is directly proportional to the free carrier concentration N. In addition, the absorption coefficient is inversely proportional to ω^2, meaning that the absorption is concentrated at lower frequencies, that is, in the infrared region that we focus on.

Figure 2.5(a) shows the absorption coefficient of a hydrogen doped ZnO crystal sample that had been annealed at elevated temperatures (50°C to 700°C) for the 2000 cm^{-1} to 3000 cm^{-1} frequency range [2.9]. Upon annealing, the absorption coefficient decays and is stable around 700°C. The free carrier absorption coefficient was calibrated with Hall measurements and was used to determine the free carrier concentration shown in Fig. 2.5(b).

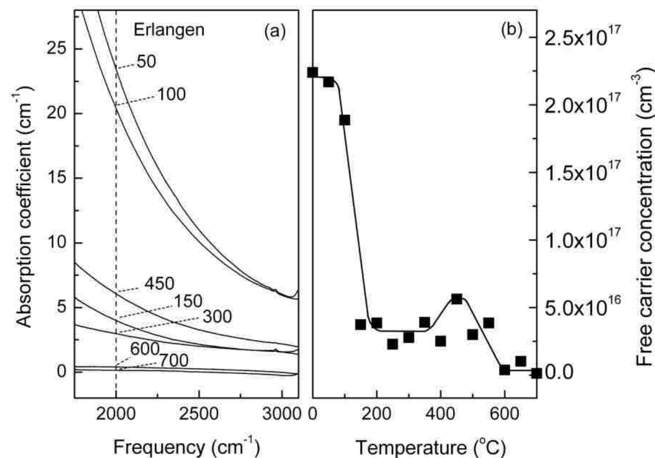

FIG. 2.5. A hydrogen doped ZnO crystal sample was annealed in flowing N_2 at elevated temperature from 50°C to 700°C. (a) the absorption coefficient at around 2000 cm^{-1} to 3000 cm^{-1}; (b) free carrier concentration as a function of annealing temperature [2.9].

2.3: Experimental Techniques

2.3.1: Fourier-transform infrared spectroscopy (FTIR)

Fourier transform infrared spectroscopy (FTIR) is a technique which is used to obtain an infrared spectrum of absorption, emission, or photoconductivity of a solid, liquid or gas. Compared to dispersive spectrometers, FTIR has the advantages of high spectral resolution, high signal-to-noise ratio, and the ability to collect spectral data in a wide spectral range within a short amount of time [2.10].

A FTIR spectrometer is based on the principle of the Michelson interferometer, which is shown in Fig. 2.6.

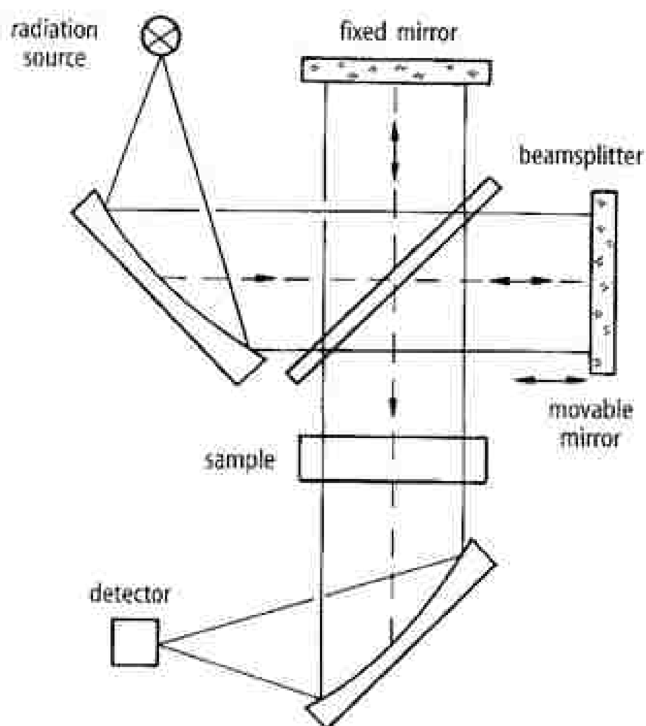

FIG. 2.6. Schematic diagram of a FTIR spectrometer.

A light beam from the IR source is directed at the beamsplitter and separated into two components. One component travels toward a fixed mirror and then is reflected back to the beam splitter. The other component is sent to the moving mirror and is then also reflected back to the beam splitter. These two components interfere with each other and recombine at the beamsplitter, travel through the sample, and finally impinge upon a detector. This beam is due to a superposition of the two light beams which have travelled along different optical paths. The optical path difference induced by the movable mirror leads to a phase difference of the two recombining waves.

To simplify this problem, consider a monochromatic light source at first. If the optical path difference between the fixed and movable mirrors is an integer multiple of the light wavelength (nλ), the two components will interfere constructively to give rise to maximum signal. On the contrary, if the optical path difference between the fixed and movable mirrors is an odd integer multiple of half of a wavelength ((n+1/2)λ), the two components will interfere destructively and give rise to a minimum signal. If we assume the moving mirror scans at a constant velocity, the signal intensity collected by the detector will be a cosine wave due to a continuous cycle of constructive and destructive interferences. The intensity recorded by the detector is,

$$I_0(\delta) = I_0\left\{1+\cos\left(\frac{2\pi\delta}{\lambda}\right)\right\} \tag{2.9}$$

where λ is the wavelength, δ is the optical path difference, and I_0 is half of the intensity of incoming light. The Fourier Transform of the cosine wave results in a single sharp line (Fig. 2.7(a)).

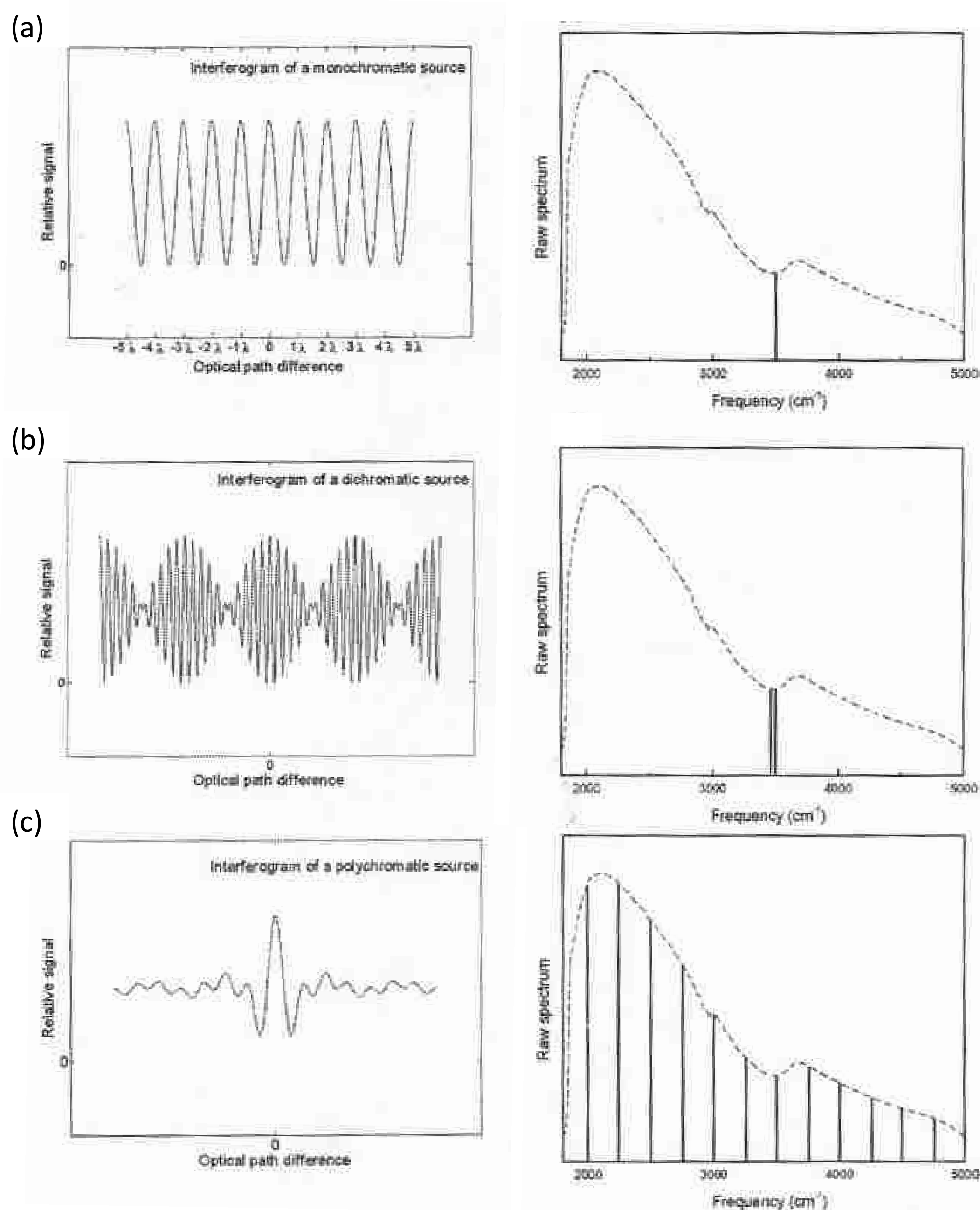

FIG. 2.7. Interferograms and their corresponding Fourier transformed spectra for (a) a single frequency, (b) two close frequencies, (c) broad continuous frequencies. Especially at the zero optical path difference (ZPD) position in the interferogram (c), a large signal is observed because all wavelengths contribute constructively.

If the IR source emits additionally a second wavelength with a very small wavelength difference, we will get an interferogram, which is the superposition of the two single interferograms (Fig. 2.7(b)). If the radiation source emits a broad continuous spectrum, the result now will be the superposition of all single wavelength interferograms and looks significantly more complex (Fig. 2.7(c)).

Considering a monochromatic light source again, Equation (2.9) has the first term as a constant and the second term $I_0\cos(2\pi\delta/\lambda)$ as the interferogram. In a FTIR spectrometer, an IR light source has a continuum of frequencies. Therefore, the interferogram is given by

$$I(\delta) = \int_{-\infty}^{\infty} I(\nu)\cos(2\pi\delta\nu)d\nu \tag{2.10}$$

with ν =1/λ. A symmetric interferogram can be converted into its corresponding spectrum by a Fourier transform:

$$I(\nu) = \int_{-\infty}^{\infty} I(\delta)\cos(2\pi\delta\nu)d\delta \tag{2.11}$$

The following is an example of a Fourier Transform spectrum. Fig. 2.8(a) shows an interferogram obtained from an In_2O_3 sample measurement and Fig. 2.8(b) is its corresponding raw spectrum after Fourier transform. To eliminate the influence of the atmosphere and optical properties of the spectrometer on the spectrum, the raw spectrum is divided by a reference spectrum, which produces the transmission spectrum. The absorbance spectrum is more often used, which is determined by taking the $-\log_{10}$ of the transmission spectrum. For different cases, the reference

spectrum might have different forms. For example, it can be a raw spectrum measured with no sample (empty cryostat), or it can also be a raw spectrum measured for a sample without defects to emphasize the emergence of defect absorption peaks after the sample is doped. A reference spectrum (no-sample condition) is shown in Fig. 2.8(c). Fig. 2.8(d) shows the absorbance spectrum of the raw spectrum (Fig. 2.8(b)) that results from using Fig. 2.8(c) as a reference spectrum. The spectrum in Fig. 2.8(d) is dominated by the absorption due to free electrons in the In_2O_3 sample.

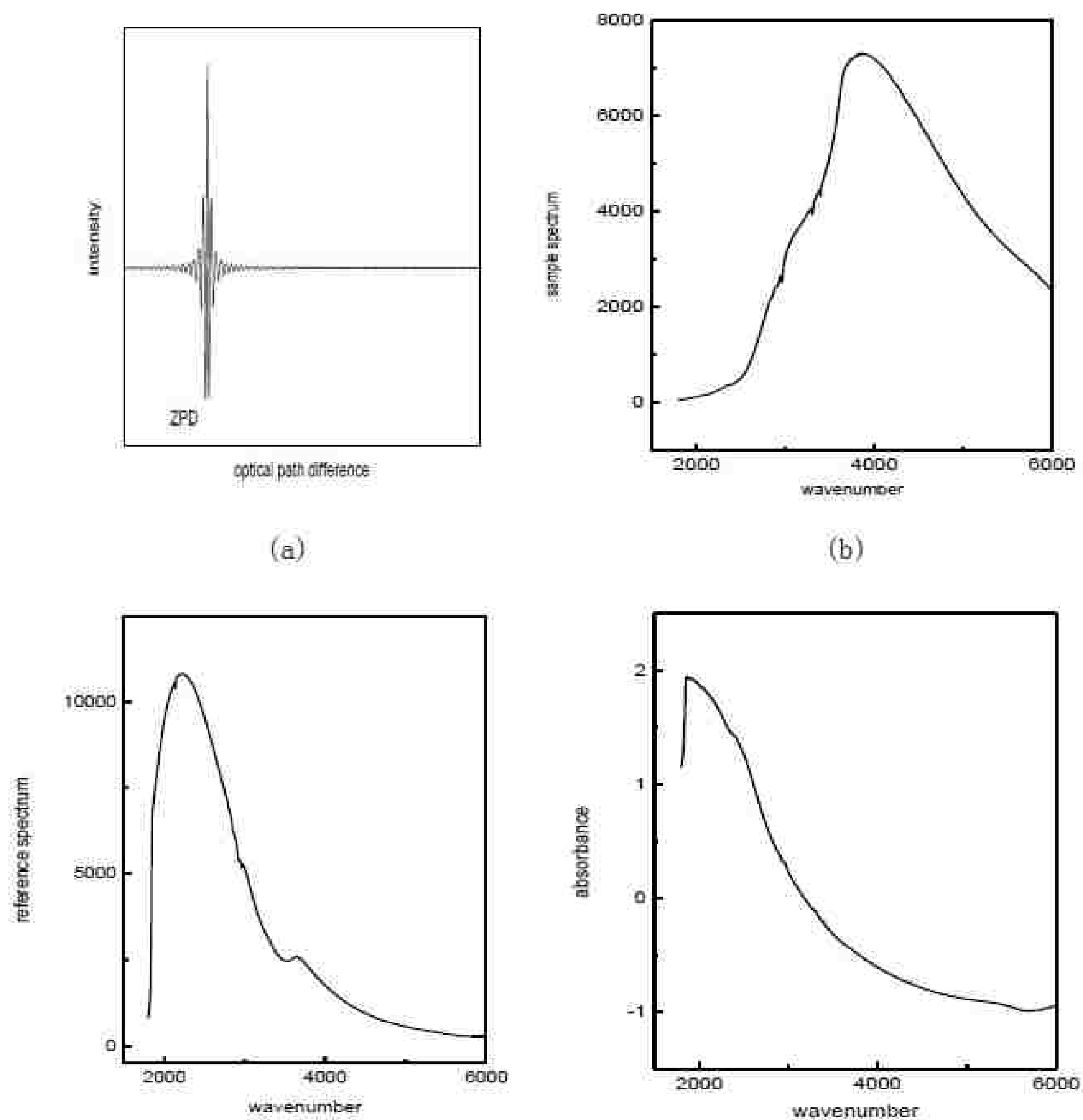

FIG. 2.8. A hydrogen doped In_2O_3 sample; (a) interferogram, (b) sample raw spectrum, (c) reference spectrum, (d) absorbance spectrum

2.3.2: Instrumentation

In our study, measurements were performed with a Bomem DA 3.16 FTIR spectrometer which is controlled by a computer via a PCDA3INT VAX interface. The spectrometer configuration and parameters can be controlled through the Bomem

PCDA data acquisition software which allows a user to select and modify experimental parameters, collect the interferogram and perform a Fast Fourier Transform (FFT) to get the corresponding raw spectrum. Thermo Scientific GRAMS/32 software is then used to process and analyze the raw spectrum (absorbance spectrum, baseline correction, smoothing, etc.). In addition, other software packages like Peak Fit V4 and Origin 8 are also used for data analysis, curve fitting, and curve plotting in this study.

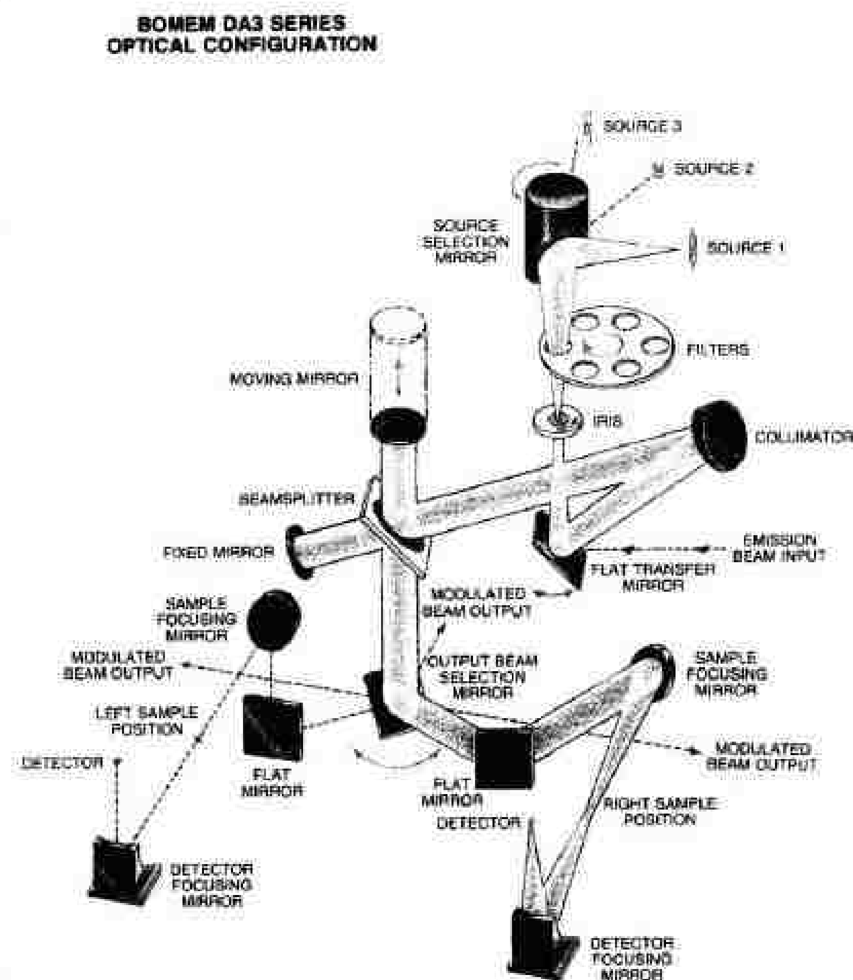

FIG. 2.9. The optical configuration of Bomem DA 3.16 spectrometer.

Fig. 2.9 shows the optical configuration of the Bomem spectrometer. There are two light sources used in the Bomem spectrometer at Lehigh that cover wide frequency ranges, a silicon carbide globar source (mid-IR) and a quartz halogen source (near IR-visible). In our study, the silicon carbide globar source is primarily used since the mid-IR frequency range, which contains the free carrier absorption and defect absorption information, was of interest for our analysis. The light from the source passes through a six-position rotary filter and an iris which has different diameter settings between 0.5 - 10 mm. Before the measurement, PCDA software is used to select the desired aperture and filter type to communicate with the set-up so that the optimal throughput can be achieved. The light is then reflected from a collimating mirror and transferred to the beam splitter. Two types of beam splitters were available to cover different frequency ranges, a KBr beam splitter coated with Ge/ZnSe (used primarily in this study) for the 450 cm^{-1}-5000 cm^{-1} range and a quartz beam splitter coated with TiO_2 for the 4000 cm^{-1}-27000 cm^{-1} range. The light is split into two components by the beam splitter, which interfere with each other and recombine at the beam splitter. Then the light is focused and directed toward the sample with the use of a set of parabolic mirrors and finally to the detector. Three types of detectors are available for different frequency ranges to be measured. An InSb detector measures IR radiation in the range 1800 cm^{-1}-8000 cm^{-1} (covering the free carrier absorption and the hydrogen defect absorption characteristic of metal oxides) and was used in most experiments. The other two detectors, a HgCdTe (MCT) detector and a Si bolometer, are available to cover different ranges, 800-5000 cm^{-1}

and 350-2500 cm^{-1}, respectively.

Most of the measurements were performed at 4K or 77K temperatures in order to reduce the thermal vibration of the host crystal lattice. The sample was mounted inside one of the two available cryostats, which can transfer liquid He or N_2 to the sample. The cryostat used most is an Air Products Heli-Tran cryostat, which is a continuous flow cryostat that has input and output CaF_2 windows transmitting more than 90% of the light from the visible to the near IR range. CsI windows are also available for measurements in the far IR. This cryostat was used in our In_2O_3 studies. The second cryostat is an Oxford model CF1204, which is also a continuous flow cryostat that cools the sample space with He exchange gas. A schematic of this cryostat is shown in Fig. 2.10. The design of this cryostat separates the vacuum layer and the sample chamber, which speeds up the transition between consecutive experiments using different samples. The Oxford Cryostat has 6 windows, 2 outer vacuum case windows, 2 inner sample windows, and 2 radiation shield windows. The radiation shield between the outer vacuum and inner sample windows is also cooled to cryogenic temperature. Therefore, the temperature in the sample chamber is better protected from the effects of thermal radiation due to entering light that is at room temperature. Compared to the Air Products cryostat, the Oxford cryostat has a more accurate temperature and better temperature stability, which enables a series of experiments with measurement temperature steps as low as 0.5 K. Measuring an IR spectrum of the sample under stress with polarized light is a useful method to

investigate the sample crystal structure and possible defect sites. The Oxford cryostat can be combined with a stress apparatus.

In order to maintain the vacuum in IR spectroscopy and minimize the effects of background features, such as absorption of light by water vapor, CO_2 and oil, a mechanical pump is used for generating a vacuum in the spectrometer and a turbo pump is used for the cryostat. Liquid nitrogen cold traps inside the spectrometer and also on the turbo pump vacuum line are used to further reduce the absorption by water vapor, oil, and CO_2.

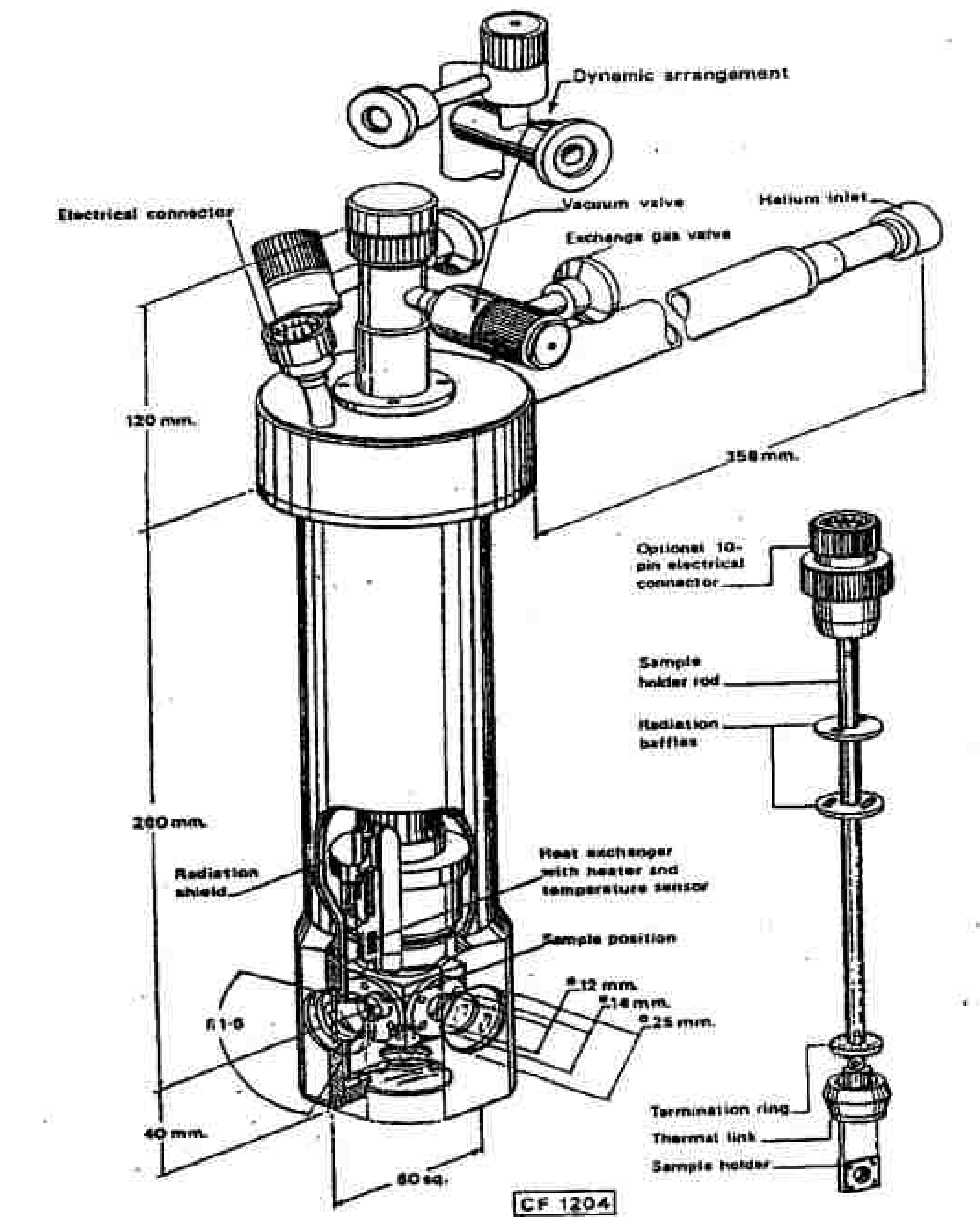

FIG. 2.10. Illustration of Oxford CF1204 cryostat

2.3.3: Other Techniques - Raman spectroscopy & Hall effect

Raman Spectroscopy

Raman spectroscopy is a measurement technique that can be used to observe vibrational, rotational, and other low-frequency modes in a system, which relies on inelastic scattering of monochromatic light, usually from a laser in the visible, near infrared, or near ultraviolet range.

A Raman system typically consists of four major components (Fig. 2.11); an excitation source (laser); a sample illumination system and collection lenses; a wavelength selector (a Filter and Spectrophotometer); and a detector (CCD array). A sample is illuminated with a laser beam in the ultraviolet, visible, or near infrared range. Scattered light is collected with lenses and sent through an interference filter and a scanning double spectrophotometer to obtain a Raman spectrum.

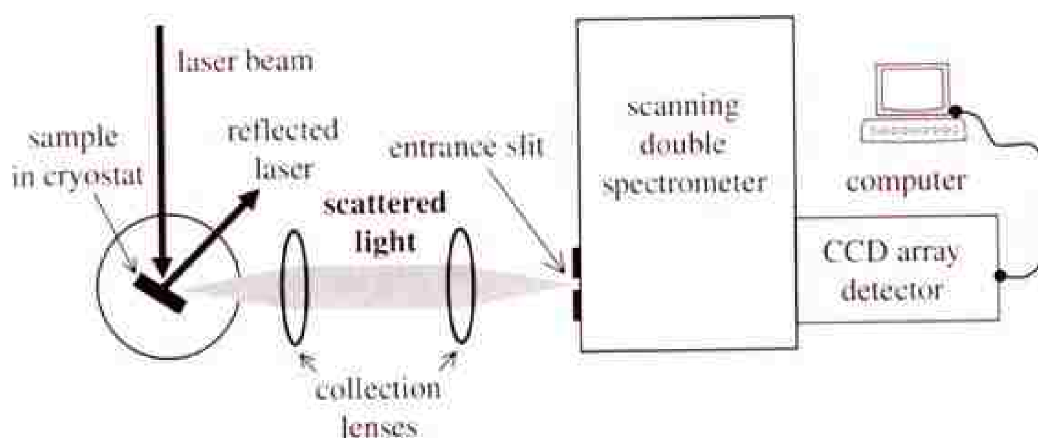

FIG. 2.11. Configuration of a Raman system

When monochromatic radiation is incident upon a sample, this light will interact with the sample. A photon excites the molecule in either the ground state or an excited state, which results in the molecule being in a virtual energy state for a short period of time before light is scattered. Light scattered from a molecule has several components - Rayleigh scattering (elastic, same energy) and the Stokes (inelastic, lower energy) and Anti-Stokes (inelastic, higher energy) Raman scattering (Fig. 2.12).

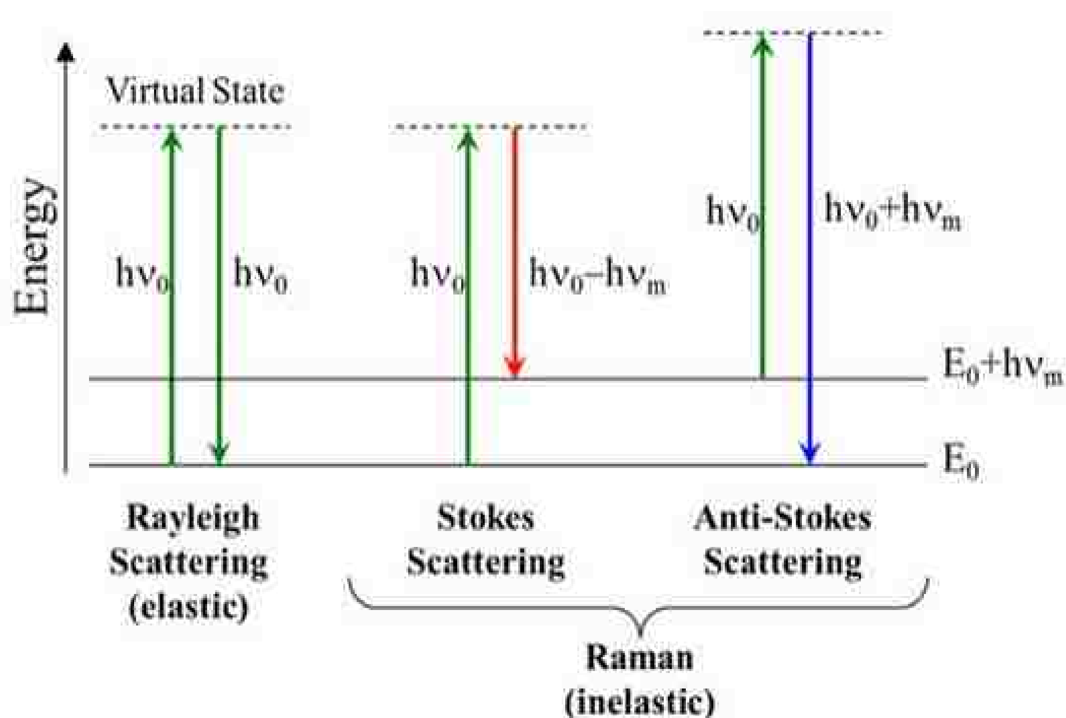

FIG. 2.12. Transitions for Rayleigh (elastic) and Raman (inelastic) Scattering.

For Stokes scattering, the energy $\hbar\omega_s$ of a scattered photon differs from that of the incoming photon $\hbar\omega_L$ by

$$\hbar\omega_s = \hbar\omega_L - \hbar\omega_{LVM} \quad (2.12)$$

where ω_{LVM} is the frequency of the local vibrational mode.

A schematic diagram of a Stokes Raman shift is shown in Fig. 2.13. In our study, Raman spectroscopy was used to investigate the phonon modes in In_2O_3, which are not easy to measure by IR spectroscopy.

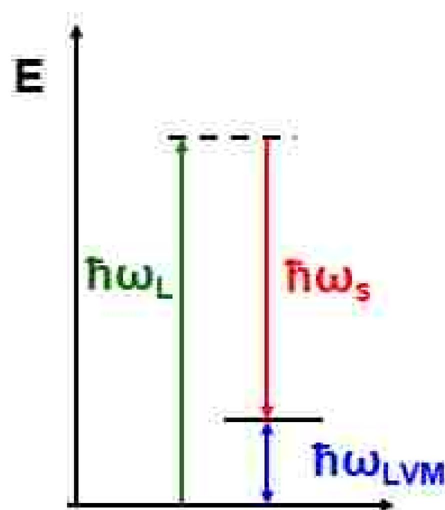

FIG. 2.13. Schematic diagram of Raman shift (Stokes scattering). A Raman shift gives the local vibrational mode frequency.

Hall Effect

The Hall effect is the production of a voltage difference across an electrical conductor, transverse to an electric current in the conductor and a magnetic field perpendicular to the current, which is a standard method to study the carrier concentration and mobility in semiconductors [2.11].

Fig. 2.14 shows a schematic of a Hall Effect measurement. Initially, the carriers experience a Lorentz force and follow the curved arrow, due to the magnetic force. Moving charges accumulate on one face of the material. This leaves equal and opposite charges exposed on the other face, which creates an electric field. In steady-state, the electric field will be strong enough to cancel out the Lorentz force, so that the carriers follow the straight arrow.

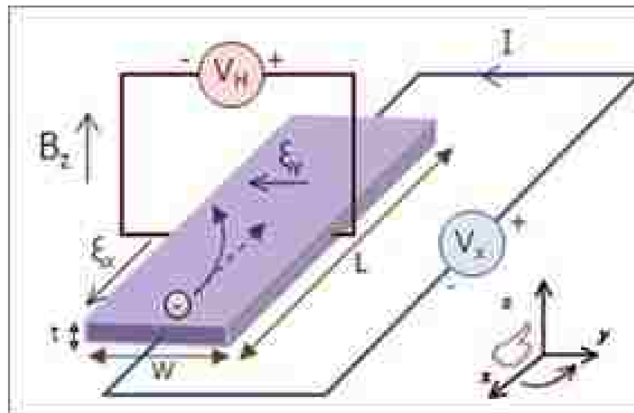

FIG. 2.14. Hall Effect measurement geometry.

In a Hall effect measurement, the Hall coefficient is defined as

$$R_H = \frac{E_y}{j_x B} \tag{2.13}$$

where E_y is the induced electric field, j_x is the current density of the carriers and B is the magnetic field.

Semiconductors usually have a more complicated Hall coefficient than conductors since both electrons and holes may be present in different concentrations

and have different mobilities. For moderate magnetic fields, the Hall coefficient is [2.12],

$$R_H = \frac{p\mu_h^2 - n\mu_e^2}{e(p\mu_h + n\mu_e)^2} \tag{2.14}$$

where the n is the electron concentration, p is the hole concentration, μ_e is the electron mobility, μ_h is the hole mobility and e is the absolute value of the electronic charge. In our study, Hall effect measurements were performed to determine the free carrier concentration, which will be discussed when we calibrate the IR lines in Chapter 3.

2.4: Diffusion

Atomic diffusion is one of the most important processes employed in the semiconductor industry. It is used at least once in the manufacture of most devices. As for fundamental research, there are two main reasons for studying diffusion in solids [2.13]. First, understanding diffusion benefits the understanding of the changes in solids at high temperatures. The second reason for studying diffusion is to learn more about how atoms move in solids. Diffusion experiments are used to investigate the diffusion coefficient, which is theoretically related to the concentration and movement of point defects in semiconductors. In this section, a few results are summarized from popular monographs on diffusion [2.13][2.14].

Fick's first law states that the diffusion flux is proportional to a concentration gradient and defines the diffusion coefficient D.

$$J = -D\frac{\partial C}{\partial x} \tag{2.15}$$

Fick's second law predicts how diffusion causes the concentration to change with time [2.14]. In one dimension,

$$\frac{\partial C}{\partial t} = D\frac{\partial^2 C}{\partial x^2} \tag{2.16}$$

Here, C is the concentration, t is time, x is the diffusion depth, and D is the diffusion coefficient.

2.4.1: Indiffusion experiments

Imagine plating a thin film of a diffusant onto the flat face of a semiconductor slice. The film then becomes the diffusion source while it is annealed for time t. The thin-film solution of this equation is a Gaussian function:

$$C = \frac{A}{t^{1/2}}\exp(-\frac{x^2}{4Dt}) \tag{2.17}$$

Now consider a pair of semi-infinite specimens, one occupying the space $-\infty < x < 0$, the other occupying $0 < x < \infty$. They are joined at the plane x=0, which is perpendicular to the length of the bars. The first bar is homogenously doped with some solute to a concentration C', the other contains no solute. In this case, the solution to Eq. (2.16) can be written as the complementary error function.

$$C = \frac{C'}{2}\operatorname{erfc}\frac{x}{2(Dt)^{1/2}} \tag{2.18}$$

Indiffusion experiments for H in In_2O_3 are described in Section 3.3.4 and were performed by thinning a bulk H-doped In_2O_3 sample. To investigate the distribution of hydrogen concentration among each sample layer, the H-doped sample was thinned on both sides and the IR spectrum was measured to show the hydrogen absorbance, which is related to the hydrogen concentration C. With this procedure, the diffusion coefficient D could be determined. More details about our indiffusion experiments and data will be shown in Chapter 3.3.4.

2.4.2: Outdiffusion experiments

Outdiffusion occurs from an initially homogeneously doped sample. It is first assumed that there exist solutions which are the product of a function only of time T(t) and a function of distance X(x). That is, it is assumed that

$$c(x,t) = X(x)T(t) \tag{2.19}$$

If Eq. (2.19) is substituted into Fick's second law Eq. (2.16), the result is

$$\frac{1}{DT}\frac{dT}{dt} = \frac{1}{X}\frac{d^2X}{dx^2} \tag{2.20}$$

Since x and t can be varied independently, Eq. (2.20) can be satisfied only if both sides of the equation are equal to a constant. This constant will be designated as $-\lambda^2$. The differential equations in time and distance are then

$$\frac{1}{T}\frac{dT}{dt} = -\lambda^2 D \tag{2.21}$$

$$\frac{d^2X}{dx^2} + \lambda^2 X = 0 \tag{2.22}$$

Solving these two equations gives the most general form of the product solution,

$$c(x,t)=\sum_{n=1}^{\infty}(A_n \sin\lambda_n x + B_n \cos\lambda_n x)\exp(-\lambda_n^2 Dt) \quad (2.23)$$

Considering diffusion out of a slab of thickness h, the boundary conditions to be assumed are

$c=c_0$ for $0<x<h$, at $t=0$

$c=0$ for $x=h$ and $x=0$, at $t>0$

By setting B_n equal to zero, A_n and λ_n can be solved. The solution is

$$c(x,t)=\frac{4c_0}{\pi}\sum_{j=0}^{\infty}\frac{1}{2j+1}\sin\frac{(2j+1)\pi x}{h}\exp[-\left(\frac{(2j+1)\pi}{h}\right)^2 Dt] \quad (2.24)$$

After a short time t' has elapsed, c(x,t) can be represented by only a few terms and can be given by a sine wave. Considering the ratio of the maximum values of the first and second terms, this ratio R is given by

$$R=3\exp\frac{8\pi^2 Dt'}{h^2} \quad (2.25)$$

For $h=2\sqrt{Dt}$, R is about 150, which means for $t\geq h^2/4D$, the error in using the first term to represent c(x,t) is less than 1% at all points. In reality, it is difficult to determine the concentration at various depths in a slab, and what can be experimentally determined is the average defect concentration $\bar{c}$ remaining in the slab. Integrating (2.24) yields

$$\bar{c}(t)=\frac{1}{h}\int_0^h c(x,t)dx=\frac{8c_0}{\pi^2}\sum_{j=0}^{\infty}\frac{1}{(2j+1)^2}\exp\left[-\left(\frac{(2j+1)\pi}{h}\right)^2 Dt\right] \quad (2.26)$$

For $\bar{c}\leq 0.8c_0$, the first term is an excellent approximation to the solution. Therefore, the solution can be written as

$$\frac{\bar{c}}{c_0} = \frac{8}{\pi^2}\exp\left(-\frac{t}{\tau}\right) \quad (2.27)$$

where $\tau \equiv h^2 / \pi^2 D$ is called the relaxation time.

For outdiffusion experiments, an as-grown In_2O_3 sample was hydrogenated by an anneal (1h) in an H_2 ambient at 500°C. The sample was then annealed isothermally (400°C) in a flowing N_2 ambient for different accumulated times (30min, 1h, 2h…). The O-H centers and free carriers were reduced for accumulated annealing times, and the outdiffusion coefficient D could be determined from the relaxation time, τ, and sample layer thickness, h, that were measured. Chapter 3.3.4 will show the outdiffusion experiments and data analysis in more detail.

References

2.1. M.D. McCluskey, J. Appl. Phys. **87**(8), 3593-3617 (2000).

2.2. R.C. Newman, *Semiconductors and Semimetals,* edited by E. Weber (Academic, New York, 1993) Vol. **38**, Chap. 4.

2.3. E.E. Haller, Mater. Res. Soc. Symp. Proc. **378**, 547 (1995).

2.4. S.C. Baker-Finch, K.R. McIntosh, D. Yan, J. Appl. Phys. **116**, 063106 (2014).

2.5. T. Tiedje, E. Yablonovitch, G.D. Cody, and B.G. Brooks, IEEE Trans. Electron Devices **31**(5), 711–716 (1984).

2.6. M.B. Clevenger, C.S. Murray, and D.R. Riley, Mater. Res. Soc. Proc. **485**, 291–296 (1997).

2.7. M. Casalino, G. Coppola, M. Iodice, I. Rendina, and L. Sirleto, Sensors **10**, 10571–10600 (2010).

2.8. M. Fox, *Optical Properties of Solids* (Oxford University Press, New York, 2001).

2.9. G.A. Shi, M. Stavola, Phys. Rev. B **72**, 195211 (2005).

2.10. R.J. Bell, *Introductory Fourier Transform Spectroscopy* (Academic, New York, 1972).

2.11. E. Hall, American Journal of Mathematics, **2** (3), 287–292 (1879).

2.12. S. Kasap, *Hall Effect in Semiconductors,* 2001.

2.13. P.G. Shewmon, *Diffusion in solids* (McGraw-Hill Book Company, New York, 1963).

2.14. B. Tuck, *Introduction to diffusion in semiconductors* (Peter Peregrinus Ltd., Stevenage, 1974).

Chapter 3:

Hydrogen centers and the conductivity of In_2O_3 single crystals

3.1: Introduction

The transparent conducting oxides (TCO's) combine high electrical conductivity with transparency in the visible region of the spectrum [3.1-3.4]. In spite of their decades-long applications as transparent electrical contacts, in circuitry, and as coatings for low-emissivity windows, the mechanisms for the conductivity of TCO's are only now being clarified. Oxygen vacancies and cation interstitials traditionally have been invoked as the sources of conductivity. In recent studies, however, hydrogen impurities have been found to be the dominant shallow donors in several important cases [3.5-3.10].

In_2O_3, a prototypical transparent conducting oxide, has the cubic bixbyite structure with a conventional unit cell that contains 80 atoms [3.11]. The oxygen sites are all equivalent. There are two inequivalent In sites, In(1) (25%) and In(2) (75%). The In(1) site is more symmetrical and has six equivalent In-O bonds. The In(2) site is less symmetrical and has three inequivalent pairs of In-O bonds with no linear O-In-O bonds.   Ref. 3.12 provides further details regarding the bixbyite structure.

The role played by hydrogen impurities in the conductivity of indium oxide (In_2O_3) has been controversial. Some studies, based on the effect of oxygen partial pressure in growth or annealing environments, argue that oxygen vacancies are the cause of the conductivity of In_2O_3 [3.12-3.15]. However, there is a growing body of theoretical and experimental work which finds that hydrogen centers can be important shallow

donors in In_2O_3. Muon-spin-resonance experiments find that implanted muons, whose properties mimic those of hydrogen, form shallow donors in In_2O_3 [3.16]. In_2O_3 thin films containing hydrogen show n-type conductivity with high mobility [3.17], and theory finds that interstitial hydrogen (H_i^+) and hydrogen trapped at an oxygen vacancy (H_O^+) are shallow donors that can give rise to n-type conductivity or compensate acceptors in In_2O_3 [3.12].

In the present chapter, infrared (IR) spectroscopy, Hall effect measurements, and theory are used to investigate the microscopic properties of hydrogen centers in In_2O_3 single crystals and the role that hydrogen plays in giving rise to conductivity.

3.2: Experimental Procedures

The In_2O_3 samples used in our experiments were bulk single crystals grown by the flux method [3.18] at the Oak Ridge National Laboratory (ORNL) by Lynn Boatner and had typical dimensions of 3 x 3 x 1 mm^3. Most as-grown samples were pale yellow in color. The properties of similar In_2O_3 crystals, also grown at ORNL, have been reported recently [3.19]. The as-grown crystals were found to have a high resistivity (2 x 10^5 Ω-cm). A few additional In_2O_3 samples that were gray or green in color were also examined in our experiments.

To introduce additional hydrogen or deuterium, In_2O_3 samples were placed in sealed quartz ampoules filled with H_2 or D_2 gas (2/3 atm at room temperature), annealed at elevated temperature, and cooled to room temperature by withdrawing the sealed ampoule from the furnace. These anneals in H_2 or D_2 produced an opaque

layer of In at the sample surface that could be removed by soaking in a 1:4 mixture of HNO_3/H_2O.

IR absorption spectra were measured with a Bomem DA.3 Fourier transform infrared spectrometer. O-H and O-D vibrational modes were measured for In_2O_3 samples held at 4.2 or 77 K with an InSb detector. Samples were cooled with a Helitran continuous-flow cryostat. The absorption due to free carriers [3.20] was measured for the In_2O_3 samples to provide a contact-free method to probe the free-carrier concentration that is convenient for annealing experiments.

Raman measurements were performed by Sandro Koch at the Dresden University of Technology. A 90° geometry was used with the frequency doubled 532 nm line of a Nd:YVO_4 laser for excitation. The scattered light was analyzed using a single grating spectrometer with a cooled Si CCD detector array.

To probe the reactions and thermal stabilities of the various hydrogen-containing centers, annealing treatments were performed in a tube furnace with a flowing He ambient.

3.3: Experimental Results

As-grown In_2O_3 single crystals that were initially pale yellow in color showed no substantial IR absorption arising from free carriers. Samples were annealed in H_2 or D_2 ambients to introduce H or D. For long annealing treatments in H_2 or D_2 (>1 hr) at temperatures above 500 °C, samples became dark in color and were opaque in the mid-IR spectral region of interest to us here. We selected temperatures near 450 to

500 °C and H_2 or D_2 treatment times near 30 to 60 min to produce hydrogenated (or deuterated) samples that were deep red in color and sufficiently transparent for IR measurements.

3.3.1: Free-carrier absorption and O-H vibrational lines

The introduction of H or D into In_2O_3 produced the broad absorption characteristic of free carriers that increases in strength at low frequency [Fig. 3.1(a)] [3.20]. Furthermore, several O-H stretching modes were also introduced [Fig. 3.1(b)].

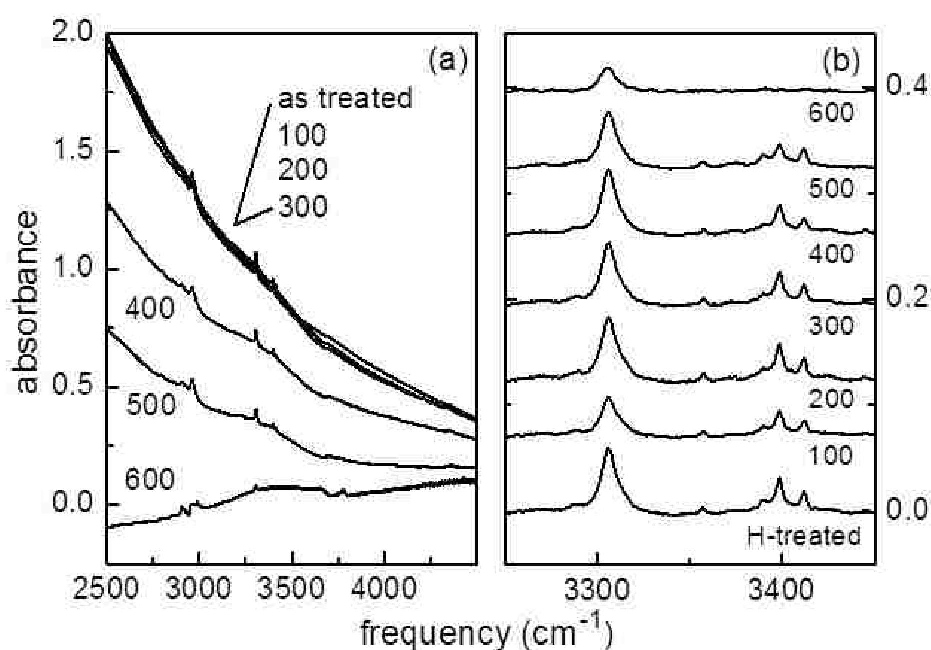

FIG. 3.1. A selection of IR absorption spectra (T = 4.2 K, resolution = 1 cm^{-1}) for an In_2O_3 sample that initially had been hydrogenated by an anneal (30 min) in an H_2 ambient at 500°C. The sample was then annealed sequentially in flowing He at the temperatures shown in °C. (a) The absorption due to free carriers. (b) The IR absorption lines in the O-H stretching region. These spectra were baseline corrected to remove the contribution from free carriers.

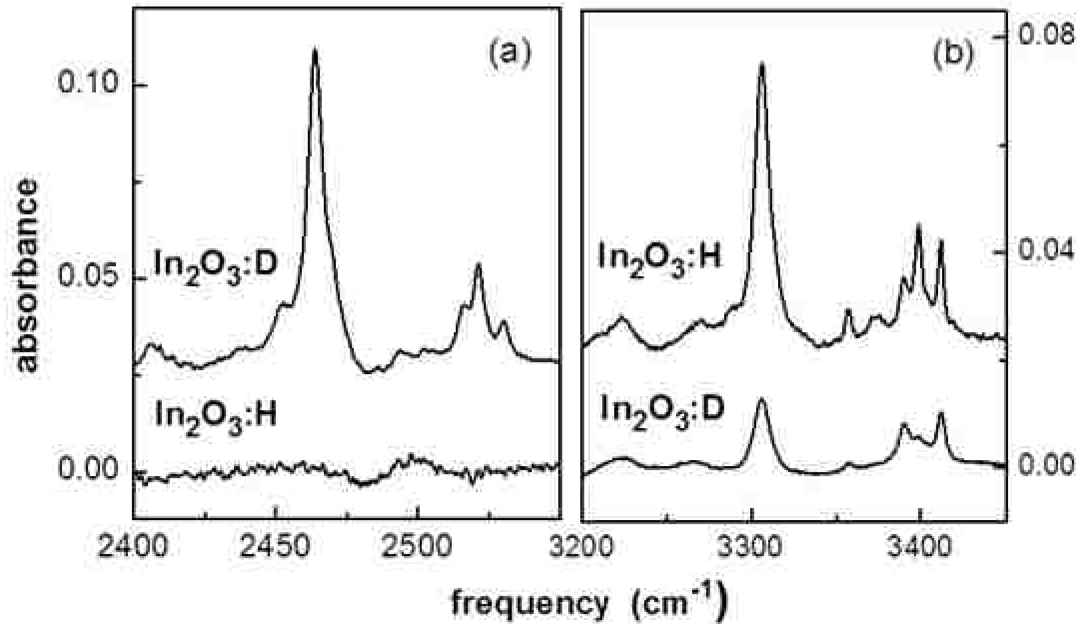

FIG. 3.2. IR absorption spectra (4.2 K, resolution = 1 cm^{-1}) for In_2O_3 samples containing D and H. Spectra were baseline corrected to remove the contribution from free carriers. The sample for the upper spectrum in (a) had been deuterated by annealing in a D_2 ambient (60 min) at 500°C. It was then annealed in flowing He at 550°C to increase its transparency and to produce the O-D lines that are shown. The sample for the upper spectrum in (b) had been hydrogenated by annealing (30 min) in an H_2 ambient at 500°C and subsequently annealed (30 min) at 550°C. [The lower spectrum in (a) shows the D-stretching region for a hydrogenated sample and the lower spectrum in (b) shows the H-stretching region for a deuterated sample.]

Figure 3.2 shows IR spectra (4.2 K) for In_2O_3 samples that had been treated in D_2 or H_2. The upper spectrum in Fig. 2(a) for the deuterated sample shows 9 resolved IR lines. The upper spectrum in Fig. 2(b) for the hydrogenated sample also shows 9 IR lines. The dominant IR lines are at 3306 cm^{-1} for H and at 2464 cm^{-1} for D. The line at

2464 cm^{-1} has a partially resolved shoulder at 2469 cm^{-1}. The line at 3306 cm^{-1} is slightly asymmetric, suggesting the presence of an unresolved line at 3316 cm^{-1} that is the isotopic partner of the shoulder at 2469 cm^{-1}. [The lower spectrum shown in Fig. 3.2(a) for a hydrogenated sample is featureless in this region. The lower spectrum in Fig. 3.2(b) shows the spectral features arising from H that typically remained in samples even after treatment in a D_2 ambient.]

Table 3.1. Vibrational frequencies of O-H (O-D) modes seen for hydrogenated (deuterated) In_2O_3 single crystals. A possible shoulder giving rise to the asymmetry of the 3306 cm^{-1} line is unresolved.

ω_H (cm^{-1})	ω_D (cm^{-1})	r
3225	2407	1.340
3271	2436	1.343
3290	2455	1.340
3306	2464	1.342
3316 (unres.)	2469	1.343
3357	2494	1.346
3373	2504	1.347
3390	2516	1.347
3398	2521	1.348
3411	2530	1.348

The vibrational frequencies of these lines are listed in Table 3.1. The ratios of the corresponding line frequencies in the H and D spectra are near 1.35, consistent with vibrational modes of H or D bonded to a light element like oxygen [3.21]. The high frequency of the vibrational lines and the value of the isotopic ratio r lead to the assignment of the lines listed in Table 3.1 to O-H and O-D stretching modes.

3.3.2: Annealing and thinning experiments

Figure 3.1 shows that both the free-carrier absorption and the 3306 cm^{-1} O-H line are annealed away together for annealing temperatures in the 500 to 600°C range. Similar annealing experiments were performed for a sample treated in a D_2 ambient (Fig. 3.3). (Samples annealed in H_2 or D_2 were red in color following treatment and returned to pale yellow after the H or D had been annealed away.) The correlation between the free-carrier absorption and the intensities of the O-H and O-D lines at 3306 and 2464 cm^{-1} in annealing experiments leads us to assign these vibrational lines to interstitial H^+ and D^+ shallow-donor centers predicted by theory [3.12].

Isothermal anneal experiments were performed to investigate the correlation between the free carrier absorption and the hydrogen defects in more detail. An as-grown In_2O_3 yellow sample had been hydrogenated by an anneal (1h) in an H_2 ambient at 500°C. This sample was then annealed isothermally (400°C) in a flowing N_2 ambient for different accumulated times (30min 1h, 2h…). The raw spectra were measured after each isothermal anneal and the air reference spectrum (empty sample holder) was measured before all annealing treatments. Absorbance spectra

were plotted in Fig. 3.4(a) with the total annealing time labeled for each. The corresponding IR absorption lines in the O-H stretching region are shown in Fig. 3.4(b). The sample was annealed (step by step) for 24 hours in total at 400°C. A significant decay of the free carrier absorption and of the intensity of the O-H lines was observed.

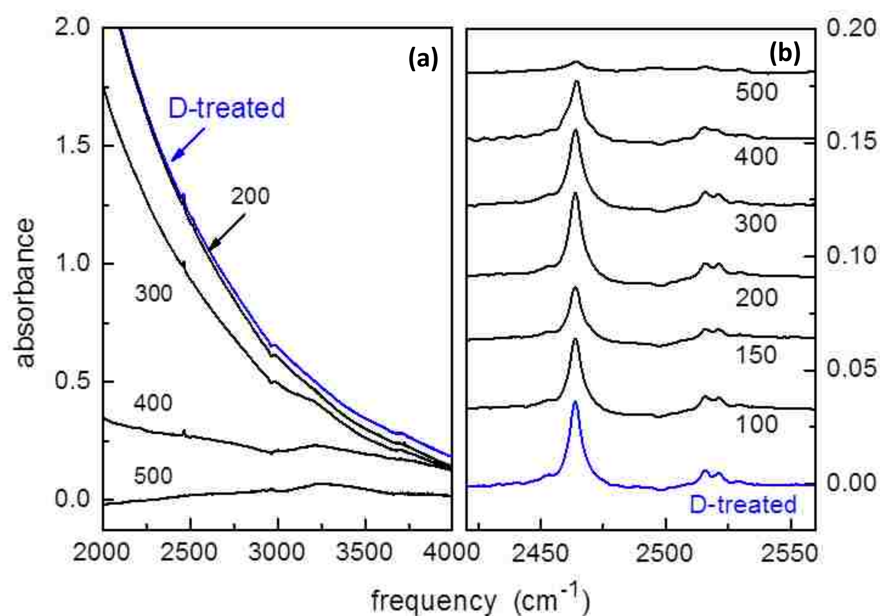

FIG. 3.3 A selection of IR absorption spectra (T = 77 K, resolution = 1 cm^{-1}) for an In_2O_3 sample that initially had been annealed (60 min) in flowing He at 850°C to remove any hydrogen that might have been present and was subsequently deuterated by an anneal (1 hour) in an D_2 ambient at 500°C. The sample was then annealed sequentially in a flowing He ambient at the temperatures shown in °C. (a) The absorption due to free carriers. (Free carrier absorption spectra measured following anneals from 50 to 250°C are indistinguishable from the results shown for the D-treated sample and also following the anneal at 200°C.) (b) The IR absorption lines in the O-D stretching region. These spectra were baseline corrected to remove the contribution from free carriers.

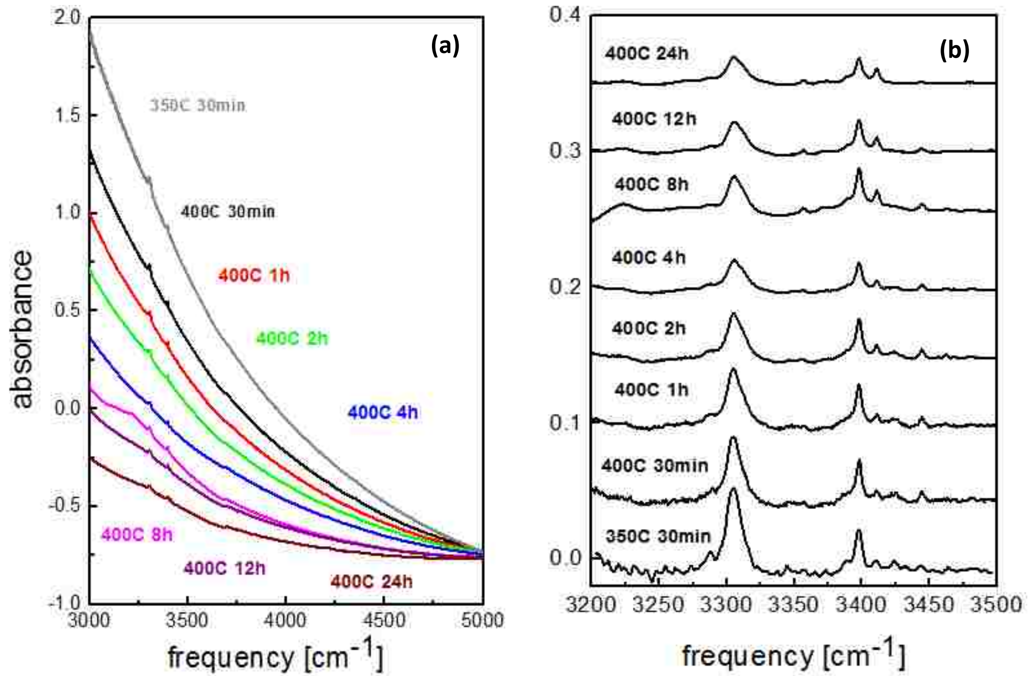

FIG. 3.4. A selection of IR absorption spectra (T = 77 K, resolution = 1 cm^{-1}) for a hydrogenated In_2O_3 sample that was annealed sequentially in flowing N_2 at 400°C for different accumulated times. (a) The absorption due to free carriers. (b) The IR absorption lines in the O-H stretching region.

The difference in the IR absorbances at 3500 cm^{-1} and 5000 cm^{-1} is used as a measure of the strength of the free carrier absorption and was determined for all absorbance spectra in Fig. 3.4(a). These differences are plotted as a function of accumulated annealing time in Fig. 3.5(a). The corresponding intensities (peak areas) of the 3306 cm^{-1} O-H line are plotted in Fig. 3.5(b). These two datasets were then fit by Excel Solver with the sum of two exponential functions. Fig. 3.5 produced with OriginLab software shows independent best fits to the data for the free carrier absorption and for the 3306 cm^{-1} O-H line intensity. The best fits to the combination of the free-carrier absorption data and the 3306 cm^{-1} O-H line intensity were then

determined by Excel Solver and plotted as Fig. 3.6, which shows that the same decay rates (higher decay rate and lower decay rate) can be used to fit both datasets. This series of experiments shows a strong correlation between the free carrier absorption and interstitial O-H line at 3306 cm^{-1}.

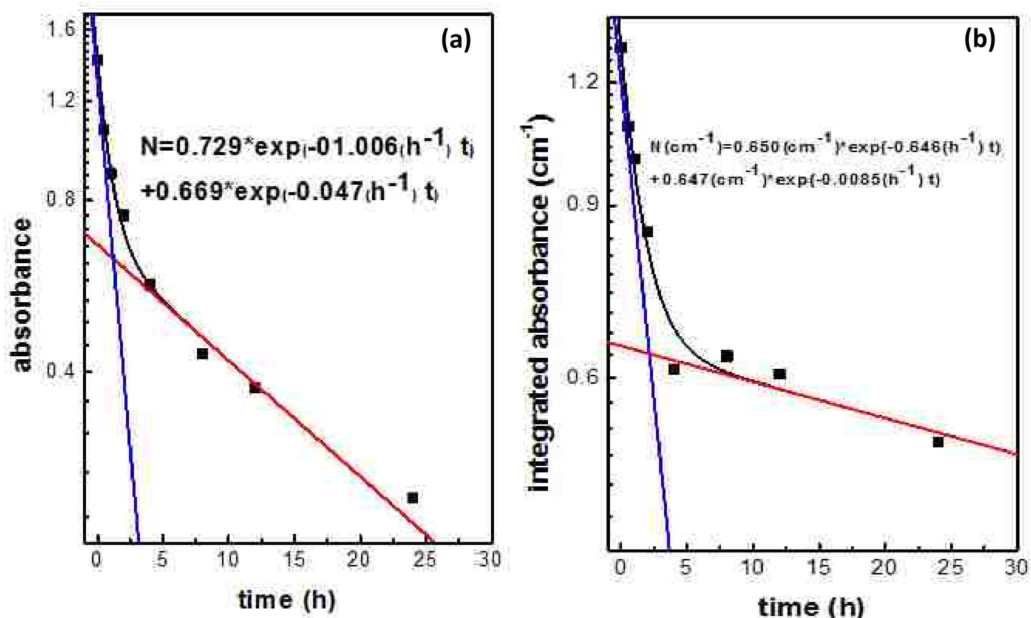

FIG. 3.5. The decay of free carrier absorption and the intensity of the interstitial O-H line at 3306 cm^{-1} for isothermal anneal experiments (400°C) plotted on a Log10 scale. (a) best fit to free carrier absorption; (b) best fit to the intensity of the interstitial O-H line at 3306 cm^{-1}. Both datasets were fit by Excel Solver and then plotted by OriginLab.

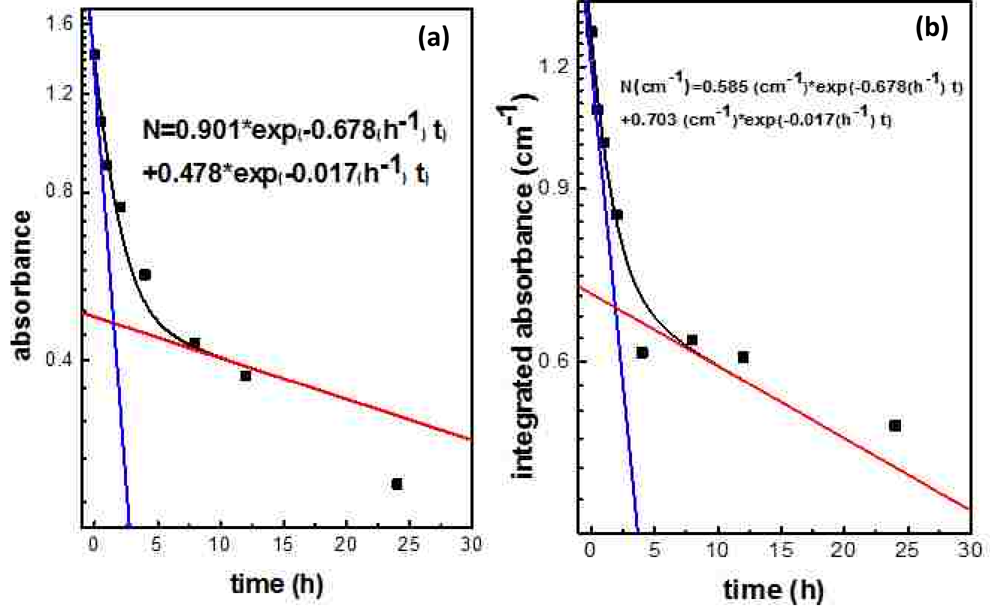

FIG. 3.6. Best fit to both the free carrier absorption (a) and the intensity of the interstitial O-H line at 3306 cm^{-1} (b) for isothermal annealing experiments (400°C). The same decay rates τ^{-1} (0.678 h^{-1} and 0.017 h^{-1}) are used for both datasets.

Fig. 3.7 shows the best fit to the combination of the free-carrier absorption and the area of the 3306 cm^{-1} O-H line on a linear scale. The fits were also produced with Excel Solver and plotted in OriginLab, which found the best decay rates to match our experimental data. The fit shown on a linear scale indicates a good match to both datasets.

The decay of the free carrier absorption and the intensity of the interstitial O-H line both showed the same decay rates. For the free carrier absorption, we find,

$$N = 0.901e^{-0.678(h^{-1})t} + 0.478e^{-0.017(h^{-1})t} \tag{3.1}$$

For the area of the interstitial O-H line, we find,

$$N(cm^{-1}) = 0.585(cm^{-1})e^{-0.678(h^{-1})t} + 0.703(cm^{-1})e^{-0.017(h^{-1})t} \tag{3.2}$$

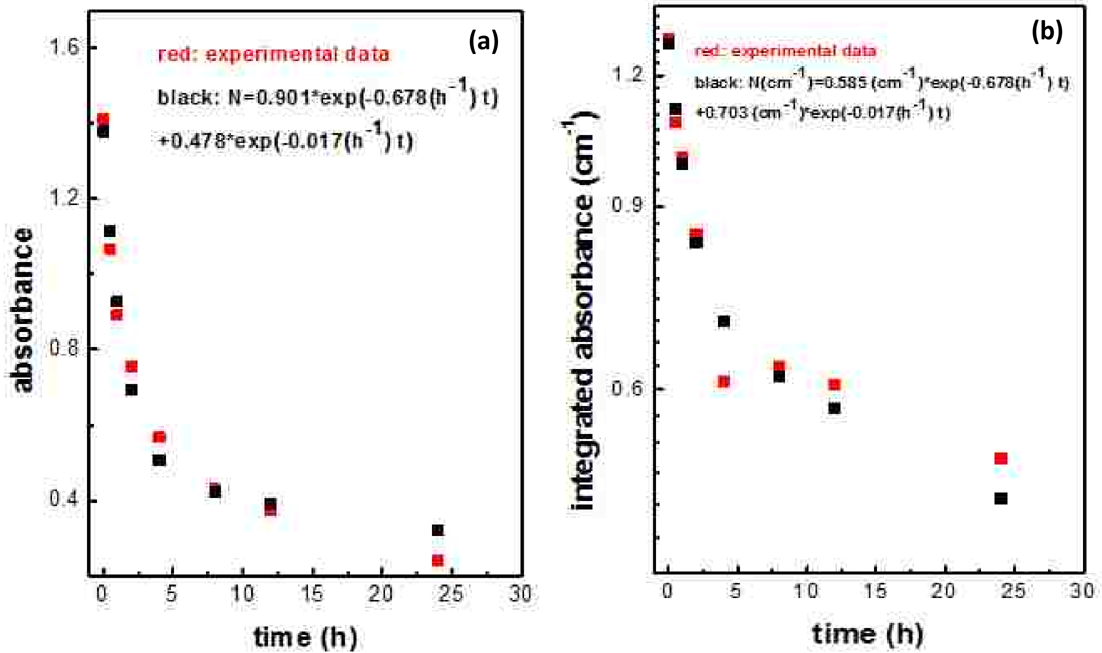

FIG. 3.7. Best fit to data for the free carrier absorption (a) and the peak height of the interstitial O-H line at 3306 cm^{-1} (b) for isothermal annealing experiments (400°C). Fits made with the same decay rates (-0.678 h^{-1} and -0.017 h^{-1}) are shown on a linear scale.

Experiments were performed to investigate how far H had penetrated into an In_2O_3 sample following a hydrogenation treatment in H_2. An as-grown sample was initially annealed at 1000°C for 30 min in flowing He to eliminate any H that might be present. There was no IR absorption observed that might be due to free carriers or O-H centers following this treatment [see the bottom spectra in Figs. 3.8(a) and 3.8(b) labeled H-free]. This sample was then annealed in an H_2 ambient at 450°C for 30 min.

Layers were then successively removed from the sample surfaces by lapping and

polishing. The sample thickness was measured with a micrometer as the sample was thinned. IR spectra [Figs. 3.8(a) and 3.8(b)] were measured as layers were removed to monitor both the free-carrier and O-H vibrational absorption. The total thickness removed from the two surfaces after each thinning step is indicated in Fig. 3.8 in units mm.

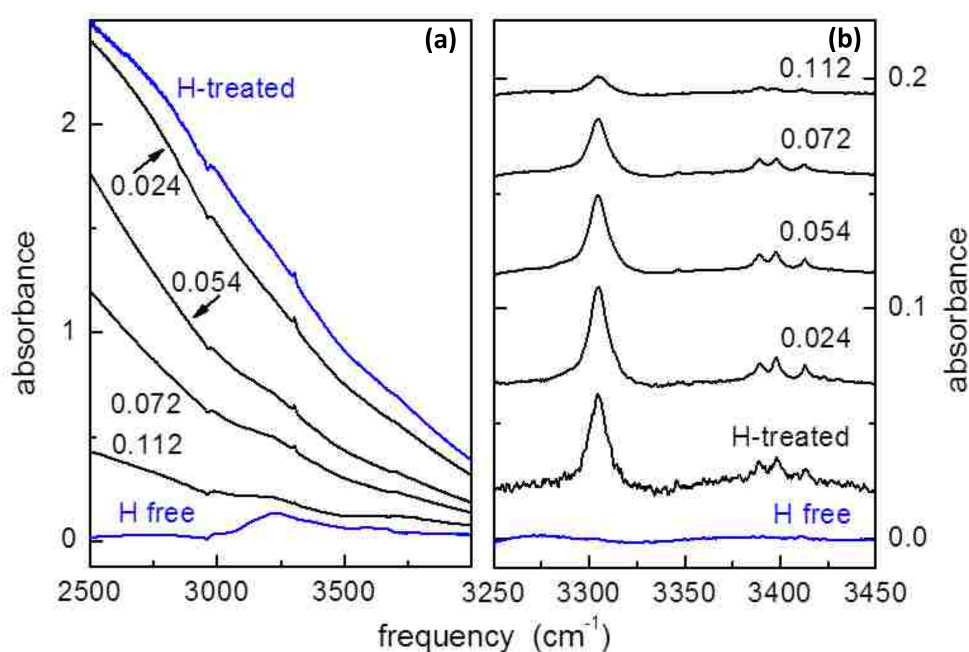

FIG. 3.8. A selection of IR absorption spectra (T = 77 K, resolution = 1 cm^{-1}) for an In_2O_3 sample that initially had been annealed (30 min) in flowing He at 1000°C to remove any hydrogen that might have been present and was subsequently hydrogenated by an anneal (1 hour) in an H_2 ambient at 450°C. The sample was then sequentially thinned by lapping and polishing the front and back surfaces. The thickness removed following each thinning step (both sides) is shown in mm. (a) shows free-carrier absorption spectra for the H-treated sample and for the sample following thinning. (b) shows baseline-corrected IR spectra of the O-H absorption lines.

The decrease in both the free-carrier absorption and the area of the 3306 cm^{-1} line intensities are plotted together in Fig. 3.9. The free-carrier absorption and the 3306 cm^{-1} O-H line are removed together as the sample is thinned. The hydrogenated layer is removed from the near-surface region of the sample when 0.06 mm is lapped from the surface of the In_2O_3 sample. These experiments show that both the free carriers and OH centers arise from a thin layer near the sample surface, further supporting the assignment of the 3306 cm^{-1} O-H line to an interstitial H^+ shallow donor that gives rise to the free-carrier absorption seen for H treated samples.

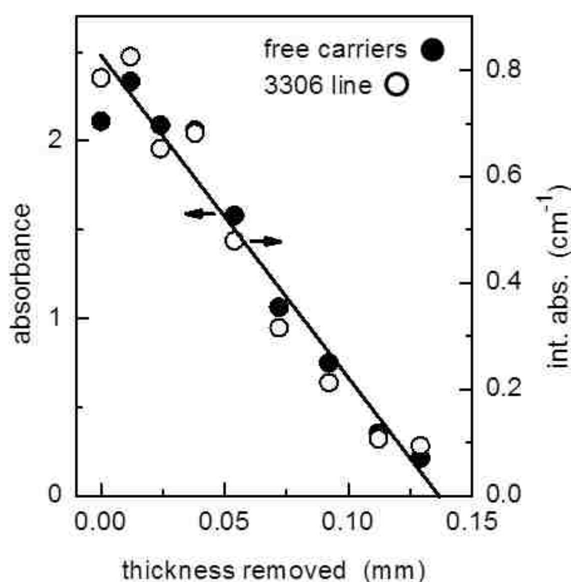

FIG. 3.9. Strength of free-carrier absorption and O-H vibrational absorption for the In_2O_3 sample whose IR data are shown in Fig. 3.8 as a function of thickness removed from the sample. The left scale (filled circles) shows the difference in the free-carrier absorption at 2500 and 4000 cm^{-1} for each thickness removed. The right scale (open circles) shows the integrated absorbance for the 3306 cm^{-1} O-H stretching line assigned to the interstitial H^+ shallow donor for each thickness removed.

3.3.3: Calibration of IR lines

Infrared absorption and Hall effect measurements were performed for the same deuterated In_2O_3 sample to approximately calibrate the strengths of the 3306 and 2464 cm^{-1} vibrational absorption lines assigned to shallow donor centers. An In_2O_3 sample was annealed (60 min) in a D_2 ambient at 450°C to produce OD shallow donors. IR absorption measurements were made to determine the integrated areas of the O-D and O-H lines at 2464 and 3306 cm^{-1}. Hall effect measurements performed by collaborators at the University of Florida yielded a sheet carrier concentration of 1.6 x 10^{17} cm^{-2} for this D-treated sample. Following the Hall measurements, this sample was thinned in steps to remove the O-H and O-D line absorption and also the free carrier absorption, similar to the results shown in Fig. 3.8, to determine the thickness of the doped layer. The total thickness of the doped layer (sum of front and back surfaces) was found to be 0.10 mm. The local carrier concentration in a doped layer is, therefore, ~1.6 x 10^{19} cm^{-3}.

$$n_{layer} = \frac{n_s}{d_{layer}} = \frac{1.6 \times 10^{17} cm^{-2}}{0.01 cm} = 1.6 \times 10^{19} cm^{-3} \qquad (3.3)$$

(This result is not the upper limit for the free-carrier density that can be produced by hydrogenation. Treating samples at higher temperatures or for longer times produced substantially stronger free-carrier absorption that made the samples opaque.)

The concentration N of defects (cm^{-3}) is proportional to the integrated absorption coefficient for the corresponding vibrational absorption line and is given by [3.22],

$$N = (m\, \eta\, c^2 / \pi\, q_{eff}^2) \int \alpha \, d\sigma \qquad (3.4)$$

Here, m is the mass of the oscillating impurity, H or D; η is the refractive index [taken to be η = 2.0 for In_2O_3 (refs. 1 and 11)]; α is the absorption coefficient; σ is the frequency in wavenumbers; and q_{eff} is an effective oscillating charge, given in terms of the electron charge in esu. [Eq. (3.4) is written in CGS units to be consistent with the absorption coefficient, conventionally expressed in units of cm^{-1}, and the frequency in wavenumber units, also cm^{-1}.]

The oscillating effective charge for our experiments is then given by,

$$q_{eff}{}^2 = \frac{m_p \eta c^2}{\pi e^2 (N_{OH} + N_{OD})} \left(\int \alpha_{OH} d\sigma + 2 \int \alpha_{OD} d\sigma \right) \tag{3.5}$$

Here, N_{OH} and N_{OD} are the concentrations of H and D defects, the sum of which is n_{layer} given in Eq. (3.3). α_{OH} and α_{OD} are the corresponding absorption coefficients. The integrated absorption coefficient $\int \alpha d\sigma$ is related to the integrated absorbance (IA) by the relationship,

$$\int \alpha d\sigma = \frac{2.303 \times IA}{d} \tag{3.6}$$

In this equation, IA has units cm^{-1} and the deuterated layer thickness d has units cm, yielding the quantity $\int \alpha d\sigma$ in units cm^{-2}. IR absorption line areas were determined with Peakfit software by fitting with Lorentzian or Gaussian line shapes to determine peak areas. Fits to our spectra gave $\int \alpha_{OH} d\sigma$ =68.9 cm^{-2} for the 3306 cm^{-1} O-H line and $\int \alpha_{OD} d\sigma$ =94.8 cm^{-2} for the 2464 cm^{-1} O-D line. These results yield an effective charge of q_{eff} = 0.26 e for the 3306 and 2464 cm^{-1} vibrational absorption lines assigned to the interstitial hydrogen and deuterium shallow donors in In_2O_3. This result for q_{eff} is similar to that found previously for the O-H line at 3611 cm^{-1} in ZnO,

whose effective charge is 0.28 e [3.23].

We have Hall and infrared data for a second In_2O_3 sample treated with D_2. In this case, we have not made a measurement of the deuterated layer thickness. However, if we assume a layer thickness of 0.05 mm similar to that of the sample discussed above (since they were both annealed in a D_2 ambient at 450°C for 60 min), we can make a rough calculation of the oscillating effective charge as a cross-check of our results. In this case, fits to our IR spectra give $\int \alpha_{OH} d\sigma$ =35.6 cm^{-2} and $\int \alpha_{OD} d\sigma$ =180.8 cm^{-2}. The sheet carrier concentration was found by Hall measurements to be 1.3×10^{17} cm^{-2}. These results yield an oscillating effective charge of q_{eff}= 0.34 e. This rough value is approximately equal to the result given in the paragraph above and provides a cross-check of our calibration.

3.3.4: Hydrogen diffusion in In_2O_3 crystals

Hydrogen diffusion into In_2O_3 crystals can be treated as one of the cases in semiconductor diffusion, which is due to Fick's second law:

$$\frac{\partial C}{\partial t} = D\frac{\partial^2 C}{\partial x^2} \tag{3.7}$$

Here, C is the concentration, t is time, x is the diffusion depth, and D is the diffusion coefficient.

Constant Surface Concentration

Experimentally, this corresponds to the common case of plating a thin film of the diffusant on to the flat face of a semiconductor slice with a constant surface

concentration. The film then becomes the diffusion source. The initial condition at t=0 is

$$C(x,0) = 0 \tag{3.8}$$

The boundary conditions are

$$C(0,t) = C_s \tag{3.9}$$

and

$$C(\infty,t) = 0 \tag{3.10}$$

where C_s is the surface concentration (at x=0), which is independent of time.

The solution of Fick's diffusion equation that satisfies the initial and boundary conditions is given by a complementary error function,

$$C = C_s \operatorname{erfc} \frac{x}{2(Dt)^{1/2}} \tag{3.11}$$

Constant Total Dopant

For this case, a fixed amount of dopant is deposited onto the semiconductor surface in a thin layer, and the dopant subsequently diffuses into the semiconductor. The initial condition is the same as Eq. (3.8). The boundary conditions are

$$\int_0^\infty C(x,t) = S \tag{3.12}$$

and

$$C(\infty,t) = 0 \tag{3.13}$$

The solution of the diffusion equation that satisfies the above conditions is

$$C(x,t)=\frac{S}{\sqrt{\pi Dt}}\exp\left(-\frac{x^2}{4Dt}\right) \quad (3.14)$$

As for our doping procedures, In_2O_3 samples were placed in sealed quartz ampoules filled with H_2 or D_2 gas, which corresponds to a constant surface concentration case with a complementary error function.

Considering the previous thinning experiments with hydrogen in-diffusion, the diffusion depth x shown in Eq. (3.11) is just half of the thickness removed for each step. Also, based on Eq. (3.6), the absorption coefficient $\int \alpha d\sigma$ can be calculated for each layer thickness removed. In this case, for each layer removed,

$$\int \alpha_{OH} d\sigma = -\frac{2.303(IA_{x_n} - IA_{x_{n-1}})}{x_n - x_{n-1}} \quad (3.15)$$

where IA_{xn} and IA_{xn-1} are the integrated absorbance of hydrogen within the rest of the sample when sample thicknesses x_n and x_{n-1} have been removed. Then, based on Eq. (3.4), the hydrogen defect concentration can be solved for each sample surface layer removed by taking q_{eff}= 0.28 e, which was discussed in section 3.3.3.

Therefore, the thinning experimental data show the hydrogen concentration as a function of diffusion depth after annealing the sample in H_2 at 450°C for one hour [Fig. 3.10]. This dataset has been fit by a complementary error function [Fig. 3.10] in Excel Solver and plotted by OriginLab software. The average hydrogen concentration has also been obtained to be about 2.2×10^{18} cm^{-3} by calculating Eq. (3.15) in terms of the

whole defect layer thickness. The diffusion coefficient D was found to be about 5× 10^{-9} cm^2/s at 450°C.

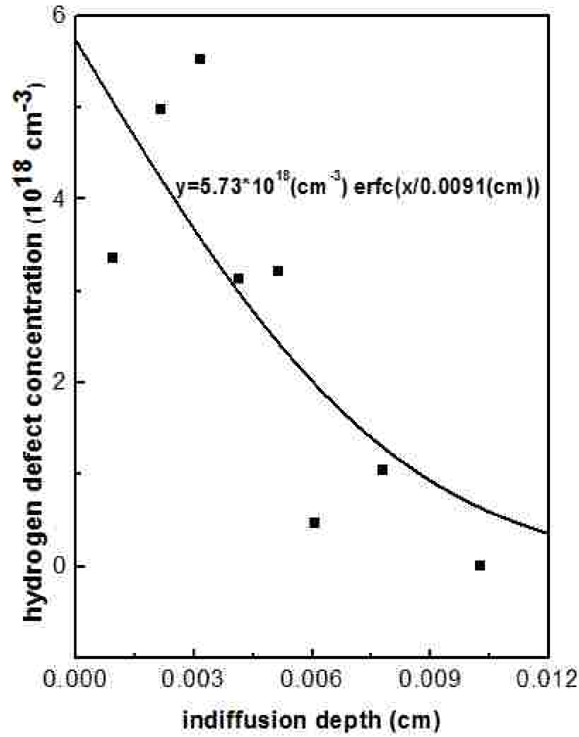

FIG. 3.10. The hydrogen defect concentration for an In_2O_3 sample (annealed in H_2 at 450°C for 1 hour) as a function of diffusion depth (layer thickness removed from one side). The experimental data were fit with a complementary error function.

We developed an alternative method to probe the diffusion of H. Two exponential decay rates were found for the annealing data shown in Figs. 3.5, 3.6 and 3.7. One possible explanation for two decay rates would concern the interconversion between different hydrogen defects. In this case, the higher decay rate might be from the decay of interstitial hydrogen with its IR line at 3306 cm^{-1}. The lower decay rate might be from an electrically inactive hydrogen species (H_2 or other inactive hydrogen centers) which could be converted into the interstitial hydrogen center at 3306 cm^{-1} by thermal

treatment at 400°C.

However, we favor an alternative explanation that involves the out-diffusion of H (or D) from the In_2O_3 samples. The out-diffusion of a defect from a finite slab of material obeys the approximate relationship,

$$\overline{C} / C_0 = \frac{8}{\pi^2} e^{-t/\tau} \tag{3.16}$$

where $\overline{C}$ is the average concentration in the slab, C_0 is the initial concentration and $\tau \equiv \frac{l^2}{\pi^2 D}$ is the relaxation time. Here l is the thickness of the slab and D is the diffusivity of the defect.

Our hydrogenated samples have two characteristic thicknesses. There is the thickness of the in-diffused layer and there is the thickness of the sample itself. Out-diffusion of H from the thin hydrogenated layer has a smaller time constant and therefore a faster rate. After several decay times, H becomes spread out through the entire sample thickness. Now, H out-diffusion from the entire sample occurs with a time constant characteristic of the sample thickness. In our experiments, the hydrogenated layer is typically 0.05 mm thick and the In_2O_3 samples are typically 0.5 mm thick. The out-diffusion time constant is proportional to the square of the layer thickness, so the out-diffusion rates should differ by a factor of 100, consistent with our experimental results for the slow and fast decay rates of the 3306 cm^{-1} line.

The thinning experiments (Figs. 3.8 and 3.9) provide data for the hydrogen in-diffusion case, while the isothermal annealing experiments (Figs. 3.5, 3.6, 3.7) provide data for the out-diffusion of hydrogen. Fig. 3.5(b) showed the best fit curve to

the absorbance of hydrogen with higher decay rate 0.646/h (due to the thin hydrogenated layer diffusion) and lower decay rate 0.0085/h (due to bulk diffusion). The out-diffusion from a slab shows the following decay rate and its dependence on the diffusion coefficient D:

$$D = \frac{l^2}{\pi^2}\tau^{-1} \tag{3.17}$$

l is the diffusion depth and τ^{-1} is the decay rate. The higher decay rate 0.646/h at 400°C with diffusion depth (layer thickness) l=0.006 cm, yielded $D_1=6.54\times10^{-10}$ cm^2/s. The lower decay rate 0.0085/h at 400°C with diffusion depth (sample bulk thickness) l=0.05 cm, yielded $D_2=5.98\times10^{-10}$ cm^2/s. Therefore, D_1 agreed with D_2 in layer out-diffusion and bulk out-diffusion at 400°C. Also, D_1 and D_2 are both smaller than D (5×10^{-9} cm^2/s) at 450°C found from our thinning experimental results, which is consistent with diffusion being faster at higher temperature.

The method outlined above is an approximate attempt to relate the diffusion coefficient D to the higher and lower rates of the out-diffusion vs. time curve. We can also numerically solve the diffusion equation [Eq. (3.7)] and integrate this solution over the diffusion depth x to generate the time dependence of hydrogen out-diffusion. This numerical method was performed by Mathematica programming, which solved the diffusion coefficient D for both the O-H line at 3306 cm^{-1} and the free carriers (Fig. 3.11). The detailed Mathematica codes are listed in appendices.

The strategy of the Mathematica program is to solve the diffusion equation, Fick's Second law, for the time evolution of the hydrogen concentration vs. depth during annealing at a fixed temperature. The initial condition for the diffusion problem is the complementary-error-function concentration profile that is produced by a hydrogen indiffusion treatment performed in an H_2 ambient. This error-function profile then evolves as the sample is annealed in N_2, with H in the near surface layer diffusing both out of the sample and into the bulk. The calculated concentration profile is then integrated over depth for each annealing time to simulate the magnitudes of the IR signals for both the intensity of the 3306 cm^{-1} O-H line and the concentration of free carriers. The shape of the plot of concentration vs. annealing time calculated by the Mathematica program matches the quantitative shape of our experimental data, Figs 3.5 to 3.7. We determined the value of the diffusion coefficient in the Mathematica code that produced the best least-squares fit to our experimental data.

The diffusion coefficient of hydrogen D(OH) was determined to be 7.22×10^{-10} cm^2/s for our out-diffusion experiments, which showed agreement with D_1 (6.54×10^{-10} cm^2/s) and D_2 (5.98×10^{-10} cm^2/s) by the two decay rates method. Furthermore, D(OH) and D(fc) by numerical method differed by just a factor of 3, which indicated a close relationship. Therefore, it seems reasonable to relate the out-diffusion coefficient D to the higher and lower rates of hydrogen intensity vs. time curve in the isothermal annealing data. This possible relationship will be investigated further in future research of the diffusion of H in In_2O_3.

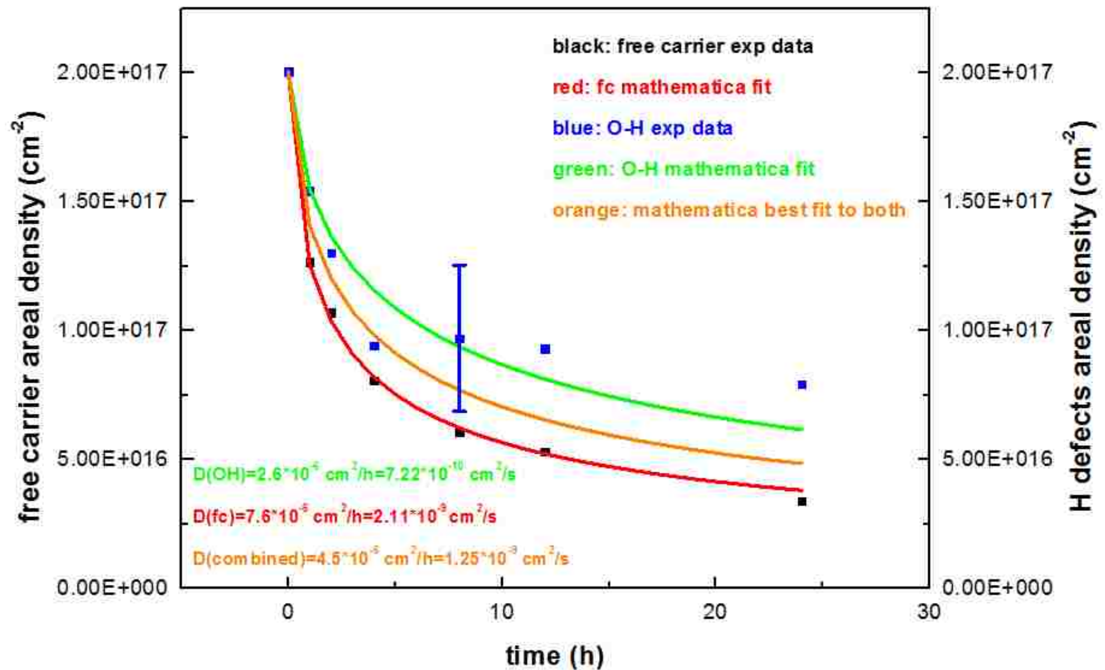

FIG. 3.11. The out-diffusion coefficient D determined by integrating the numerical solution to generate the time dependence of hydrogen (normalized) and free carrier out-diffusion. The O-H (blue) and free carrier (black) out-diffusion experimental data points were fit by Mathematica simulation curves (green and red) separately. A representative error bar is shown in the O-H experimental data that is due to uncertainty in the choice of baseline in the spectra. The orange curve is the best numerical integration fit to both two experimental datasets.

3.3.5: H_O shallow donors?

Most of the conductivity changes produced by the introduction of H (or D) into In_2O_3 in our experiments can be explained by an interstitial H^+ (or D^+) center that acts as a shallow donor. However, there is some experimental evidence for “hidden hydrogen” that does not give rise to O-H vibrational absorption but that remains electrically active, nonetheless. The data in Fig. 3.1 show that for a hydrogenated

sample annealed at 100°C, the free-carrier absorption remained unchanged while the 3306 cm^{-1} O-H line was decreased in intensity by ~40%. Annealing at higher temperatures caused the intensity of the O-H absorption to recover. This result suggests that interstitial H^+ can be partially converted by annealing near 100°C into an electrically active H center that gives no observable O-H vibrational absorption. The shallow donor center with H trapped at an oxygen vacancy (H_O^+) predicted by theory [3.12] is a candidate for such a defect. The vibrational absorption arising from the H_O^+ center is expected to lie at a frequency too low to be observed by IR transmission measurements [3.7][3.24], as predicted by theory to be discussed below (Table 3.3). (Figure 3.3 shows a similar result for an In_2O_3 sample containing D when it was annealed near 150°C. The O-D line intensity is decreased by ~40% while the free-carrier absorption remains unchanged, suggesting conversions between interstitial D^+ and D_O^+ shallow donors.).

Interstitial H^+ and H_O^+ shallow donor centers have been found to coexist in other oxides, ZnO and SnO_2, for example [3.23][3.25]. In these cases, H_O^+ is more thermally stable than interstitial H^+ and is the dominant donor in the material. Our results for In_2O_3 indicate that, in this case, it is interstitial H^+ that is the dominant H-related shallow donor.

3.3.6: Other IR absorption lines

A number of O-H and O-D absorption lines in addition to the lines at 3306 and 2464 cm^{-1} (Table 3.1) were seen in spectra measured for as-grown samples of In_2O_3

and for samples treated in H_2 or D_2 [3.26]. These lines might be due to metastable interstitial H configurations [3.12] or H associated with a native defect such as the In vacancy [3.27]. These additional vibrational lines appeared in different samples with different relative intensities, depending on the sample treatment with one exception. The O-D lines at 2469 and 2521 cm^{-1} (Fig. 3.12) were introduced together and were annealed away together (around 550°C) in our experiments. (Of the corresponding O-H lines at 3316 and 3398 cm^{-1}, only one is resolved, making these O-H lines difficult to study.)

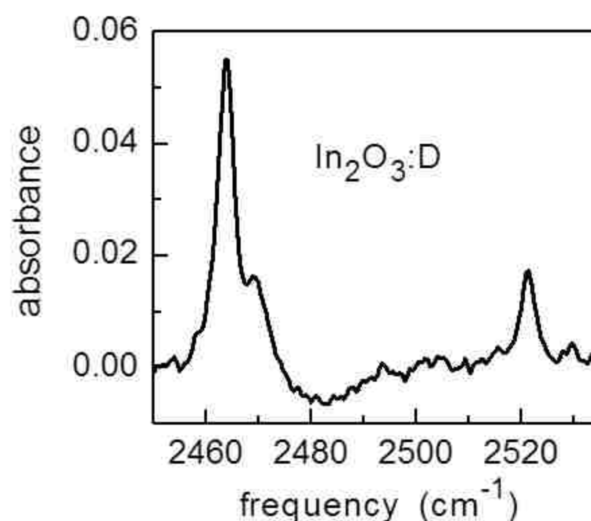

FIG. 3.12. IR absorption spectrum (T = 4.2 K, resolution = 1 cm^{-1}) for an In_2O_3 sample deuterated by an anneal (60 min) in a D_2 ambient at 500°C.

The correlation between the O-D lines at 2469 and 2521 cm^{-1} is confirmed by the results shown in Fig. 3.13 and Table 3.2. Fig. 3.13 shows that these two peaks were introduced together in all four deuterated samples (samples were deuterated and then annealed in flowing N_2 around 400°C to partially recover IR transparency). The intensities of the two peaks have been determined by fitting with Peakfit software.

Results are shown in Table 3.2. The ratios between the areas of O-D lines at 2469 and 2521 cm^{-1} are all near 1, showing a good correlation and strongly supporting the observation that these two lines are introduced and annealed away together.

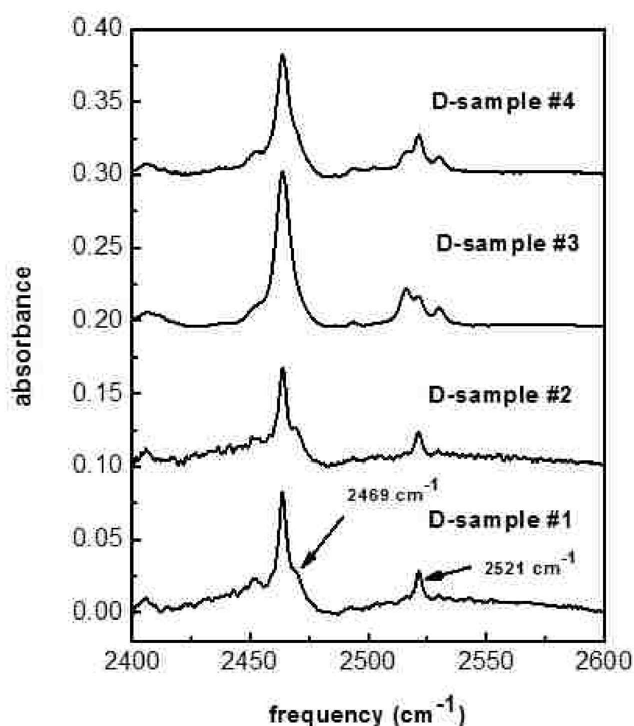

FIG. 3.13. IR absorption spectra in the O-D stretching region for four deuterated In_2O_3 samples, which then have been annealed in flowing N_2 to partially recover IR transparency. The O-D lines at 2469 (the shoulder) and 2521 cm^{-1} were introduced together into sample spectra.

Both H and D were introduced together into In_2O_3 samples to investigate whether or not defects containing more than one H (or D) atom could be produced. In spite of several attempts to diffuse H and D into In_2O_3 layers of similar thickness, no new absorption lines that might arise from centers containing both H and D were found [3.22]. Implications of this result are discussed in section 3.4.

Table 3.2. The intensities of O-D lines at 2464, 2469 (the shoulder) and 2521 cm^{-1} for four different deuterated In_2O_3 sample. The intensities of the 2521 cm^{-1} and 2469 cm^{-1} D lines are approximately equal.

D-treated sample	2464 cm^{-1} intensity (cm^{-1})	2469 cm^{-1} intensity (cm^{-1})	2521 cm^{-1} intensity (cm^{-1})	intensity ratio between 2469 cm^{-1} and 2521 cm^{-1}
#1	0.437	0.098	0.099	1.010
#2	0.357	0.068	0.064	0.941
#3	0.781	0.132	0.111	0.841
#4	0.377	0.159	0.163	1.025

3.3.7: In_2O_3 phonons

In_2O_3 samples that had been deliberately hydrogenated or deuterated by an anneal in H_2 or D_2 gas at 500°C were found to be opaque in the spectral region with frequency near 2000 cm^{-1} and below. However, following annealing treatments at temperatures near 400°C that reduced the free carrier concentration, an additional strong IR absorption line emerged at 1890 cm^{-1} as the sample increased in transparency [Fig. 3.14]. We found that this line showed no H vs D isotope effect.

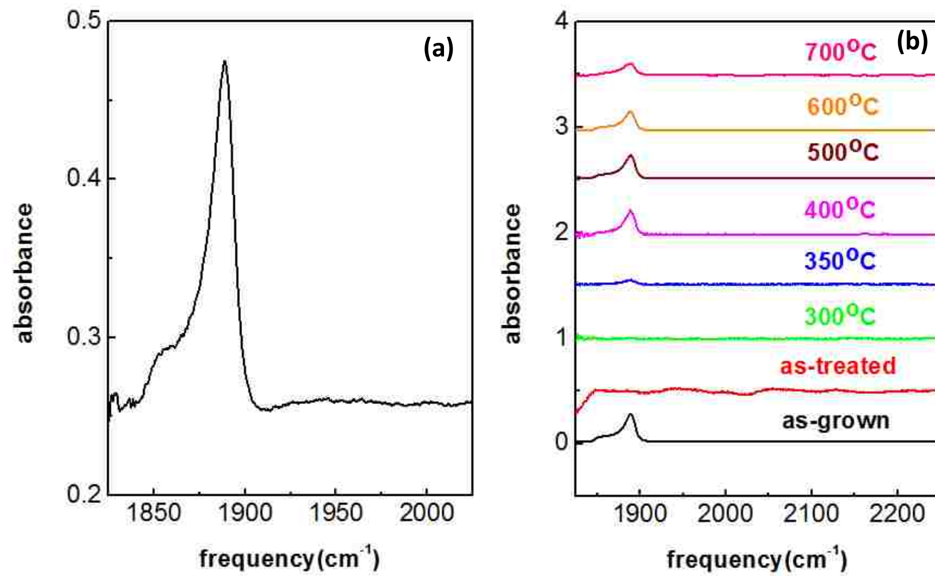

FIG. 3.14. A strong IR absorption line at 1890 cm^{-1} (a) existed in an as-grown In_2O_3 sample but disappeared after a sample had been deliberately hydrogenated or deuterated. This line emerged again as the sample turned more transparent upon annealing (b).

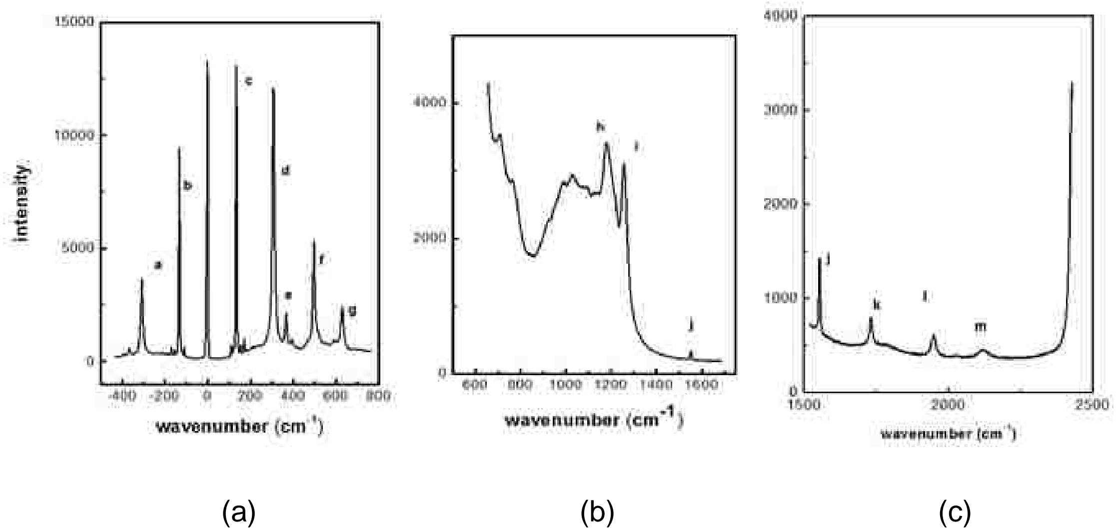

(a) (b) (c)

FIG. 3.15. Raman Spectra of an as-grown In_2O_3 sample. (a) shows the fundamental region. (b) and (c) show spectra for the overtone regions. Line frequencies and suggested assignments are presented in Table 3.3.

We attribute the 1890 cm^{-1} line to the third harmonic of an In_2O_3 lattice phonon with frequency 630 cm^{-1} that can be seen with Raman spectroscopy. If the 3rd harmonic of the 630 cm^{-1} phonon can be observed, it is natural to wonder if the 2nd harmonic might also be present. Another strong line at 1254 cm^{-1} was observed by Raman spectroscopy, which can be attributed to the second harmonic of the In_2O_3 lattice phonon at 630 cm^{-1} [Fig. 3.15(b)]. Table 3.3 shows frequencies of the lines seen in Raman measurements performed by Sandro Koch at the Dresden University of Technology. Assignments to the combination modes of different phonon frequencies are suggested in the Table.

Table 3.3. Frequencies of lattice vibrational lines seen with Raman measurements. Assignments of combination modes are suggested.

peak number	frequency (cm^{-1})	possible combination
c	133	c
d	306	d
e	366	e
f	495	f
g	627	g
h	1179	f+g+e+a
i	1254	g*2
j	1551	g*2+d
k	1731	f+g+d*2
i	1948	c*3+j
m	2119	b+d+l

3.3.8: Other shallow donors and deep compensating centers

While most of the samples we studied were pale yellow in color, a few as-grown samples had different colors. IR spectra are shown in Fig. 3.16 for an as-grown sample that was gray in color and for an as-grown sample that was green. In this case, several O-H absorption lines are seen along with substantial free-carrier absorption.

Annealing experiments [Fig. 3.16(a)] found that the free-carrier absorption in the gray-colored sample was thermally stable for an annealing temperature of 700°C where H centers and their associated O-H lines are annealed away. Fig. 3.16(a) also showed a relatively weaker free carrier absorption in an as-grown sample that was green in color. In this case, the free carrier absorption was stable around 800°C where associated O-H lines were annealed away. These annealing results indicate that these gray-colored and green-colored samples contain thermally stable shallow donors other than interstitial hydrogen. The weaker free carrier absorption in the green sample indicates a lower donor concentration than for the gray sample.

The as-grown In_2O_3 samples we studied, whether pale yellow in color or gray/green, showed weak absorption at 3306 cm^{-1} in addition to other O-H absorption lines, similar to the 3306 cm^{-1} line seen in Fig. 3.16. From the areas of the 3306 cm^{-1} line seen in typical as-grown samples and the calibration of this absorption given in Eq. (3.9), we estimate an interstitial hydrogen donor concentration between 2x10^{16} and 10^{17} cm^{-3} that is due to hydrogen that was introduced unintentionally into In_2O_3 samples during the growth process that was carried out in the air.

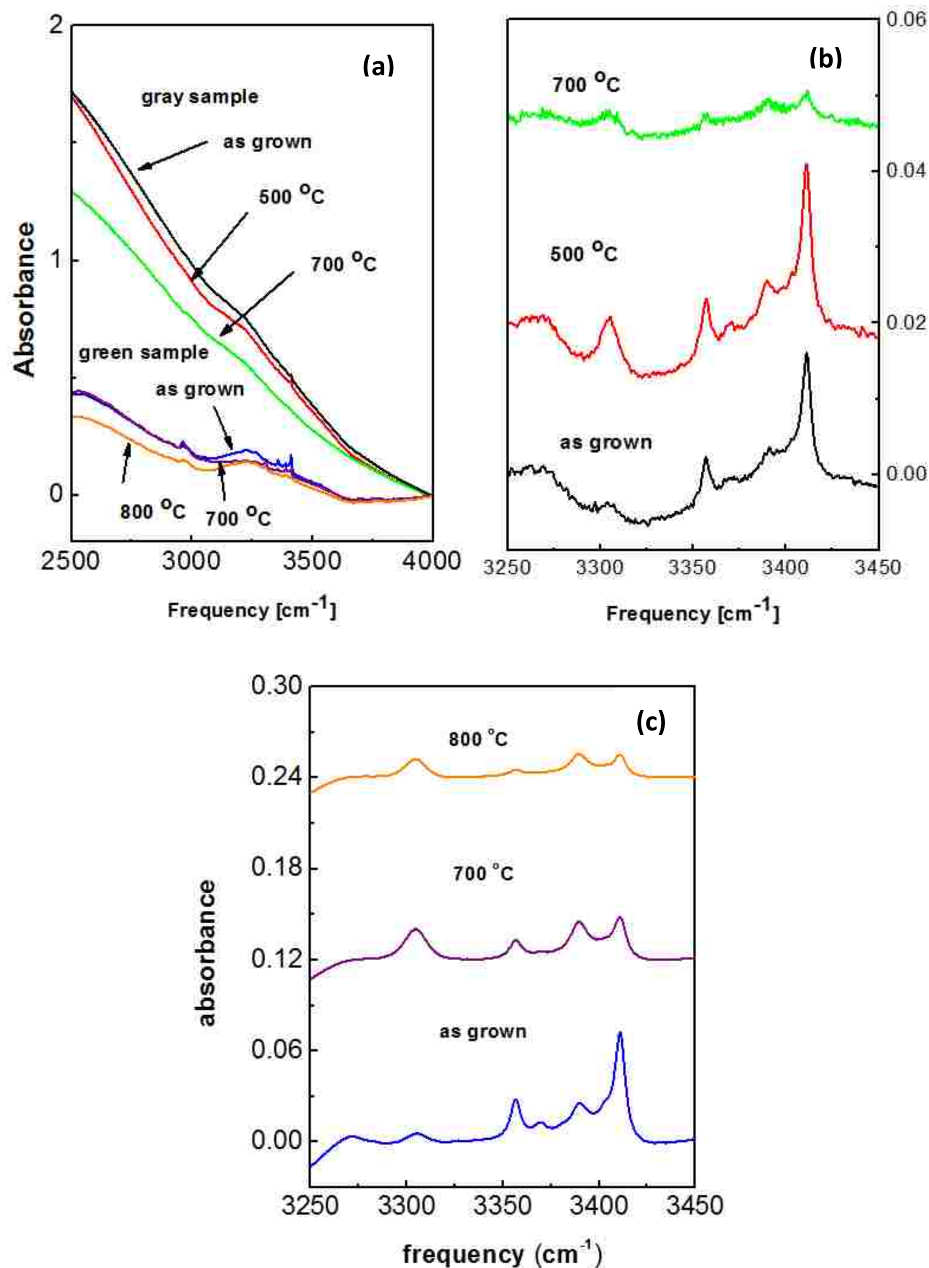

FIG. 3.16. IR spectra of colored as-grown samples (gray and green samples). The gray sample was 0.825 mm thick and the green sample 1.160 mm thick. Samples were annealed at the temperature shown. (a) free carrier absorbance of gray and green In_2O_3 samples. (b) IR absorption lines in the O-H stretching region for the grey sample. (c) IR absorption lines in the O-H stretching region for the green sample.

Samples that are pale yellow in color did not show substantial free-carrier absorption in our experiments, and similar samples, also grown at Oak Ridge, were found in another study to have high resistivity [3.19]. Our infrared results for the concentrations of H_i^+ shallow donors in as-grown In_2O_3 samples suggest that for such samples to have high resistivities, they must contain compensating defects - also at the ~10^{17} cm^{-3} level.

The concentrations of hydrogen (or deuterium) shallow donors introduced intentionally into thin layers by annealing in an H_2 (or D_2) ambient at 500°C in our experiments are near 10^{19} cm^{-3} and would dominate the n-type doping in these layers, even if these In_2O_3 samples contained compensating centers at the 10^{17} cm^{-3} level.

We attempted to produce free carriers in In_2O_3 samples by annealing in reducing ambients that did not include hydrogen. Annealing samples in flowing He at 800°C did not produce free-carrier absorption that is at all comparable to that shown in Figs. 3.1 and 3.3. Similarly, annealing In_2O_3 samples in a flowing CO ambient at 700°C for 2 hrs did not produce substantial free-carrier absorption.

3.4: Defect Modeling

Professor Fowler (Lehigh University) has carried out calculations of H defect structures in In_2O_3 with the CRYSTAL06 code [3.29] using density functional theory (DFT).

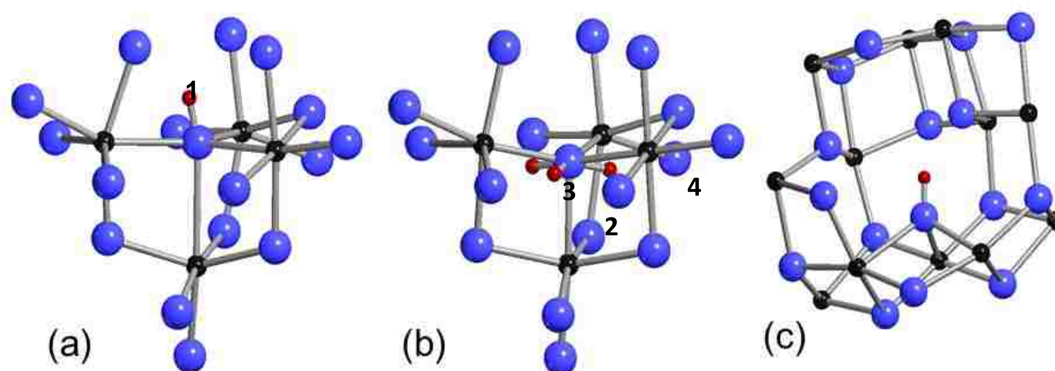

FIG. 3.17. Defect models. (a) The lowest energy antibonding configuration (AB_{01}) for H_i^+. (b) Metastable H_i^+ antibonding configurations (AB_{02} to AB_{04}). Defect labeling follows Ref. 12. (c) Lowest energy configuration for $[V_{In}(24d)\text{-}H]^{2-}$. Larger (blue) atoms represent O, smaller (black) atoms represent In, and the smallest (red) atom is H. This was constructed by MOLDRAW (P. Ugliengo, Torino 2006, available at http://www.moldraw.unito.it) and POV-Ray (http://povray.org).

Similar calculation have been reported previously in Ref. 12 and 27. Ref. 12 predicts that the four inequivalent BC configurations for H^+ are unstable. Of the four antibonding configurations, Fowler's results (Table 3.4) and those of Ref. 12 predict that the structure shown in Fig. 3.17(a) is lowest in energy, while the remaining three configurations shown in Fig. 3.17(b) are metastable. Thus the O-H (O-D) line at 3306 (2464) cm^{-1} is assigned to the lowest energy antibonding configuration shown in Fig. 3.17(a).

Fowler's calculations agree with those of Ref. 12 in predicting that H_i^+ is energetically favored over H^+ substituted for a neutral oxygen, while given an H^+ and

an existing O vacancy, the substitutional configuration is favored over a separated H_i^+ and an O vacancy. These results are in agreement with our experimental results that show that H_i^+ is the dominant H-related shallow donor in In_2O_3. Furthermore, our results also suggest that H_O^+ may coexist with H_i^+ following annealing treatments near 100°C. Except in this brief annealing window between 100 to 200°C, H_i^+ can explain the free-carrier absorption we have observed as well as the shallow donors from which it arises without the need for invoking additional shallow H centers. This is different from the situation for H in ZnO and SnO_2 where H_O^+ has been found to be the more thermally stable H-containing shallow center and H_i^+ is only marginally stable at room temperature.

There are several lines in the O-H and O-D spectra in addition to the 3306 and 2464 cm^{-1} lines attributed to the lowest energy interstitial H and D centers. Candidates for these additional lines include the metastable antibonding configurations for H_i^+ shown in Fig. 3.15(b), centers with H in V_{In} [3.27], and hydrogen defects that contain more than one H atom.

The metastable AB configurations have predicted vibrational frequencies that are substantially higher than the 3306 cm^{-1} line (Table 3.4) and are, therefore, candidates for the H lines observed between 3375 and 3425 cm^{-1}. These configurations, however, are at least 0.5 eV higher in energy than the stable configuration, so it is not clear that they will be populated.

Table 3.4. Calculated vibrational frequencies and formation energies relative to the most stable configurations for H centers in In_2O_3. Defect labeling follows that of Refs. 12 and 27. Frequencies for H_i and V_{In}-H centers include the effect of anharmonicity. The results shown for H_O and D_O are harmonic frequencies.

Defect	Energy (eV)	ω_H (cm^{-1})	ω_D(cm^{-1})
$H_i^+(AB_{01})$	0	2931	2193
$H_i^+(AB_{02})$	0.51	3125	2325
$H_i^+(AB_{03})$	0.82	3283	2449
$H_i^+(AB_{04})$	0.82	3453	2555
$[V_{In}(24d)\text{-}H]^{-2}$ (eq:S)	0	3026	2253
$[V_{In}(24d)\text{-}H]^{-2}$ (ax)	0.56	3340	2473
$[V_{In}(24d)\text{-}H]^{-2}$ (eq:L)	0.58	3313	2453
$[V_{In}(8b)\text{-}H]^{-2}$		3434	2540
H_O		800	566
$[V_{In}(24d)\text{-}2H]^{-1}$		range from 3150 to 3525	range from 2225 to 2500

There are two inequivalent In sites, In(1) and In(2), or 8b and 24d, respectively, in Wyckoff notation. One of the 24d sites for H in an In vacancy (24d eq:S in the notation of Ref. 27) has the lowest energy and also has the lowest predicted vibrational frequency of the three possible sites. Ref. 27 predicts this frequency to be 13 cm^{-1} higher than that of H_i^+, while Fowler predicts it to be 90 cm^{-1} higher (Table 3.4). This defect is a candidate for one of the vibrational lines seen between 3225 and 3290 cm^{-1}.

Other, metastable V_{In}-H configurations have predicted vibrational frequencies approximately 200 cm^{-1} higher than H_i^+ and are also candidates for the vibrational lines observed between 3375 and 3425 cm^{-1}. Again, the circumstances in which these metastable sites are populated are not clear.

We also consider configurations with more than one H or D atom. The vibrational lines at 2469 and 2521 cm^{-1} are seen together in the spectra that we have measured for different deuterium-introduction treatments and following annealing treatments. These results suggest that both lines arise from the same D-containing center. If this were the case, one might expect the lines to shift if one of the D is replaced by an H. This, however, has not been observed in experiments on mixed H-D samples.

To consider this further, Professor Fowler has carried out calculations for two H in an In vacancy. There are three pairs of equivalent sites at the In(2) vacancy. Fowler finds that if the two H are attached to an equivalent pair, even though the coupling is weak, the degeneracy of these sites predicts that lines for H-D will be displaced by ~ 10 to 15 cm^{-1} from those predicted for H-H or D-D. However, this is not seen experimentally. If the two H are attached to an inequivalent pair, the new lines predicted for H-D will be displaced from the H-H or D-D lines by less than 1 cm^{-1}, i.e., by a value too small to be resolved. And, the lowest-energy situation predicted by Fowler does involve hydrogens on *inequivalent* sites. Therefore, the possibility of two (or more) H in an In vacancy remains as a possibility. But alternatively, one line of the

pair of lines could be an O-D stretching mode and the second could be due to the 2nd harmonic mode of an O-D wag mode associated with the same defect and with an intensity that is strengthened by Fermi resonance [3.22].

3.5: Conclusions

The effect that hydrogen impurities have on the conductivity of In_2O_3 single crystals has been studied by IR spectroscopy and theory. Annealing In_2O_3 crystals in an H_2 or D_2 ambient at temperatures near 500°C was found to produce a thin conducting layer near the sample surface with a thickness ≈ 0.06 mm and with a carrier concentration determined by Hall measurements to be 1.6 x 10^{19} cm^{-3}. An OH vibrational line at 3306 cm^{-1} has been assigned to the interstitial H shallow-donor center that is responsible for the hydrogen-related conductivity. The corresponding D_i center has an OD line at 2464 cm^{-1}. The H_i center was found to be thermally stable up to ≈ 500°C.

Several additional OH lines were produced by the treatment of In_2O_3 in H. Additional configurations for interstitial H with higher formation energies or defects with H trapped by In vacancies that have been investigated by theory are candidates for these OH lines. A comparison of experiment with the relative vibrational frequencies for these H-containing defects predicted by theory (Ref. 27 and Table 3.2) suggests specific assignments.

Investigations of hydrogen shallow-donor centers in other conducting oxides studied recently, ZnO and SnO_2 for example[3.23] [3.25], find that H_i is only marginally stable at room temperature and that H_O is a more thermally stable donor that dominates the n-type conductivity of hydrogenated samples of these materials stored for substantial times at room temperature. Our experimental results and complementary theory show that the conductivity produced by the thermal treatment of In_2O_3 in hydrogen can be explained primarily by a thermally stable H_i center, consistent with theoretical predictions that H_O has a higher formation energy.

References

3.1. H.L. Hartnagel, A. L. Dawar, A. K. Jain, C. Jagadish, *Semiconducting Transparent Thin Films* (Institute of Physics, London, 1995).

3.2. A. Facchetti and T. Marks (eds.), *Transparent Electronics: From Synthesis to Applications* (Wiley, New York, 2010).

3.3. See the special issue of the Journal of Physics: Condensed Matter, Semiconducting Oxides, edited by R. Catlow and A. Walsh, J. Phys. Condens. Matter **23**, 330301 (2011).

3.4. *Oxide Semiconductors*, edited by B.G. Svensson, S.J. Pearton, and C. Jagadish (Academic Press, San Diego, 2013).

3.5. C.G. Van de Walle, Phys. Rev. Lett. **85**, 1012 (2000).

3.6. Ç. Kiliç and A. Zunger, Appl. Phys. Lett. **81**, 73 (2002).

3.7. A. Janotti and C.G. Van de Walle, Nature Materials **6**, 44 (2006).

3.8. P.D.C. King and T.D. Veal, J. Phys. Condens. Matter **23**, 334214 (2011).

3.9. M.D. McCluskey, M. C. Tarun, and S. T. Teklemichael, J. Mater. Res. **17**, 2190 (2012).

3.10. H. Li and J. Robertson, J. Appl. Phys. **115**, 203708 (2014).

3.11. I. Hamberg and C. G. Granqvist, J. Appl. Phys. **60**, R123 (1986).

3.12. S. Limpijumnong, P. Reunchan, A. Janotti, and C. G. Van de Walle, Phys. Rev. B **80**, 193202 (2009).

3.13. S. Lee and D. C. Paine, Appl. Phys. Lett. **102**, 052101 (2013).

3.14. J. H. W. De Wit, J. Sol. State Chem. **13**, 192 (1975).

3.15. J. H. W. De Wit, G. Van Unen, and M. Lahey, J. Phys. Chem. Solids **38**, 819 (1977).

3.16. P.D.C. King, R.L. Lichti, Y.G. Celebi, J.M. Gil, R.C. Vilão, H.V. Alberto, J.P. Durte, D.J. Payne, R.B. Egdell, I. McKenzie, C.F. McConville, S.F.J. Cox, and T.D. Veal, Phys. Rev. B **80**, 081201(R) (2009).

3.17. T. Koida, H. Fujiwara, and M. Kondo, Jpn. J. Appl. Phys. **46**, L685 (2007).

3.18. J. P. Remeika and E. G. Spencer, J. Appl. Phys. **35**, 2803 (1964).

3.19. D. R. Hagletner, M. Menhart, P. Jacobson, S. Blomberg, K. Schulte, E. Lundgren, M. Kubicek, J. Fleig, F. Kubel, C. Puls, A. Limbeck, H. Hutter, L. A. Boatner, M. Schmid, and U. Diebold, Phys. Rev. B **85**, 115441 (2012).

3.20. P. Y. Yu and M. Cardona, *Fundamentals of Semiconductors, Physics and Materials Properties* (Springer, Berlin, 2010), 4th ed.

3.21. M. Wöhlecke and L. Kovács, Critical Reviews in Solid State and Materials Sciences **26**, 1 (2001).

3.22. M. Stavola, in *Identification of Defects in Semiconductors*, edited by M. Stavola (Academic Press, San Diego, 1999), Chap. 3, p. 153.

3.23. E. V. Lavrov, F. Herklotz, and J. Weber, Phys. Rev. B **79**, 165210 (2009).

3.24. S.G. Koch, E.V. Lavrov, and J. Weber, Phys. Rev. Lett. **108**, 165501 (2012).

3.25. F. Bekisli, M. Stavola, W.B. Fowler, L. Boatner, E. Spahr, and G. Lüpke, Phys. Rev. B **84**, 035213 (2011).

3.26. In_2O_3 samples that had been deliberately hydrogenated or deuterated by an anneal in H_2 or D_2 gas at 500°C were found to be opaque in the spectral region with a

frequency near 2000 cm^{-1} and below. However, following annealing treatments at temperatures near 400°C that reduced the free carrier concentration, an additional strong IR absorption line emerged at 1890 cm^{-1} as the sample increased in transparency. We found that this line showed no H vs D isotope effect. Raman measurements made for our In_2O_3 samples in their as-grown state showed a strong line at 630 cm^{-1}, in agreement with a previous Raman study of In_2O_3 powder [G. P. Schwartz, W. A. Sunder, and J. E. Griffins, J. Electrochem. Soc. **129**, 1361 (1982)]. We attribute the 1890 cm^{-1} line to the third harmonic of an In_2O_3 lattice phonon with frequency 630 cm^{-1} that has been seen with Raman spectroscopy.

3.27. J. B. Varley, H. Peelaers, A. Janotti, and C. G. Van de Walle, J. Phys. Condens. Matter **23**, 334212 (2011).

3.28. G. P. Schwartz, W. A. Sunder and J. E. Griffiths, J. Electrochem. Soc **129**, 1361-1367 (1982).

3.29. R. Dovesi, V. R. Saunders, C. Roetti, R. Orlando, C. M. Zicovich-Wilson, F. Pascale, B. Civalleri, K. Doll, N. M. Harrison, I. J. Bush, Ph. D'Arco, M. Llunell, *Crystal06 User's Manual*, University of Torino, Torino, 2006.

Chapter 4:

Conclusion

Traditionally, the high electrical conductivity of TCOs has been attributed to native defects such as oxygen vacancies and cation interstitials, while hydrogen was recognized as a passivating defect to the conductivity in most common semiconductors. However, recent theoretical and experimental work have indicated that hydrogen centers can be important shallow donors in the bixbyite-structure, transparent-conducting-oxide In_2O_3.

In this study, the effect that hydrogen impurities have on the conductivity of In_2O_3 single crystals has been studied by IR spectroscopy and theory. We found that annealing In_2O_3 single crystal in an H_2 or D_2 ambient at temperatures near 500°C produces a thin conducting layer near the sample surface, which has been determined as about 0.06 mm in a 1 mm thick sample by thinning experiments. An OH vibrational line at 3306 cm^{-1} has been assigned to the interstitial H shallow-donor center that is responsible for the hydrogen-related conductivity. Annealing experiments following H treatment showed both free carriers and an O-H IR vibrational line at 3306 cm^{-1} that were thermally stable up to ≈ 600°C, which indicated a correlation between them.

The diffusion of hydrogen impurities is important to determine in order understand the chemical reactions of H. Out-diffusion and in-diffusion of hydrogen have been

investigated by isothermal annealing and thinning experiments. The fast and slow decay rates of H_i found in isothermal annealing experiments at 400°C were explained as the out-diffusion of hydrogen in the conducting layer and sample bulk, which yields an out-diffusion coefficient of about 6×10^{-10} cm^2/s. The relationship between the two decay rates and the out-diffusion of hydrogen is supported by numerical calculations in Mathematica which found the out-diffusion coefficient to be 7.22×10^{-10} cm^2/s. (The in-diffusion coefficient in our thinning experiments was found to be about 5×10^{-9} cm^2/s for a 450°C hydrogen treatment by fitting our experimental data with the complementary error function.

Several additional OH lines were produced by the treatment of In_2O_3 in H. Additional configurations for interstitial H with higher formation energies or defects with H trapped by In vacancies have been investigated by theory are candidates for these OH lines.

APPENDIX I

Mathematica code to best fit O-H out-diffusion

```
Df = 2.6*10^-6; x2 = 0.1; t2 = 24;
s1 = NDSolve [{D[y[t, x], t] == Df D[y[t, x], x, x],
     y[0, x] == 3.77*10^19*(Erfc[x/0.01] - Exp[-100000x])*(1 - Exp[-1000(x2 - x)]),
     y[t, 0] == 0, y[t, x2] == 0}, y, {t, 0, t2}, {x, 0, x2}, Method → {"MethodOfLines",
     "SpatialDiscretization" → {"TensorProductGrid", "MinPoints" → 200}}];
Plot3D[Evaluate[y[t, x] /. s1], {x, 0, x2}, {t, 0, t2}, PlotRange → {0, 4*10^19}]
```

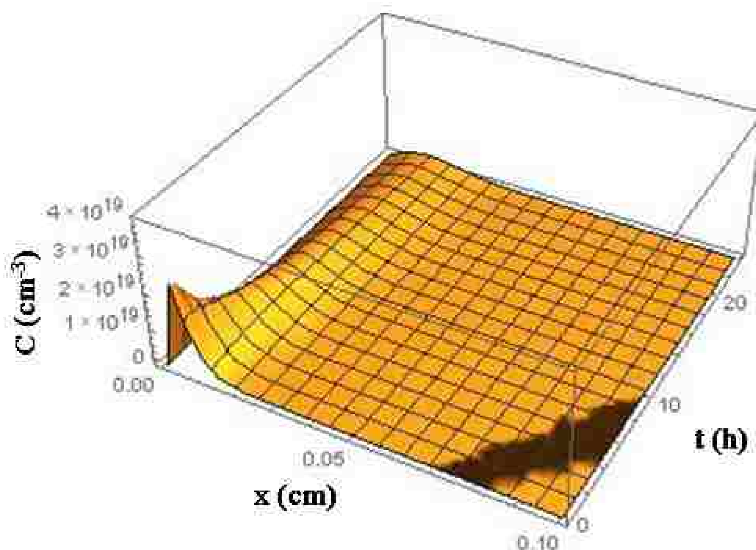


```
Df = 2.6*10^-6; x2 = 0.1; t2 = 24;
f = 5;
s1 = NDSolve [{D[y[t, x], t] == Df D[y[t, x], x, x],
     y[0, x] == 3.77*10^19*(Erfc[x/0.01] - Exp[-100000x])*(1 - Exp[-1000(x2 - x)]),
     y[t, 0] == 0, y[t, x2] == 0}, y, {t, 0, t2}, {x, 0, x2}, Method → {"MethodOfLines",
     "SpatialDiscretization" → {"TensorProductGrid", "MinPoints" → 100}}];
Plot[{Evaluate[y[t2/f/f/f/f/f/f/f, x] /. s1, Evaluate[y[t2/f/f/f/f/f/f, x] /. s1,
     Evaluate[y[t2/f/f/f/f/f, x] /. s1, Evaluate[y[t2/f/f/f/f, x] /. s1,
     Evaluate[y[t2/f/f/f, x] /. s1, Evaluate[y[t2/f/f, x] /. s1, Evaluate[y[t2/f, x],
     Evaluate[y[t2, x] /. s1], {x, 0, x2}, PlotRange → {0, 4*10^19}]
```

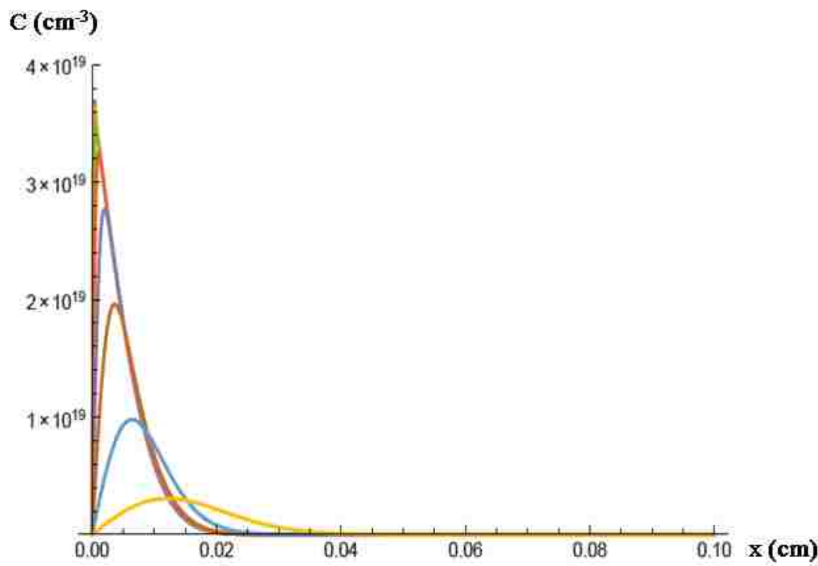

Table[Integrate[Evaluate[y[t, x] /. s1], {x, 0, 0.1}][[1]], {t, 0, 24}]

{2.08823×10^{17}, 1.54892×10^{17}, 1.3677×10^{17}, 1.24824×10^{17}, 1.15916×10^{17}, 1.08854×10^{17}, 1.03037×10^{17}, 9.81193×10^{16}, 9.38799×10^{16}, 9.01699×10^{16}, 8.68839×10^{16}, 8.39442×10^{16}, 8.12925×10^{16}, 7.88834×10^{16}, 7.66813×10^{16}, 7.46576×10^{16}, 7.2789×10^{16}, 7.10563×10^{16}, 6.94436×10^{16}, 6.79375×10^{16}, 6.65265×10^{16}, 6.5201×10^{16}, 6.39525×10^{16}, 6.27738×10^{16}, 6.16586×10^{16}}

ListPlot[%]

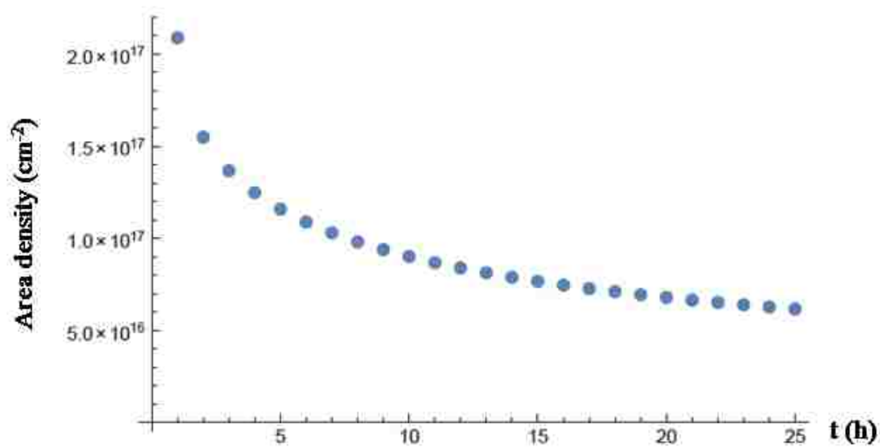

APPENDIX II

Mathematica code to best fit free carrier out-diffusion

```
Df = 7.6*10^-6; x2 = 0.1; t2 = 24;
s1 = NDSolve [{D[y[t, x], t] == Df D[y[t, x], x, x],
     y[0, x] == 3.77*10^19*(Erfc[x/0.01] - Exp[-100000x])*(1 - Exp[-1000(x2 - x)]),
     y[t, 0] == 0, y[t, x2] == 0}, y, {t, 0, t2}, {x, 0, x2}, Method → {"MethodOfLines",
     "SpatialDiscretization" → {"TensorProductGrid", "MinPoints" → 200}}];
Plot3D[Evaluate[y[t, x] /. s1], {x, 0, x2}, {t, 0, t2}, PlotRange → {0, 4*10^19}]
```

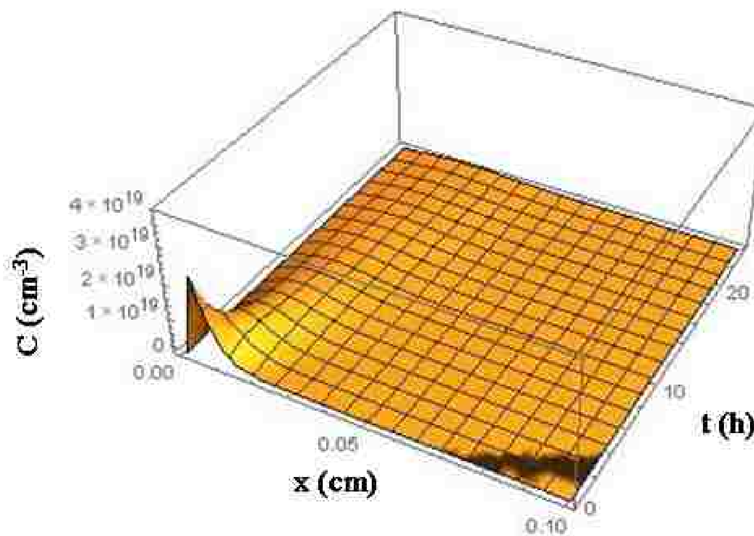


```
Df = 7.6*10^-6; x2 = 0.1; t2 = 24;
f = 5;
s1 = NDSolve [{D[y[t, x], t] == Df D[y[t, x], x, x],
     y[0, x] == 3.77*10^19*(Erfc[x/0.01] - Exp[-100000x])*(1 - Exp[-1000(x2 - x)]),
     y[t, 0] == 0, y[t, x2] == 0}, y, {t, 0, t2}, {x, 0, x2}, Method → {"MethodOfLines",
     "SpatialDiscretization" → {"TensorProductGrid", "MinPoints" → 100}}];
Plot[{Evaluate[y[t2/f/f/f/f/f/f/f, x] /. s1, Evaluate[y[t2/f/f/f/f/f/f, x] /. s1,
     Evaluate[y[t2/f/f/f/f/f, x] /. s1, Evaluate[y[t2/f/f/f/f, x] /. s1,
     Evaluate[y[t2/f/f/f, x] /. s1, Evaluate[y[t2/f/f, x] /. s1, Evaluate[y[t2/f, x],
     Evaluate[y[t2, x] /. s1], {x, 0, x2}, PlotRange → {0, 4*10^19}]
```

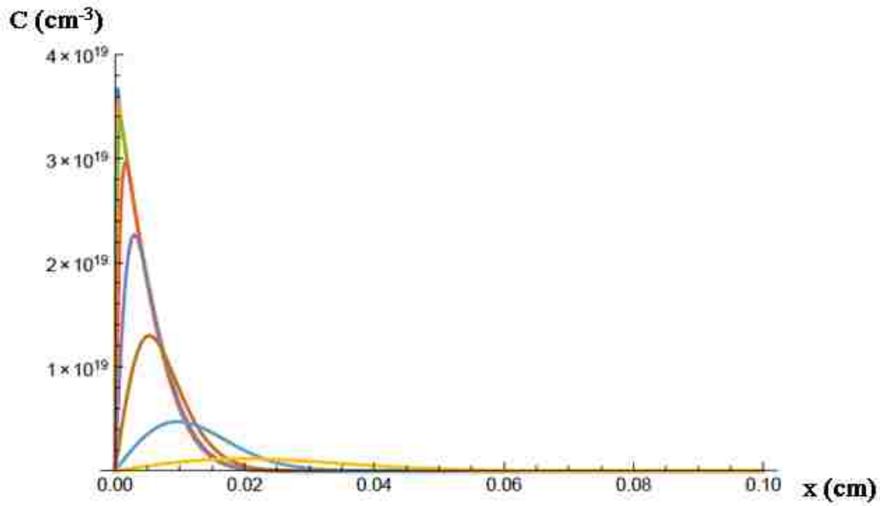


```
Table[Integrate[Evaluate[y[t, x] /. s1], {x, 0, 0.1}][[1]], {t, 0, 24}]
```

{2.08897×10^{17}, 1.25613×10^{17}, 1.03867×10^{17}, 9.09852×10^{16}, 8.20806×10^{16}, 7.54164×10^{16}, 7.0174×10^{16}, 6.59046×10^{16}, 6.23377×10^{16}, 5.9298×10^{16}, 5.66664×10^{16}, 5.43587×10^{16}, 5.23131×10^{16}, 5.04832×10^{16}, 4.88335×10^{16}, 4.73362×10^{16}, 4.5969×10^{16}, 4.47142×10^{16}, 4.3557×10^{16}, 4.24855×10^{16}, 4.14894×10^{16}, 4.05604×10^{16}, 3.96913×10^{16}, 3.88757×10^{16}, 3.81085×10^{16}}

```
ListPlot[%]
```

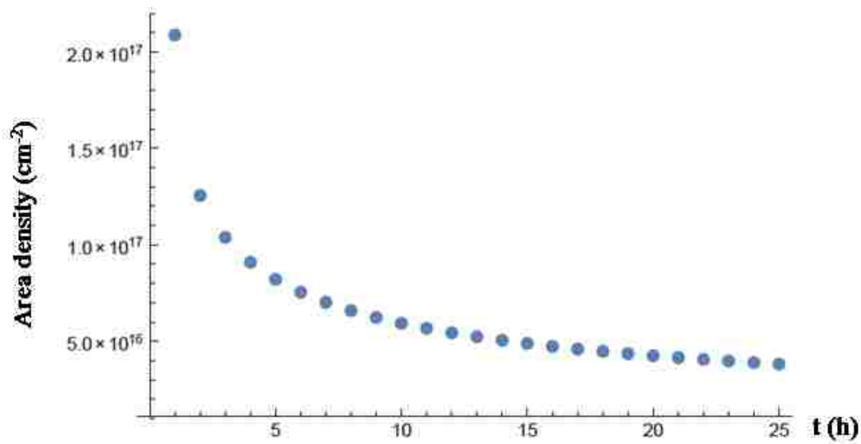

APPENDIX III

Mathematica code to best fit both free carrier and O-H out-diffusion

```
Df = 4.5*10^-6; x2 = 0.1; t2 = 24;
s1 = NDSolve [{D[y[t, x], t] == Df D[y[t, x], x, x],
      y[0, x] == 3.77*10^19*(Erfc[x/0.01] - Exp[-100000x])*(1 - Exp[-1000(x2 - x)]),
      y[t, 0] == 0, y[t, x2] == 0}, y, {t, 0, t2}, {x, 0, x2}, Method → {"MethodOfLines",
      "SpatialDiscretization" → {"TensorProductGrid", "MinPoints" → 200}}];
Plot3D[Evaluate[y[t, x] /. s1], {x, 0, x2}, {t, 0, t2}, PlotRange → {0, 4*10^19}]
```

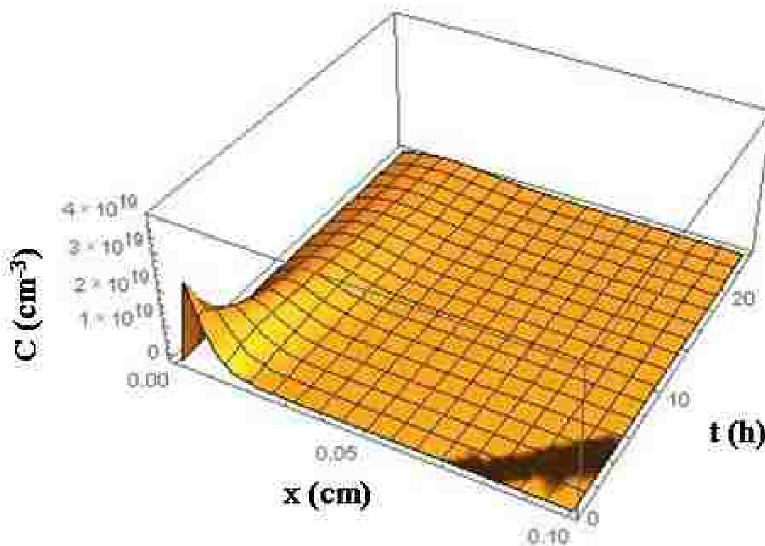


```
Df = 4.5*10^-6; x2 = 0.1; t2 = 24;
f = 5;
s1 = NDSolve [{D[y[t, x], t] == Df D[y[t, x], x, x],
      y[0, x] == 3.77*10^19*(Erfc[x/0.01] - Exp[-100000x])*(1 - Exp[-1000(x2 - x)]),
      y[t, 0] == 0, y[t, x2] == 0}, y, {t, 0, t2}, {x, 0, x2}, Method → {"MethodOfLines",
      "SpatialDiscretization" → {"TensorProductGrid", "MinPoints" → 100}}];
Plot[{Evaluate[y[t2/f/f/f/f/f/f/f, x] /. s1, Evaluate[y[t2/f/f/f/f/f/f, x] /. s1,
      Evaluate[y[t2/f/f/f/f/f, x] /. s1, Evaluate[y[t2/f/f/f/f, x] /. s1,
      Evaluate[y[t2/f/f/f, x] /. s1, Evaluate[y[t2/f/f, x] /. s1, Evaluate[y[t2/f, x],
      Evaluate[y[t2, x] /. s1], {x, 0, x2}, PlotRange → {0, 4*10^19}]
```

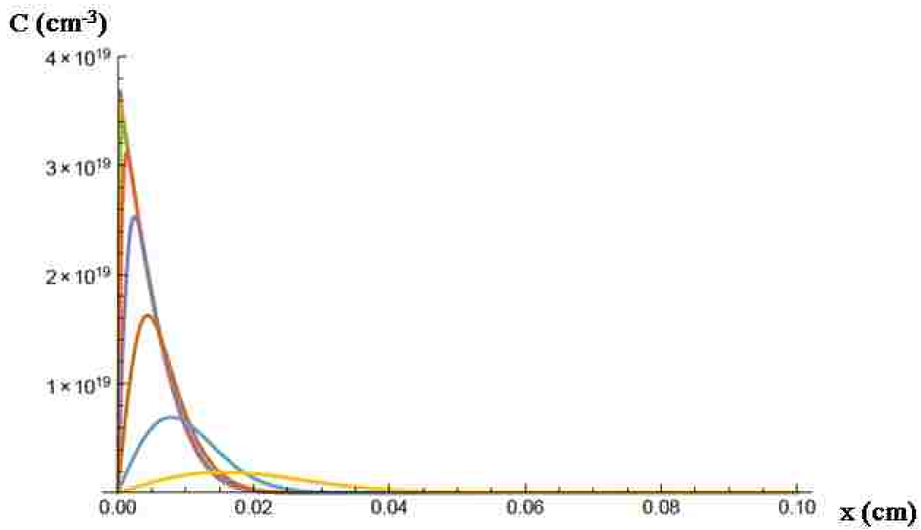

Table[Integrate[Evaluate[y[t, x] /. s1], {x, 0, 0.1}][[1]], {t, 0, 24}]

{2.08848×10^{17}, 1.4081×10^{17}, 1.20428×10^{17}, 1.07652×10^{17}, 9.84712×10^{16}, 9.14015×10^{16}, 8.57158×10^{16}, 8.10029×10^{16}, 7.70078×10^{16}, 7.35619×10^{16}, 7.0548×10^{16}, 6.78815×10^{16}, 6.54997×10^{16}, 6.33548×10^{16}, 6.14096×10^{16}, 5.96347×10^{16}, 5.80064×10^{16}, 5.65054×10^{16}, 5.5116×10^{16}, 5.38248×10^{16}, 5.26207×10^{16}, 5.14943×10^{16}, 5.04376×10^{16}, 4.94437×10^{16}, 4.85064×10^{16}}

ListPlot[%]

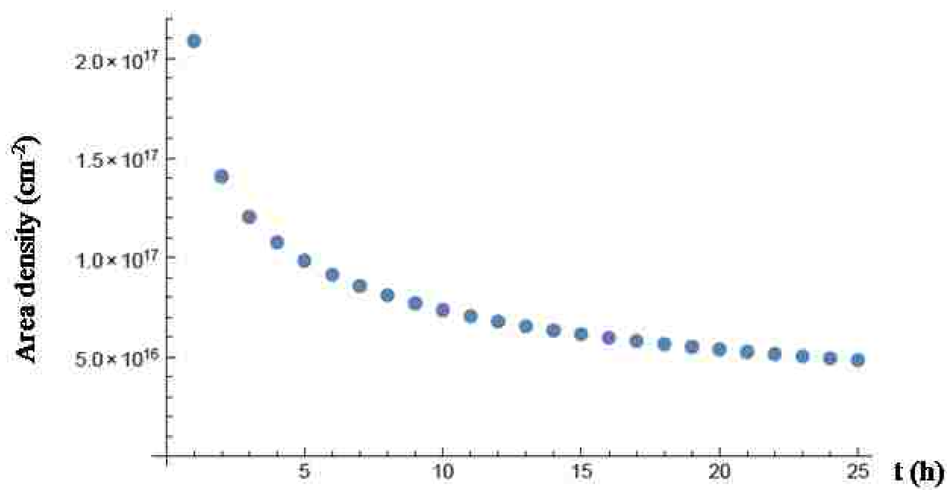

Vita

Weikai Yin started his undergraduate study in Physics at Nankai University in Tianjin, China and received his Bachelor's degree in Physics in June 2010. He enrolled in the Ph.D. program in the Physics Department at Lehigh University in Fall semester 2010. He worked as a Teaching Assistant in Introductory of Physics from August 2010 to May 2012. He began his Ph.D. research on semiconductor impurities supervised by Professor Michael Stavola during the summer of 2011 and then continued his research in Professor Stavola's group since June 2012. Weikai worked as a Research Assistant in this group between 2012 and 2015, focusing on hydrogen defects in semiconducting oxides. During his five years at Lehigh, he also earned his Master's degree in Electrical Engineering in January 2014.